

## ABSTRACT

### DOSIMETRIC STUDY OF BETA-MINUS EMITTER PRASEODYMIUM-142: APPLICATIONS IN MICROSPHERE BRACHYTHERAPY FOR HEPATOCELLULAR CARCINOMA AND BRACHYTHERAPY FOR OCULAR SQUAMOUS CELL CARCINOMA

by Maria Clara Ferreira

July 2013

Director of Dissertation: Dr. Jae Won Jung

DEPARTMENT OF PHYSICS

A dosimetric study of the beta-minus emitter Praseodymium-142 ( $^{142}\text{Pr}$ ) was performed and two main innovative applications of this source in brachytherapy are proposed: microsphere brachytherapy and eye plaque brachytherapy.  $^{142}\text{Pr}$  (96.3% beta and 3.7% gamma) has recently gained increased attention among beta sources for therapy. Its inherent physical and dosimetric characteristics may be suitable for several brachytherapy applications. This relatively short half-life (19.12 h) allows this source to deliver high dose rates to the target. Penetration of the beta component of  $^{142}\text{Pr}$  radiation in tissue is limited to a few millimeters, therefore limiting dose deposition to the treated site. The large neutron activation cross-section of the parent isotope (11.40 barn including that of a meta-stable state) allows the activation of this nuclide in a low neutron fluence reactor, making its production easily available for both research and therapy purposes. From simulations and measurement of the doses, exposure rates due to the 3.7% gamma component showed to be clinically small for the patients' healthy organs and tissues as well as to medical staff and general public. Furthermore, it was studied whether its gamma

component could be effective in performing pre-treatment quality assurance (QA) and dosimetry, as well as post-treatment biodistribution imaging and dose distributions of permanently implanted  $^{142}\text{Pr}$  brachytherapy sources. Two main novel applications of  $^{142}\text{Pr}$  beta emitters are studied in this work: (i)  $^{142}\text{Pr}$  glass microspheres, as a possible choice of radionuclide for microsphere brachytherapy of nonresectable hepatocellular carcinoma (HCC) and metastasis of the liver, and (ii)  $^{142}\text{Pr}$  glass rods for brachytherapy of ocular squamous cell carcinoma (OSCC), based on a novel design for eye brachytherapy – also developed in this work. In order to simulate the dosimetric characteristics of  $^{142}\text{Pr}$ , MCNPX2.6 Monte Carlo code and BRAIN-DOSE Dose Point Kernel code were used to determine the dose distributions of  $^{142}\text{Pr}$  for different source distributions. Dosimetric properties of the currently used nuclide in microsphere brachytherapy, Yttrium-90 ( $^{90}\text{Y}$ ), was also studied and compared to  $^{142}\text{Pr}$ . A more realistic biodistribution model of microspheres within a single HCCs blood vessel was studied. In addition, the biological effective dose (BED) for different tumor doubling times (DT) for HCC was determined using the linear quadratic (LQ) model for both nuclides. Dose distributions for  $^{142}\text{Pr}$ ,  $^{90}\text{Y}$  and Rhenium-188 were simulated within the eyeball and compared for application in eye brachytherapy. Measurements of dose distribution using GAFCHROMIC<sup>®</sup> EBT2 film were performed with  $^{142}\text{Pr}$  glass microspheres and  $^{142}\text{Pr}$  glass rods. Monte Carlo simulation validation with experimental measurements in phantom of the dose distribution due to  $^{142}\text{Pr}$  glass microspheres and  $^{142}\text{Pr}$  glass rods were performed.  $^{142}\text{Pr}$  showed to be a possible choice of radionuclide for HCC microsphere brachytherapy and OSCC brachytherapy, delivering a high biological effective dose, and opening possibilities for post treatment imaging and biodistribution assessment.



DOSIMETRIC STUDY OF BETA-MINUS EMITTER PRASEODYMIUM-142:  
APPLICATIONS IN MICROSPHERE BRACHYTHERAPY FOR  
HEPATOCELLULAR CARCINOMA AND  
BRACHYTHERAPY FOR OCULAR SQUAMOUS CELL CARCINOMA

A Dissertation

Presented To

The faculty of the Department of Physics

East Carolina University

In Partial Fulfillment of the Requirements for the Degree

Doctor of Philosophy in Biomedical Physics

by

Maria Clara Ferreira

July 2013

© Maria Clara Ferreira, 2013

DOSIMETRIC STUDY OF BETA-MINUS EMITTER PRASEODYMIUM-142:  
APPLICATIONS IN MICROSPHERE BRACHYTHERAPY FOR  
HEPATOCELLULAR CARCINOMA AND  
BRACHYTHERAPY FOR OCULAR SQUAMOUS CELL CARCINOMA

by

Maria Clara Ferreira

APPROVED BY:

DIRECTOR OF  
DISSERTATION/THESIS:

\_\_\_\_\_  
Jae Won Jung, PhD

COMMITTEE MEMBER:

\_\_\_\_\_  
Michael Dingfelder, PhD

COMMITTEE MEMBER:

\_\_\_\_\_  
Zhibin Huang, PhD

COMMITTEE MEMBER:

\_\_\_\_\_  
Karl Rasmussen, PhD

COMMITTEE MEMBER:

\_\_\_\_\_  
Jefferson Shinpaugh, PhD

CHAIR OF THE DEPARTMENT  
OF PHYSICS:

\_\_\_\_\_  
John C. Sutherland, PhD

DEAN OF THE  
GRADUATE SCHOOL:

\_\_\_\_\_  
Paul J. Gemperline, PhD

## ACKNOWLEDGEMENTS

I would like to thank Dr. Jae Won Jung for the great support and guidance with my research projects. I also would like to thank all the professors whom I had the honor to work with, in special: Dr. Carlo Campos, Dr. Claudio Sibata, Dr. Helvecio Mota, Dr. Michael Dingfelder, Dr. Karl Rasmussen, and Dr. Edson Rocha, thanks for all the advices and helpful research discussions. Thanks to the dissertation committee members, Dr. Jae Won Jung, Dr. Michael Dingfelder, Dr. Zhibin Huang, Dr. Karl Rasmussen, and Dr. Jefferson Shinpaugh for the manuscript review and helpful suggestions.

Great thanks to my lab mates and co-workers, who helped me to overcome the challenges in this journey: Jihyung Yoon, Chris Pelletier, Emtenan Alotaibi, and Raj Maharjan. I also would like to thank the physics staff that helped me in every way to get things done on time and on the best way possible: Dr. Yong-Qing Li, Dr. Lingbo Kong, Mr. Daniel Criminger, Mrs. Brenda Doss, Mr. Gene Oakley, Mr. Marcus Jeannette, and Mr. Chris Bonnerup, I really appreciate it. Thanks to the radiation safety officer, Mr. Robert Hall, and Dr. David Robertson from the University of Missouri Research Reactor (MURR<sup>®</sup>), for helping with the irradiation and with partial financial support for the seed irradiation.

I also would like to thank my dear friends for all the support and help. I am fortunate for having met so many great people in my journey through this degree. Special thanks to Cristiano Rizzotto, for all the unconditional support and friendship, to my research mentor, friend and life coach, Dr. Carlos Campos, to his wife and great friend, Dr. Diana Campos, to my dear friend and sister by choice, Maria Lucia Ferreira, and to my dear friend Terry Stafford. Thanks to my friends Quendela Taylor, Bineyam Kassahum, Sarah Hollis, Soma Prum, Sidi Benhabib, Dana

Raper, Jenny Sattler, Stacy-Ann Stephenson, Jasdeep Kaur, and Lydia Levinson Handsfield. I would not know how to find strength and motivation if it wasn't for these truly kind and warm hearted people who have helped me greatly during these years. They all have become my second family on this other side of the globe. Finally I would like to thank my family and friends in Brazil, for being understanding and supportive of my hours dedicated to my studies and research, and the years away from home. Thanks to my dear friends Mariana Mendes and Davi Monteiro. Thanks to my grandmother, Maria Miranda, to my mother, Elizabeth Miranda, my aunt, Rosângela Leite, my uncle, Eduardo Miranda, my cousins, Carolina Parreira, Daniel Parreira, Natália Parreira, Cristiane Eirado and Magda Miranda for all the unconditional love and support.

# TABLE OF CONTENTS

<b>LIST OF FIGURES</b> .....	iv
<b>LIST OF TABLES</b> .....	viii
<b>LIST OF ABBREVIATIONS</b> .....	ix
<b>CHAPTER 1: INTRODUCTION</b> .....	1
1.1 Importance of Brachytherapy in the current clinical practice.....	1
1.2 Hepatocellular Carcinoma (HCC) and <sup>142</sup> Pr Microsphere Brachytherapy.....	5
1.3 Ocular Squamous Cell Carcinoma (OSCC) and <sup>142</sup> Pr Eye Brachytherapy.....	10
1.4 BRAIN-DOSE and MCNPX2.6 Monte Carlo Radiation Transport Code.....	14
1.5 Biological Effective Dose (BED) and the Linear Quadratic (LQ) Model.....	17
1.6 Beta Emitter <sup>142</sup> Pr: Radionuclide Properties.....	19
1.7 Electron Maximum Range.....	20
1.8 Decay modes of <sup>142</sup> Pr.....	21
1.9 Radionuclide Production.....	22
1.10 GAFCHROMIC <sup>®</sup> EBT2 Dosimetry Film.....	24
1.11 Specific Aims.....	26
<b>CHAPTER 2: MATERIALS AND METHODS I: SIMULATIONS</b> .....	28
2.1 <sup>142</sup> Pr MICROSPHERE BRACHYTHERAPY.....	28
2.1.1 Clinical Activity and Tumor Target Dose.....	28
2.1.2 Physical and Radiobiological Properties.....	28
2.1.3 MCNPX2.6 Monte Carlo Simulations.....	32

2.1.4 Analytical calculations for gamma dose distribution.....	37
2.2 CONFORMAL EYE BRACHYTHERAPY DEVICE.....	40
2.2.1 Device Development.....	40
2.2.2 CEBT design.....	41
2.2.3 MCNPX2.6 Monte Carlo Simulation for CEBT device.....	43
2.2.4 MCNPX2.6 Monte Carlo Simulations for $^{142}\text{Pr}$ , $^{90}\text{Y}$ , and $^{188}\text{Re}$ .....	44
<b>CHAPTER 3: MATERIALS AND METHODS II: EXPERIMENTAL DESIGN.....</b>	<b>49</b>
3.1 Microsphere Brachytherapy and Eye Brachytherapy.....	49
3.2 Nuclide Activation.....	49
3.3 Experimental Setup.....	51
3.3.1 Film Calibration.....	51
3.3.2 Verification of Glass Microspheres.....	56
3.3.3 Experimental setup for accessing dose fall-off of microspheres.....	59
3.3.4 Glass Rod Measurements.....	66
3.4 Radiation Safety and Shielding of the Experimental Setup.....	67
<b>CHAPTER 4: RESULTS.....</b>	<b>71</b>
4.1 $^{142}\text{Pr}$ MICROSPHERE BRACHYTHERAPY.....	71
4.1.1 Biological Effective Doses for $^{142}\text{Pr}$ and $^{90}\text{Y}$ .....	71
4.1.2 MCNPX2.6 Monte Carlo Simulations.....	75
4.1.3 MCNPX2.6 model for $^{142}\text{Pr}$ glass microspheres experimental design.....	87
4.2 $^{142}\text{Pr}$ CONFORMAL EYE BRACHYTHERAPY DEVICE.....	90
4.2.1 MCNPX2.6 $^{142}\text{Pr}$ Dose distributions within the eye.....	90
4.2.2. Comparison of $^{142}\text{Pr}$ , $^{90}\text{Y}$ and $^{188}\text{Re}$ dose distributions.....	90

4.2.3 MCNPX2.6 model for experimental design of <sup>142</sup> Pr glass rod.....	91
4.3 Experimental Results and Monte Carlo Validation.....	97
4.3.1 <sup>142</sup> Pr glass microspheres.....	97
4.3.1 <sup>142</sup> Pr glass rods.....	98
4.4 MCNPX2.6 Simulations and Experimental Uncertainties Considerations.....	107
<b>CHAPTER 5: DISCUSSIONS AND CONCLUSIONS.....</b>	<b>108</b>
5.1 Microsphere Brachytherapy.....	109
5.1.1 Future work.....	112
5.2 Conformal Eye Brachytherapy.....	113
5.2.1 Patent and Future Work.....	114
<b>REFERENCES.....</b>	<b>116</b>
<b>APPENDIX A: MCNPX2.6 INPUTS.....</b>	<b>126</b>
A.1: Microsphere Brachytherapy Inputs.....	126
A1.1: Source homogeneously distributed model for spherical tumor.....	125
A1.2: Cylindrical blood vessel model.....	128
A.1.3: Glass Capillary filled with <sup>142</sup> Pr.....	130
A.2: Eye Applicator Input.....	133
A.2.1 Eye Dose profile at water.....	133
A.2.2 Dose at Water for <sup>142</sup> Pr, <sup>90</sup> Y and <sup>188</sup> Re.....	135
A.2.3 Eye dose profiles at water: Experimental Geometry.....	137
<b>APPENDIX B: SELECTED PUBLISHED ABSTRACTS AND AWARDS.....</b>	<b>139</b>

## LIST OF FIGURES

<b>Figure 1.1</b>	Cross-section of a GAFCHROMIC <sup>®</sup> EBT2 film sheet.....	26
<b>Figure 2.1</b>	<sup>142</sup> Pr and <sup>90</sup> Y Beta energy spectrum used for MC simulation.....	32
<b>Figure 2.2</b>	Model of 20µm blood vessel within a 1 cm tumor.....	35
<b>Figure 2.3</b>	Geometric model used for analytical calculation.....	38
<b>Figure 2.4</b>	Eye applicator design.....	41
<b>Figure 2.5</b>	Eye applicator holder.....	42
<b>Figure 2.6</b>	Top view of the eye applicator.....	45
<b>Figure 2.7</b>	Eye model with one rod touching the eye surface.....	46
<b>Figure 2.8</b>	Sagittal view of the geometry input used in the MCNPX2.6 to simulate the dose distribution due to <sup>142</sup> Pr, <sup>90</sup> Y and <sup>188</sup> Re within the eyeball.....	47
<b>Figure 2.9</b>	Geometry input used in the MCNPX2.6 to simulate the dose distribution due to <sup>142</sup> Pr experiments with glass rods.	48
<b>Figure 3.1</b>	RBG film channels and their different brightness responses to radiation doses.....	54
<b>Figure 3.2</b>	Film calibration using a Siemens ONCOR 6 MeV electron beam.....	55
<b>Figure 3.3</b>	Inactivated Pr glass microspheres.....	57

<b>Figure 3.4</b>	Microscopic view of the $^{141}\text{Pr}$ microspheres.....	58
<b>Figure 3.5</b>	Glass capillaries used as receptacle of microspheres.....	60
<b>Figure 3.6</b>	Micropipette used to fill the glass capillary with $^{142}\text{Pr}$ microsphere solution..	61
<b>Figure 3.7</b>	Air-microcapillary-microsphere solution interface under the microscope.....	62
<b>Figure 3.8</b>	Phantom developed to carry the measurements with the microspheres.....	63
<b>Figure 3.9</b>	$^{142}\text{Pr}$ glass rods and DREMEL tool with diamond cut-off wheel.....	65
<b>Figure 3.10</b>	View of the glass rods placed on top of the junction of the Gammex Solid Water <sup>®</sup> .....	66
<b>Figure 3.12</b>	Dry box used to carry the $^{142}\text{Pr}$ measurements.....	68
<b>Figure 3.13</b>	Beta syringe shield.....	69
<b>Figure 4.1</b>	Biological Effective Dose for tumor and non-tumor tissues.....	73
<b>Figure 4.2</b>	DPK calculations and comparison with the benchmarking.....	75
<b>Figure 4.3</b>	DPK calculations and MCNPX simulation of the dose distribution for $^{142}\text{Pr}$ .....	76
<b>Figure 4.4</b>	Contour plot of the MCNPX2.6 simulation of dose distribution for $^{142}\text{Pr}$ ....	78
<b>Figure 4.5</b>	Beta and gamma contributions to the dose for $^{142}\text{Pr}$ .....	79
<b>Figure 4.6</b>	Dose distribution for tumor radii ranging from 1 cm to 5 cm.....	81

<b>Figure 4.7</b>	Validation of the MCNPX2.6 simulations for the $^{142}\text{Pr}$ gamma dose distribution using the analytical calculations.....	82
<b>Figure 4.8</b>	Simulation of the dose distribution generated by the 20 $\mu\text{m}$ diameter blood vessel model (white line in the center) within a 0.5 cm tumor.....	83
<b>Figure 4.9</b>	Dose distributions for a blood vessel placed in the center of tumor and placed at the tumor boundary.....	84
<b>Figure 4.10</b>	BEDVH(use full name).....	85
<b>Figure 4.11</b>	Dose distributions for a glass capillary filled with glass $^{142}\text{Pr}$ microspheres.	88
<b>Figure 4.12</b>	Linear-log plot of the dose distributions (Gy) per decay for a glass capillary filled with glass $^{142}\text{Pr}$ microspheres.....	89
<b>Figure 4.13</b>	Dose distribution inside the eye for a $^{142}\text{Pr}$ rod.....	92
<b>Figure 4.14</b>	Axial profile of dose (Gy) per decay due to one $^{142}\text{Pr}$ rod touching the eye surface.....	93
<b>Figure 4.15</b>	Comparison of dose distributions for $^{142}\text{Pr}$ , $^{90}\text{Y}$ and $^{188}\text{Re}$ .....	94
<b>Figure 4.16</b>	MCNPX2.6 Simulations for the dose (Gy) per decay profile of model used for experimental setup.....	95
<b>Figure 4.17</b>	Axial profile of dose (Gy) per decay due to one $^{142}\text{Pr}$ rod in contact with a squared water phantom.....	96
<b>Figure 4.18</b>	$^{142}\text{Pr}$ Spectrum measured with the NaI scintillator detector.....	99
<b>Figure 4.19</b>	Scan of GAFCHROMIC® EBT2 film measurement for the glass capillary.	100
<b>Figure 4.20</b>	Isodose lines (cGy) for the glass microcapillary dose measurements in GAFCHROMIC® EBT2 film.....	101

<b>Figure 4.21</b>	Monte Carlo Simulation (cGy) for a total of 70,000 <sup>142</sup> Pr glass microspheres in a glass capillary.....	102
<b>Figure 4.22</b>	Monte Carlo and GAFCHROMIC® EBT2 film measurements for the <sup>142</sup> Pr glass microspheres.....	103
<b>Figure 4.23</b>	Axial and transversal GAFCHROMIC® EBT2 film measurement of <sup>142</sup> Pr glass rod.....	104
<b>Figure 4.24</b>	Isodose lines (cGy) for the glass rods dose measurements in GAFCHROMIC® EBT2 film.....	105
<b>Figure 4.25</b>	Monte Carlo Simulation (cGy) for a total of decays of a <sup>142</sup> Pr glass rod.....	106

## LIST OF TABLES

<b>Table 1.1</b>	Property of beta-emitter radionuclides for medical applications.....	4
<b>Table 2.1</b>	Physical properties of beta emitters used in microsphere brachytherapy.	29
<b>Table 2.2</b>	Composition of $^{142}\text{Pr}$ and $^{90}\text{Y}$ glass microspheres.....	30
<b>Table 3.1</b>	Measured exposure rates.....	70
<b>Table 4.1</b>	Calculated BED values for 150 Gy physical total dose.....	72
<b>Table 4.2</b>	Percent of the tumor volume covered with a BED higher than 150 Gy for different tumor radius and blood vessel diameters.....	86

## LIST OF SYMBOLS AND ABBREVIATIONS

$^{142}\text{Pr}$	Praseodymium-142
$^{188}\text{Re}$	Rhenium-188
$^{90}\text{Y}$	Yttrium-90
ABS	American Brachytherapy Society
ALARA	As Low As Reasonably Achievable
BED	Biologic Effective Dose
BEDVH	Biologic Effective Dose Volume Histogram
CEBT	Conformal Eye Brachytherapy Device
DPK	Dose Point Kernel
DT	Doubling Time
EBRT	External Beam Radiation Therapy
HCC	Hepatocellular Carcinoma
HDR	High Dose Rate
IMRT	Intensity Modulated Radiation Therapy
LQ	Linear Quadratic
MC	Monte Carlo

MCNPX	Monte Carlo N-Particle eXtended
NIST	National Institute of Standards and Technology
OD	Optical Density
OSCC	Ocular Squamous Cell Carcinoma
PD	Physical Dose
QA	Quality Assurance
REAS	Rare Earth Aluminosilicate
RGB	Red Green Blue
SIRT	Selective internal radiation therapy
TD	Total Dose
TRIGA	Training, Research, Isotopes, and General Atomics
YAS	Yttrium Aluminosilicate

## CHAPTER 1: INTRODUCTION

### 1.1 Importance of Brachytherapy in the current clinical practice

Brachytherapy, from the Greek word *brachys*, meaning “short-distance”, is a form of internal radiotherapy, in which a short-range radiation source is placed inside or near the tumor. Brachytherapy can be used to treat several body sites and it has been used as an effective treatment for prostate, breast, skin, and cervical cancer. This technique allows the localization of high doses of radiation to the tumor, while sparing surrounding healthy tissues. Because it is highly targeted, brachytherapy presents lower risks of side effects due to radiation and is usually well tolerated. Brachytherapy can be used in combination with other techniques, such as external beam radiation therapy (EBRT) and chemotherapy.

Shortly after the discovery of radioactivity by Henri Becquerel in 1896, radioactive sources were used in a variety of medical treatments. The first reported case of radiation being used in the treatment of cancer was in 1899. Marie and Pierre Currie were the first to suggest that radioactive sources could be implanted in or near tumors. This was the beginning of brachytherapy, at the time known as curietherapy. The Curie institute in Paris pioneered the improvement and development of the technique in the earlier twentieth century, developing successful treatment schedules for gynecologic malignancies.

Radium sources were the most common type of internal source used during the 1930s. Gold seeds filled with radon were developed in 1942 and used until 1958. After the World War II, Cobalt needles were used for a short period of time, but were ultimately replaced by tantalum

and gold. Iridium sources were first used in 1958, and these continue to be the most commonly used radioactive sources for brachytherapy.

Due to the unnecessary radiation exposure to operators, the use of brachytherapy declined in the middle twentieth century in Europe and in the United States. It was only with the improvement of remote after-loading and computerized dose calculation techniques, in the 1950s and 1960s, that brachytherapy regained interest in the medical community. After-loading techniques allow the therapist to deliver the seeds remotely, therefore decreasing the risk of unnecessary radiation exposure. This technique uses hollow catheters or guide tubes inserted in the target volume, which are then loaded with radioactive sources. Improvements in the dose calculations prior to interstitial brachytherapy treatment made it possible to plan a homogeneous tumor dose distribution, avoiding hot spots in the tumor and surrounding healthy tissues.

A large variety of clinical instrumentation is currently available for implementing numerous types of brachytherapy procedures (Nath et al., 1997). The types of brachytherapy techniques can be classified according to (i) the place where the seeds are implanted, (ii) the dose rate that the radiation is delivered and (iii) the duration of the dose delivery.

Radioactive seeds can be placed within the target tissue or interstitially, e.g. in the prostate or in the breast, or it can be placed in contact or next to the treated area, such as a body cavity, e.g. cervix, uterus or vagina, or a body surface, e.g. skin. Radiation sources can also be placed in blood vessels (intravascular brachytherapy), e.g. coronary and liver blood vessels. Intraluminal brachytherapy is also used for treating tumors that obstruct the opening of hollow organs, such as pulmonary bronchus, biliary duct, and esophagus.

The dose rate (Gray per hour) at which the radiation is delivered can be classified in two general categories: low dose rate (LDR) and high dose rate (HDR) brachytherapy. Dose rates of LDR brachytherapy go up to 2 Gy/h, from radium, cesium, cobalt, or iridium sources and it is usually used to treat the oral cavity, oropharynx, sarcomas, cervix and prostate cancers. In the past few decades, HDR has been developed as an alternative method for brachytherapy. In HDR brachytherapy, dose rates are greater than 12 Gy/h, (ICRU Report 38) a rate commonly used in linear accelerators for external beam therapy (Nath et al., 2007), and is used for treating lungs, breast, cervix, and prostate cancers. In most cases, HDR brachytherapy is performed in an outpatient basis. The radiation source can either be implanted permanently or temporarily placed in or near the treatment site. Temporary brachytherapy involves placement of radiation sources for a certain period of time before being withdrawn. In permanent brachytherapy, also known as seed implantation, small radioactive seeds are implanted permanently in the tumor or treatment site.

Many radionuclides have been studied for use in brachytherapy. These sources have a wide range of half-lives and energies (Häfeli, 2001). Several brachytherapy sources are currently available for use, and these sources vary in shape, size, and radionuclide used. Each source type may have a different application or medical purpose, depending on their radiation energy, dosimetric characteristics and physical properties. Radiation sources used for medical applications may emit alpha, beta or gamma radiation. In the current work, the beta-minus emitter  $^{142}\text{Pr}$  was studied. Table 1.1 lists several beta-emitters and their radiological properties, such as half-life, average and maximum beta energy, gamma emissions with their percentage yield, etc.

**Table 1.1** Property of beta-emitter radionuclides used in radiation therapy

Radioisotope	Half-Life	Average/Max Beta Energy (keV) <sup>†</sup>	Max. range in tissue (mm)*	Gamma	Production
<sup>3</sup> H	12.3 y	5.7 / 18.0	$5.48 \times 10^{-3}$	none	<sup>6</sup> Li(n,α) <sup>3</sup> H
<sup>14</sup> C	5730 y	49.5 / 156.0	0.287	none	<sup>14</sup> N(n,p) <sup>14</sup> C
<sup>32</sup> P	14.3 d	694.9 / 1710.2	7.90	none	<sup>32</sup> S(n,p) <sup>32</sup> P or <sup>31</sup> P(n,γ) <sup>32</sup> P
<sup>90</sup> Y	64.1 h	933.6 / 2280.0	10.9	none	<sup>90</sup> Sr/ <sup>90</sup> Y generator
<sup>131</sup> I	8.0 d	181.7 / 806.9	2.4	364.5 keV (82.5%)	<sup>131</sup> Te (β <sup>-</sup> ) <sup>131</sup> I
<sup>142</sup> Pr	19.12 h	809.0 / 2162.0	10.3	1580 keV (3.7%)	<sup>141</sup> Pr(n, γ) <sup>142</sup> Pr
<sup>153</sup> Sm	46.5 h	224.2 / 808.2	3.0	103.2 keV (29.8%)	<sup>152</sup> Sm(n,γ) <sup>153</sup> Sm
<sup>165</sup> Dy	2.3 h	440.2 / 1286.7	6.4	94.7 keV (3.6%)	<sup>164</sup> Dy(n,γ) <sup>165</sup> Dy
<sup>166</sup> Ho	26.8 h	665.1 / 1853.9	10.2	80.6 keV (6.7%)	<sup>165</sup> Ho(n,γ) <sup>166</sup> Ho
<sup>169</sup> Er	9.4 d	99.6 / 350.9	1.0	< 0.2%	<sup>168</sup> Er(n,γ) <sup>169</sup> Er
<sup>177</sup> Lu	6.7 d	133.3 / 497.8	1.7	113.0 keV (6.4%) 208.4 keV (11%)	<sup>176</sup> Lu(n,γ) <sup>177</sup> Lu
<sup>186</sup> Re	89.2 h	346.7 / 1069.5	5.0	137.2 keV (9.42%)	<sup>185</sup> Re(n,γ) <sup>186</sup> Re
<sup>188</sup> Re	17.0 h	764.3 / 2120.4	10.0	155.0 keV (15.1%)	<sup>188</sup> W/ <sup>188</sup> Re generator
<sup>198</sup> Au	2.7 d	311.5 / 960.7	4.4	411.8 keV (95.5%)	<sup>197</sup> Au(n,γ) <sup>198</sup> Au

<sup>†</sup>NuDat database (Kinsey, 1998)

\*Calculated using empirical formula (Katz and Penfold, 1952)

In order to deliver significant radiation doses to the treatment area, applicator modifications, insertion techniques, dose specification, and new radionuclides have been developed for LDR and HDR brachytherapy. In the following sections, the background information on microsphere brachytherapy and eye plaque brachytherapy will be discussed and the rationale for the needed improvement of these techniques will be explained.

## **1.2 Hepatocellular Carcinoma (HCC) and $^{142}\text{Pr}$ Microsphere Brachytherapy**

The liver is a vital organ that has several functions, such as breaking down and storing nutrients from the intestine, generating clotting factors needed to stop bleeding from injuries, producing bile essential for the absorption of nutrients in the intestine, breaking down toxic waste and filtering the blood, among other functions. The liver is the largest internal organ of the human body. It is divided into right and left lobe. It receives blood supply from two different sources: the portal vein (blood rich in nutrients from the intestine) and the hepatic artery (blood rich in oxygen).

Both malignant and benign tumors can develop in the liver. The most common type of malignant liver cancer in adults is hepatocellular carcinoma (HCC) (primary) and metastasized colon cancer (secondary). About 80% of the primary liver cancers are HCC. Primary HCC can be classified into two main groups: a primary single tumor, that grows then spreads to other liver sites, or multiple primary tumors throughout the liver (usually as a consequence of other ongoing liver cells damage or cirrhosis). The latter is the most common type in the United States and the frequency of this type of HCC has been increasing throughout western countries (Hennequin et al., 2011). In 2013 it is estimated that 30,640 new cases of primary liver cancer will be diagnosed in the United States. Of these cases, an estimated 21,670 will be fatal. Liver cancer is more

common on the continents of Africa (especially in sub-Saharan countries) and Asia (predominantly in the eastern countries) (ACS Liver Cancer, 2012).

Tumors can be either resectable, i.e. removable through surgery, or nonresectable. Determining whether a tumor is resectable depends on the location, size, patient overall health conditions, as well as a variety of other factors. There has to be sufficient hepatic parenchyma left after surgery for the proper functioning of the organ, meaning that the tumor have to be small enough and have a well-defined border. Although surgical removal of liver tumors may offer the best cure rates, more than 75% of primary liver tumors and 90% of secondary liver tumors are nonresectable.

There are different methods for treating liver tumors that are difficult to reach or nonresectable. Currently available methods are: stereotactic body radiosurgery, cyber knife radiosurgery (Bianciotto et al. 2010), microsphere radioembolization, transarterial chemoembolization, radiofrequency ablation, etc. The choice of the treatment method depends on the stage of the disease, the patient treatment preferences, the available methods in a given cancer center, as well as the treatment cost.

One of the challenges of treating hepatocellular carcinoma with radiation is the fact that hepatic tumor are radioresistant, while liver parenchyma cells are radiosensitive. This limits the amount of dose that can be delivered by conventional external beam radiotherapy, since the normal hepatic parenchyma cannot tolerate high doses. The maximum external dose tolerated by the whole liver is 35 Gy fractionated in 1.8 Gy per day (Dezarn et al., 2011). New methods focusing on a more targeted approach began to emerge in response to the challenge presented by the radiosensitivity of hepatic parenchyma. Microsphere brachytherapy is an example of

treatment capable of delivering high doses to specific parts of the liver, allowing the treatment of tumor sites while sparing normal tissue.

Microsphere brachytherapy has gained an increased importance among cancer treatment modalities and research topics in radiotherapy (Salem and Thurston, 2006; Council Steering Committee, 2008; Kennedy et al., 2007; Dezarn et al., 2011). Radioactive microspheres have sizes ranging from 10 to 30  $\mu\text{m}$ , meaning they are larger than capillaries and are easily trapped in the capillary beds. These spheres remain permanently implanted and deliver radiation dose locally (Häfeli, 2001). It is a selective internal radiation therapy (SIRT), in which the target organ or tumor site receives a high dose of radiation, while the surrounding healthy tissue receives a very low dose when compared to other treatment modalities, e.g. external beam radiation therapy (EBRT). Typical effective treatment range in tissue is up to several millimeters for beta-emitters. At the present stage, the technique has been used for unresectable liver tumors cases in which standard treatments, such as chemotherapy and radiotherapy, have failed to treat the malignancy. Microsphere brachytherapy is a palliative, not curative, treatment. However, patients have benefited from this treatment through life-extension and improvements in quality of life.

Microsphere brachytherapy was originally used to treat patients with rheumatoid arthritis, ovarian and pancreatic cancer, and primary and metastatic hepatic tumors. This technique is particularly effective in treating arthritis, delivering a targeted dose to the membrane for treatment or ablation of synovium and reducing joint effusion. In the treatment of ovarian cancer, the microspheres are introduced through the abdominal cavity and deliver radiation to the cancer

cells. Microsphere brachytherapy has also been effective in controlling growth in benign cystic brain lesions, craniopharyngioma, as well as pancreatic and hepatic tumors.

One of the first beta-emitters used in microsphere brachytherapy for the treatment of lung tumors was  $^{198}\text{Au}$  (size 30-50  $\mu\text{m}$ ). However,  $^{198}\text{Au}$  also emits high-energy  $\gamma$ -rays (0.985% gamma yield of 1087.8 keV photons and 98.99% gamma yield of 418 keV photons) (Spillane et al., 2007). The high yield of gamma emissions (greater than 99%) that follows the beta decay led to high radiation exposure to the other organs of the patient, as well as to the caregivers. In an attempt to overcome this issue, pure beta-emitters, such as Phosphorous-32 ( $^{32}\text{P}$ ) and Yttrium-90 ( $^{90}\text{Y}$ ) became the predominant radioisotopes for many therapeutic applications during the past decade. Recently, however, it has been shown that a few percent of low-energy  $\gamma$ -radiation can actually be useful for imaging, either during or after the delivery of the microspheres (Hoesler et al., 2004). With the help of gamma cameras, the surgeons are able to direct the radioactive microspheres and adjust the necessary amounts of radioactivity during the process of microsphere embolization (Häfeli, 2001).

It has been shown that not only is the total dose delivered important for predicting treatment outcome in radiotherapy, dose rate is also an important parameter (Hall and Brenner, 1992). Short-lived radioisotopes may be used to optimize radiobiologic aspects of therapy. Short-lived radioisotopes such as Dysprosium-165 ( $^{165}\text{Dy}$ ) and Rhenium-188 ( $^{188}\text{Re}$ ) deliver the total dose in a much shorter period of time, allowing less time for tumor cells to recover and repopulate. Although there is still a need for more research in this area, beta-emitting lanthanides are seen as promising for microsphere brachytherapy.

Several beta emitters, such as  $^{90}\text{Y}$ , Samarium-153 ( $^{153}\text{Sm}$ ),  $^{188}\text{Re}$ ,  $^{32}\text{P}$ , Holmium ( $^{166}\text{Ho}$ ) and  $^{142}\text{Pr}$  have been studied and their use in brachytherapy and microsphere brachytherapy has been increasing (Kennedy et al., 2006; Sadeghi et al., 2010; Fischer and Kampen, 2012; Conzone et al., 1998; Oehme and Kotzerke, 2009; Coursey and Nath, 2000; Turner et al., 1994; Squair et al., 2012; Lee and Reece, 2005; Jung and Reece, 2008). The most popular radioisotope currently used in microsphere brachytherapy is  $^{90}\text{Y}$ . It is found in the form of glass or resin microsphere, under the brand names of SIR-Sphere<sup>®</sup> (Sirtex Medical Limited, North Sydney, NSW, Australia) and TheraSphere<sup>®</sup> (Nordion Inc., Ottawa, ON, Canada).

Production of  $^{90}\text{Y}$  is considered challenging and costly (Hamoudeh et al., 2008). Availability and costs are therefore limiting factors for research improvements and widespread clinical use of the technique. Another issue related to the nuclide is the difficulty of appropriate verification of the microspheres activity for quality assurance (Dezarn et al., 2011). The activity of  $^{90}\text{Y}$  microspheres is usually calculated based on the time elapsed since the sample was produced, the half-life, and initial activity provided by the vendor. Direct verification of the total activity at the treatment site has been challenging because  $^{90}\text{Y}$  is mostly a beta emitter (it also undergoes internal pair production determined to be  $31.87 \pm 0.47 \times 10^{-6}$ ) (Gates et al., 2011). This presents an issue if only part of the total activity of the microspheres will be used for treatment. The gamma component of  $^{142}\text{Pr}$  would allow a direct verification of the remaining sample activity and therefore a better estimation of the dose delivered to the patient.

Another important factor to consider is the biological effective dose (BED) received by the hepatic parenchyma and HCC, which varies greatly with the radionuclides used. This property is related to the dose delivery time of the radionuclide, as well as the rate of growth and

repopulation, repair rate, and other biological factors of the tumor or tissue considered (Hall, 2000). Dose delivery time is mainly related to the radionuclide half-life. Optimization of half-life to obtain the maximum efficiency in delivering the total dose has been studied previously. Armpilia et al. (2003) considered biological factors and tumor growth rates applied in the quadratic model for the assessment of BED values. Results obtained by Armpilia et al. suggest that radionuclides with shorter half-life may produce better clinical results. However, the shorter half-life may also give a higher dose to normal tissues. Therefore special care is necessary not to cause failure of selective delivery, i.e lung shunting (Oehme and Kotzerke, 2009; Cremonesi et al., 2008; Dale, 1996). Lung shunting is characterized by the intake of microspheres by the lungs and it may be more prominent in some patients than others.

In the present work  $^{142}\text{Pr}$  was studied as a possible choice of radionuclide for microsphere brachytherapy. The contribution to the total dose and dose distribution due to the beta and gamma emission of  $^{142}\text{Pr}$  was studied and compared with the dose distribution due to  $^{90}\text{Y}$  (a pure beta emitter). Tumors and blood vessels were modeled and simulated using MCNPX2.6 (Monte Carlo Team, 2008) (Monte Carlo Team, 2008). Dose distributions due to both nuclides were calculated and compared. This study aims to evaluate the feasibility of the radionuclide  $^{142}\text{Pr}$  as a possible nuclide for microsphere brachytherapy. This work includes modeling of single blood vessel and simulation of the dose distribution, direct measurements of dose delivered by microspheres, and Monte Carlo validation with experimental data.

### **1.3 Ocular Squamous Cell Carcinoma (OSCC) and $^{142}\text{Pr}$ Eye Brachytherapy**

According to the American Cancer Society (ACS Eye Cancer, 2013), an estimated 2,610 cases of cancer in the eye and eye orbit will be diagnosed in 2013 (1,310 males, 1,300 females),

with an estimated 270 deaths (120 males, 150 females). Secondary eye cancer, metastasized from other organs, is more common than primary eye cancers. Eye cancer can occur at any age, but most commonly occurs in patients over age 50. The two main types of eye cancer are retinoblastoma and melanoma. Retinoblastomas are more common among children under age five. Malignant melanomas present on average at age 60 to 65. These tumors may cause pain and impair vision. These tumor types may metastasize to the optic nerve, brain, and eye orbit. Early detection and treatment is important to prevent sight losses and spread of the disease.

There are currently several modalities available to treat eye tumors. The most common techniques are: eye plaque brachytherapy (Chiu-Tsao et al., 2012), external beam radiotherapy (photon and proton), photocoagulation and photodynamic therapy, chemotherapy, cryotherapy (freezing affected area), and enucleation (removal of the eyeball). Resection of the tumors may cause sight loss and may not prevent disease recurrence in the eye or eye orbit.

Currently available low dose rate (LDR) brachytherapy techniques have shown low recurrence rates, but may be followed by severe side effects, such as permanent loss of the eyelashes and progressive visual acuity deterioration, among others (Nag et al., 2003). Conventional eye brachytherapy is based on standard spherical shaped plaques (Supe et al., 1975). These plaques present some geometrical limitations. Eye plaques were designed to deliver uniform fields to the eyeball, restricting the options for planning a tumor specific dose distribution. Advances have been made in other branches of brachytherapy that allow the delivery of a conformal dose to the tumor, e.g. after load seed implantation for prostate cancer and gynecologic interstitial implant (Thibault and Vigneault, 2011), and microsphere brachytherapy for liver cancer treatment. For episcleral eye brachytherapy however, the current

eye plaque is limited to a circular concave shape to fit the eyeball. These plaques do not take into account the specific patient eye anatomy or the specific tumor shape.

In order to overcome the limitations of the present method, the proposed device was designed to deliver a more conformal dose throughout the tumor, taking into account patient specific tumor shape and eye anatomy, as well as providing a faster dose delivery. High dose rate (HDR) brachytherapy using beta emitters can treat superficial tumors in few minutes, as opposed to LDR, which typically takes several days. Penetration of this type of radiation in tissue is small and healthy structures in the treated eye can be spared from unwanted radiation.

A conformal eye applicator, or conformal eye brachytherapy (CEBT) device, was developed in this work. It was intended to improve the current state and concept of eye plaque brachytherapy, by proposing a more conformal and patient specific dose profile. The novel device has to fulfill three primary treatment requirements: (i) to improve the spatial precision of the dose delivered to the target volume, (ii) to increase the tumor control probability while decreasing tissue complications by sparing the surrounding healthy tissue and increasing the total dose delivered to the target and (iii) to optimize the treatment effectiveness by increasing the dose rate and decreasing the treatment time.

Current methods used in eye plaque brachytherapy do not allow planning for a tumor specific dose distribution. Eye plaques consist of a small pre-molded concave metal plaque, which is used as a base for inserting radioactive seeds. The plaque is then sewn on to the sclera, where it stays for several days. In this technique, a homogeneous dose distribution is delivered throughout the eye surface, irradiating a significant amount of healthy tissue with the prescription dose. As a consequence, the patient may develop severe side effects, including loss

of sight. Traditional eye plaque design is suitable for round, homogeneous tumors. However, most of the tumors present nonhomogeneous shapes with variable sizes.

The conformal eye brachytherapy (CEBT) device allows the physician to plan a treatment based on patient specific anatomy and tumor shape and size, allowing for a more conformal dose to the tumor volume. This technique was inspired by the concept of intensity modulated radiation therapy (IMRT), in which photon fluence can be controlled to deliver a targeted dose to the tumor. IMRT uses a segmental approach to achieve a final desired dose to the target. To achieve the planned dose to the target, the multi-leaf collimator shapes the beam into different patterns. The segments can be overlapped in order to form a three-dimensional dose distribution within the patient. However, for the CEBT the dose will be limited to the surface and shallow depths, since its proposition uses a beta-emitter and most of the dose will be limited to within a few millimeters of the eye surface. In the proposed device, the radioactive sources are independently controlled by a computed system. They are free to move and can be positioned in different arrangements, allowing several fields to overlap to meet the desired dose distribution to the target.

In this work, the CEBT device design is described. The viability of  $^{142}\text{Pr}$  as a radionuclide for treating OSCC is studied using MCNPX2.6 Monte Carlo Simulation. A priori this device is proposed specifically for eye tumors. However, based on its geometric characteristics and physical properties, it may be suitable for treating other types of superficial tumors. Due to the highly localized doses delivered by this device, its use could be extended to the treatment of body sites such as melanomas and squamous cell carcinomas, or cancer located in the eyelid, ear, nose, lip, fingers, toes, tongue and sexual organs (Sedda et al., 2011). The device was designed

to be reusable after proper sterilization and radionuclide reactivation. Total dose can be delivered within a few minutes because of the high dose rate provided by short-lived nuclides such as  $^{142}\text{Pr}$ . No surgical procedure is necessary, so treatment can be performed on an outpatient basis. The procedure does not require source implantation, so there is no need for patient isolation from family and caregivers after treatment. In summary, the three main aims of this proposal are: (i) to design a conformal eye brachytherapy (CEBT) device for a tumor specific treatment, (ii) to perform simulations and dose distribution measurements within the modeled eyeball for the nuclide proposed, and (iii) to simulate and compare different nuclides and their dose distribution for the eye applicator. Future work includes: (i) to develop a planning system to customize the radiation coverage for a target volume, and (ii) to develop a quality assurance method for verification of the device and treatment plan.

#### **1.4 MCNPX2.6 Monte Carlo Radiation Transport Code**

MCNPX, Monte Carlo N-Particle eXtended, is a general-purpose Monte Carlo radiation transport code for modeling the interaction of radiation with matter. MCNPX extends the capabilities of previous versions of MCNP code by allowing the tracking of more particles, wider energy ranges, and by allowing a wider variety of applications to be simulated. The code was developed and is maintained by the Los Alamos National Laboratory (LANL) and uses Monte Carlo (MC) method for simulation of the particle tracks. MCNPX2.6 (Monte Carlo Team, 2008) is an extension of MCNP5. Simulations were benchmarked with accepted results from the literature for known dose distributions (Berger, 1971). MCNPX2.6 has a broad available nuclear data library, in regard to cross-sections for different particles and energy. It has numerous

applications in radiation measurements, such as high-energy dosimetry and neutron detection and in Medical physics, especially proton and neutron therapy.

Convolution techniques are often used for photon and electron dose calculation. These methods are fast and have a good agreement with Monte Carlo simulations for simple geometries (Mainegra-Hing et al., 2005). Convolution techniques calculate the total dose by convolving the total energy released per unit mass with a dose point kernel (DPK), which is the radial distribution of dose around an isotropic point source in an infinite water medium. DPK is used to calculate dose delivered by electrons and has no angular information.

Dose rates due to  $^{142}\text{Pr}$  and  $^{90}\text{Y}$  point sources were calculated using the BRAIN-DOSE DPK code (Dauffy, 1998). The BRAIN-DOSE code is based on SADDE (Reece et al., 1989) and VARSKIN (Traub et al., 1987) codes. BRAIN-DOSE code uses the dose point kernel (DPK) method to integrate the Berger point kernels over the source volume using the scaled point kernels tabulated by Berger (1971):

$$B(\rho, E) = \frac{1}{4\pi\delta\rho^2} \int_0^{E_{max}} \frac{EN(E)}{X_{90}} F\left(\frac{\rho}{X_{90}}, E\right) dE \quad \text{Eq. 1.1}$$

Where  $\rho$  is the distance between source point and dose point (cm);  $\delta$  is the density of the irradiated medium (value used was 1.00 g/cm<sup>3</sup> for water);  $N(E)$  is the probability that a  $\beta^-$  particle is emitted with Energy  $E$ ;  $X_{90}$  is the radius (cm) of the sphere within which 90% of the beta energy is deposited from a point source in an infinite medium; and  $F$  is a function of  $\rho$  and  $X_{90}$  and represents the dimensionless scaled absorbed dose distribution.

Dose rates for point sources using both nuclides were calculated using the MCNPX2.6 Monte Carlo code. It has been shown that MCNPX2.6 can be used successfully for the calculation of dose distributions for electrons when using ITS-style (DBCN 18 card=1), also called the “nearest group boundary” treatment, and it has been shown to be in agreement with other versions of MCNP code (Nedaie et al., 2006; Schaart et al., 2002). It can be used for calculating several particle types, such as neutron, photon, electron, or coupled neutron/photon/electron transport. Secondary radiations such as positrons, K-edge characteristic x-rays, and bremsstrahlung are included in the default modeling of MCNPX2.6.

The continuous-slowing-down model is used for the electron transport simulation. This model takes into account several factors, including electron energy, total path length and total stopping power of the electron, the electron collisional stopping power due to collisions between particle and atoms, the electron radioactive stopping power due to energy loss during interactions with the Coulomb force field of the atoms or Bremsstrahlung, statistical variations in the amount of energy lost in each collision, or energy straggling, and multiple scattering distributions.

The geometry of the sources was modeled and a series of three-dimensional mesh tallies (finite volumes used as detectors by MCNPX2.6 for the 3D mapping of the energy deposited in the medium) were positioned along the dose tally points. The energy cutoff used both electron and photon was 0.001 MeV, which is the default value used by MCNPX2.6 for these particles. The number of source electron histories (NPS) was chosen so that there was less than 1.5 % statistical error for the points of interest, such as the points close to the source. To obtain less than 1.5 % statistical error at least  $2.0 \times 10^7$  NPS were required per simulation. The “ITS-style” energy-indexing algorithm (DBCN 18 card=1) was used. The default ESTEP parameter (number

of sub-steps per energy step depends on the material in which the electrons are traveling and ranges from 2 for  $Z = 3$  to 15 for  $Z > 90$ ) was defined in the material card (Reynaert et al., 2002).

### 1.5 Biological Effective Dose (BED) and the Linear Quadratic (LQ) Model

It is useful to have a quantitative method of comparing treatment effectiveness. The Linear Quadratic (LQ) model is the most widely used method for comparing effective dose in radiotherapy. In this model, the biological effect is not only a function of dose but also the dose rate at which the radiation is delivered. The tissue radiosensitivity to a given radiation type is modeled by the parameters  $\alpha$  and  $\beta$ . According to the LQ model (Lea and Catcheside, 1942; Lea, 1947; Fowler, 1989; Antipas et al., 2011; Armpilia et al., 2013), the percent survival of cells as a function of dose is given by:

$$S = e^{-\alpha D - \beta D^2} \quad \text{Eq. 1.2}$$

The Biological Effective Dose (BED) values were calculated for both  $^{142}\text{Pr}$  and  $^{90}\text{Y}$ . Considering the relative biological effectiveness ( $RBE$ ), the BED is calculated as the prescribed total dose ( $TD$ ) times the relative effectiveness ( $RE$ ) factor minus biological equivalent of the tumor repopulation ( $BRF$ ):

$$BED = (TD)(RE) - BRF \quad \text{Eq. 1.3}$$

Each term of this equation will be defined in the following equations. The total dose is expressed as:

$$TD = \frac{R_0}{\lambda} [1 - e^{(-\lambda T_{eff})}] \quad \text{Eq. 1.4}$$

where,  $R_0$  is the initial dose rate,  $\lambda$  is the radionuclide decay constant ( $h^{-1}$ ), and  $T_{eff}$  is the effective treatment time ( $h$ ), given by:

$$T_{eff} = -\frac{1}{\lambda} \ln \left( \frac{K}{RBE_{max} R_0} \right) \quad \text{Eq. 1.5}$$

with  $K$  being the tumor repopulation factor (Gy/h), the biological dose required to offset each day's worth of tumor repopulation, given by:

$$K = \ln(2)/(\alpha DT) \quad \text{Eq. 1.6}$$

and  $RBE_{max}$  is the maximum  $RBE$  defined as the ratio of linear sensitivity coefficient ( $\alpha$ ) for high LET test radiation to that for a reference low LET radiation.  $RBE_{max}$  used in these calculations was 1.0. The relative effectiveness ( $RE$ ) can be expressed as:

$$RE = RBE_{max} + \left[ \frac{2R_0\lambda}{(\mu_{tum} - \lambda)(\alpha/\beta_{tum})} \right] A(B - C) \quad \text{Eq. 1.7}$$

where  $A$ ,  $B$ , and  $C$  are defined as:

$$A = \frac{1}{1 - \exp(-\lambda T_{eff})}, \quad \text{Eq. 1.8}$$

$$B = \frac{1 - \exp(-2\lambda T_{eff})}{2\lambda}, \quad \text{Eq. 1.9}$$

$$C = \frac{1 - \exp[-T_{eff}(\mu_{tum} + \lambda)]}{\mu_{tum} + \lambda} \quad \text{Eq. 1.10}$$

with  $\mu_{tum}$  being the sublethal damage repair constant ( $\text{h}^{-1}$ ),  $(\alpha/\beta)_{tum}$  the inverse fractionation factor of the tumor (Gy),  $\alpha$  the linear radiosensitivity coefficient ( $\text{Gy}^{-1}$ ), and  $DT$  the average clonogen doubling time (h).

## 1.6 Beta Emitter Praseodymium-142: Radionuclide Properties

The production of several radionuclides, including  $^{32}\text{P}$ ,  $^{90}\text{Y}$  and  $^{142}\text{Pr}$ , is performed by means of neutron activation (NA) in neutron reactors. This method consists of bombarding the parent atoms with a flux of neutrons. The activity reached through NA is proportional to the number of atoms in the sample, the neutron flux in the reactor, the neutron energy, the parent

neutron absorption cross section and the amount of time that the parent is exposed to the neutron flux. Details of neutron activation parameters are discussed in Section 1.8 Radionuclide Production. Radionuclides with higher activation cross-section reach a higher saturation activity than ones with lower activation cross-section. Therefore, smaller cross sections require higher neutron fluence for activation (the most commonly used unit for cross section is *barn*, where 1 barn =  $10^{-24}$  cm<sup>2</sup>). For instance, <sup>32</sup>P has a smaller thermal neutron absorption cross-section of the parent (0.18 barn) and lower beta maximum energy ( $E_{\max}$  1.709 MeV) when compared to <sup>90</sup>Y (cross section of the parent  $\sigma$  = 1.28 barn and  $E_{\max}$  =2.284 MeV). On the other hand, <sup>142</sup>Pr presents a higher neutron absorption cross-section of the parent (11.40 barn) and relatively high maximum beta energy ( $E_{\max}$  2.162 MeV). The higher neutron absorption cross-section of the parent for <sup>142</sup>Pr when compared to <sup>90</sup>Y (1.28 barn) allows for faster production and allows for the possibility of activation in low neutron fluence reactors. Some authors also suggest the possibility of activation of <sup>142</sup>Pr using cyclotrons (Sadeghi et al., 2011).

## 1.7 Electron maximum range

Maximum range in tissue for several beta emitter nuclides used in therapy are shown in Table 1.1. The maximum range of electron emitted by these nuclides can be calculated using the empirical formula (Katz and Penfold, 1952):

$$R_{max}[g/cm^2] = 0.412 E_{\beta}^{1.265 - 0.0954 \ln E_{\beta}} \quad \text{for } 0.01 \leq E_{\beta} \leq 2.5 \text{ MeV} \quad \text{Eq. 1.11}$$

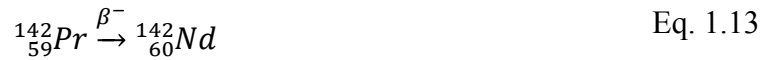
where  $E_\beta$  is the maximum beta energy in MeV. Range in Eq. 1.11 is expressed as a density thickness ( $\text{g}/\text{cm}^2$ ) and it is material independent. The range, expressed as a distance, can be calculated for different materials by dividing  $R_{max}$  by the material density. For instance, the maximum electron range for  $^{142}\text{Pr}$  in water is 10.3 mm, which is comparable to the maximum range for  $^{90}\text{Y}$  (10.9 mm), and for  $^{32}\text{P}$  this value is 7.90 mm.

### 1.8 Decay modes of Praseodymium-142

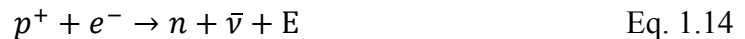
$^{142}\text{Pr}$  has a half-life of 19.12 hours and undergoes two decay modes: beta-minus emission ( $\beta^-$ ) and electron capture (EC). In the beta-minus decay (99.98%), a neutron in the  $^{141}\text{Pr}$  nucleus is transformed into a proton and electron:



An electron and an antineutrino is ejected from the nucleus and carry away the energy in form of kinetic energy. The kinetic energy released is shared between the neutrino and electron. The antineutrino is a weakly interacting elementary subatomic particle that undergoes essentially no interactions with matter and is practically undetectable. The energy for the beta-minus forms a spectrum, in which the mean energy may be approximated by  $\bar{E}_\beta \approx (1/3)E_\beta^{max}$ . The maximum beta energy for  $^{142}\text{Pr}$  is 2.162 MeV and its average beta energy is 0.809 MeV. In the standard nuclear notation, this decay is represented as:



The parent isotope and daughter are different elements with same mass number  $A$ . This decay is therefore an isobaric decay mode that results in a transmutation of elements. The daughter  ${}^{142}\text{Nd}$  is a stable nuclide. In the electron capture mode (0.0164%), one orbital electron is captured by the nucleus and combines with a proton to form a neutron:



in the standard nuclear notation, this decay is represented as:



This is an isobaric decay that also results in a transmutation of elements. The daughter  ${}^{142}\text{Ce}$  is also a stable element.

## 1.9 Radionuclide Production

Production mode of  ${}^{142}\text{Pr}$  may be achieved by either fast neutron activation or thermal neutron activation of  ${}^{141}\text{Pr}$ . The amount of activity produced in a sample irradiated with a particle beam will depend on the number of nuclei being irradiated, the flux of neutrons hitting the sample and the probability of interaction of the neutron with the atoms. The probability of

interaction is represented by the activation cross-section  $\sigma$  (barn). When the sample is irradiated with a constant neutron flux  $\phi$ , the activity builds up from zero and approaches a saturation activity in which the nuclide disintegration rate is the same as the production rate. The saturation activity (Bq) of the material is given by:

$$A_{Sat} = N\phi\sigma \quad \text{Eq. 1.15}$$

where  $N$  is the number of atoms in the sample, given by:

$$N = \frac{mN_a}{M} \quad \text{Eq. 1.16}$$

with  $m$  being the sample mass,  $N_a$  the Avogadro's constant ( $6.022 \times 10^{23} \text{ mol}^{-1}$ ) and  $M$  the nuclide atomic mass (140.9 g for  $^{141}\text{Pr}$ ). Equation 1.15 describes the sample saturation activity (Bq) for the cases where the nuclide is 100% abundant in the irradiated sample. If the isotope is not 100% abundant then the saturation activity should be reduced by the nuclide abundance percentage. The irradiated sample must be sufficiently thin in order for Eq. 1.15 to hold. If the sample is significantly thick, the neutron flux may be attenuated as it penetrates the target. The mass of the irradiated samples for the present work were small (0.169 g for the microspheres and 0.35 g for each glass rod) and therefore Eq. 1.15 was used. Details of the sample sizes and dimensions used are discussed in CHAPTER 3: MATERIALS AND METHODS II: EXPERIMENTAL DESIGN. The dependency of the activity on the irradiation time is given by:

$$A(t) = A_{sat}(1 - e^{-\lambda t}) \quad \text{Eq. 1.17}$$

where  $\lambda$  is the decay constant of the product nuclide.

$$\lambda = \frac{\ln(2)}{T_{1/2}} \quad \text{Eq. 1.18}$$

and  $T_{1/2}$  is the radionuclide's half-life. The calculated activation times and total activities are presented in CHAPTER 4: RESULTS.

### **1.10 GAFCHROMIC<sup>®</sup> EBT2 Dosimetry Film**

Film dosimetry is a powerful tool for radiotherapy treatment verification and quality assurance. Over the years there have been significant improvements in the sensitivity and uniformity as two-dimensional detectors (Devic, 2011). Recently, film dosimetry has gained increased popularity in brachytherapy, diagnostic radiology, and radiobiological experiments. Two-dimensional arrays of diodes or ion chambers can produce results in real time, but film has the advantage of higher spatial resolution (25  $\mu\text{m}$ ). The spatial resolution of dosimeters is limited by the finite nature of dosimeter size and collecting volume. In the microscopic scale, the spatial resolution is limited by the stochastic nature of energy deposition in matter. GAFCHROMIC<sup>®</sup> EBT2 Dosimetry film is self-developing and does not require any film processing. It is energy independent, presenting minimal response differences from 100 keV into the MV range for both photons and electrons (Arjomandy, 2010). It is designed for quantitative dose measurements in

radiotherapy, and it is widely used in intensity modulated radiation therapy (IMRT) and brachytherapy, in which high dose gradients occur. It has also been shown that the dose response for GAFCHROMIC<sup>®</sup> EBT2 is independent of fractionation, dose rate and depth dependence in electron beams (Gerbi *et al.*, 2009). The EBT2 film has near-tissue equivalent electron density ( $Z_{\text{eff}}^{\text{EBT2}} = 6.84$  compared to  $Z_{\text{eff}}^{\text{water}} = 7.3$ ). Also, it is water resistant, and can be immersed for hours in water phantoms. It is stable in room light and temperatures up to 60 °C.

GAFCHROMIC<sup>®</sup> EBT2 film (Figure 1.1) is comprised of a single 30 μm thick active layer coated on a clear polyester substrate of 175 μm and covered with a 25 μm adhesive layer topped with a 50 μm polyester overlamine. The active layer contains marker dye and stabilizers that undergoes changes in color upon irradiation. The optical density of the film can be expressed as:

$$OD = \log\left(\frac{I_0}{I}\right) \quad \text{Eq. 1.19}$$

where  $I_0$  is the intensity of light transmitted by the unexposed film and  $I$  is the intensity of light transmitted through the exposed film.

The active layer incorporates a yellow dye, which enables multi-channel (RGB) dosimetry and decreases the UV and light sensitivity. The multi-channel feature allows analyzing red, green and blue channels separately. Each channel presents a different darkening response to the dose absorbed. For instance, the blue channel exhibits a low slope because the signal is dominated by a dose independent contribution. On the other hand, the red channel presents a high slope curve,

due to the strong dose dependence of the signal in this channel. Previous studies have shown that red-channel data calibration done at standard megavoltage electron energies yields the best accuracy regardless of the energy (Kairn and Aland, 2013). Red-channel was used for the dose calibration curve. Film sensitivity limits in the red channel goes from 1 cGy to 10 Gy. Dose can be derived from the optical density if the film is properly calibrated with an absolute dosimeter such as a NIST traceable ion chamber.

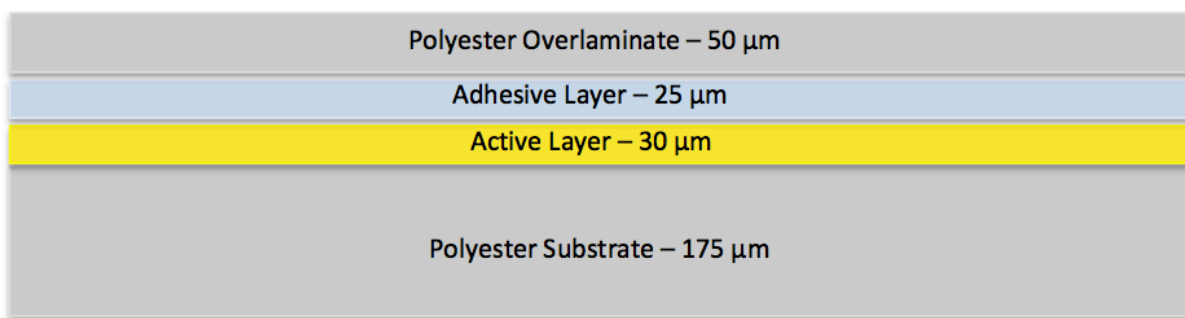


**Figure 1.1** Cross-section of a GAFCHROMIC<sup>®</sup> EBT2 film sheet and view of the asymmetric structure ([http://online1.ispcorp.com/\\_layouts/Gafchromic/content/products/ebt2/pdfs/GAFCHROMIC EBT2 Technical Brief-Rev1.pdf](http://online1.ispcorp.com/_layouts/Gafchromic/content/products/ebt2/pdfs/GAFCHROMIC%20EBT2%20Technical%20Brief-Rev1.pdf).)

### 1.11 Specific Aims

The fundamental question in the current clinical practice of radiation therapy is how to balance the optimization of tumor control with the minimization of post radiation therapy complications for the patient. The use of beta-minus emitters in brachytherapy has been increasing for both benign and malignant tumors (Sedda et al., 2012), as it represents a more targeted radiation therapy. Physical characteristics of beta radiation, such as the short penetration in tissue, allow the deposition of high doses to small volumes, avoiding unwanted doses to the

surrounding healthy tissues. In this proposal the beta emitter Praseodymium-142 ( $^{142}\text{Pr}$ ) is studied.  $^{142}\text{Pr}$  is a dual beta-minus/gamma emitter with a half-life of 19.12 h. It undergoes beta decay (96.3%), with maximum beta energy of  $E_{\beta^-} = 2.162$  MeV and presents a gamma emission (3.7%) with energy  $E_{\gamma} = 1.575$  MeV. It also presents a high neutron absorption cross-section of parent (11.40 barn including meta-stable state).  $^{142}\text{Pr}$  microspheres and seeds have been previously proposed for the treatment of prostate cancer and arteriovenous malformation (Jung and Reece, 2008; Lee and Reece, 2005).  $^{142}\text{Pr}$  can be easily activated in research facilities or clinics equipped with a low neutron flux reactor such as the 1 Megawatt TRIGA (Training, Research, Isotopes, and General Atomics). Two innovative applications for this radionuclide are presented:  $^{142}\text{Pr}$  Glass Microsphere brachytherapy for treating Hepatocellular Carcinoma (HCC), and a novel  $^{142}\text{Pr}$  eye applicator for treating Ocular Squamous Cell Carcinoma (OSCC).

The overall goal of this work is to study the radionuclide  $^{142}\text{Pr}$  as a brachytherapy source, covering the possible benefits and issues related to the use of this beta emitter in microsphere brachytherapy and eye plaque brachytherapy, as well as propose a new device for dosimetric studies of dose distribution due to this nuclide. Both MCNPX2.6 Monte Carlo simulations and experimental measurements of the proposed brachytherapy sources were performed. Detailed radiobiological studies of the biological effects of this high dose rate nuclide in tissues and organs are studied using the well-known Linear Quadratic (LQ) Model (Armpilia et al., 2003). Specific applications of this radionuclide are (i)  $^{142}\text{Pr}$  microsphere brachytherapy for treating HCC and liver metastasis (ii)  $^{142}\text{Pr}$  glass eye applicator, an innovative device for brachytherapy of OSCC.

## CHAPTER 2: MATERIALS AND METHODS I: THEORY AND SIMULATIONS

### 2.1 $^{142}\text{Pr}$ MICROSPHERE BRACHYTHERAPY

#### 2.1.1 Clinical Activity and Tumor Target Dose

Source activity for TheraSphere<sup>®</sup> ( $^{90}\text{Y}$  glass microsphere) is calculated based on the nominal target dose and patient's liver mass (Kennedy et al., 2007). The treatment prescription dose considered for brachytherapy is between 120 to 180 Gy. In this study a dose of 150 Gy was considered for calculation and simulation purposes. The same total physical dose was considered for  $^{142}\text{Pr}$  and  $^{90}\text{Y}$  in order to compare the effects for a fixed dose.

#### 2.1.2 Physical and Radiobiological Properties

Several physical and radiobiological aspects, including physical half-life, dose distribution and biological effective dose for  $^{142}\text{Pr}$  and  $^{90}\text{Y}$  were also compared in this work. Table 2.1 and 2.2 list the properties of beta emitters and the composition of rare earth aluminosilicate (REAS) and yttrium aluminosilicate (YAS) glasses. The time to deliver 90% of the dose ( $T_{90}$ ) for  $^{142}\text{Pr}$  (2.65 days) is approximately 30% of  $T_{90}$  for  $^{90}\text{Y}$  (8.86 days). This is one advantage of  $^{142}\text{Pr}$  over  $^{90}\text{Y}$ , since the longer the treatment time the higher is the risk of dose contamination to healthy tissue due to migration to adjacent organs (especially to lungs) (Kennedy et al., 2007).  $^{142}\text{Pr}$  rare earth REAS glass is composed of 15.5% Silica, 8.1% Aluminum, 44.5% Praseodymium, and 32.1% Oxygen.

**Table 2.1:** Physical properties of beta emitters used in microsphere brachytherapy (Häfeli, 2001)

Property	<sup>142</sup> Pr	<sup>90</sup> Y	<sup>32</sup> P
Half life	<b>19.12 h</b>	64.0 h	342.7 h
Time to deliver 90% of the dose	<b>2.65 days</b>	8.86 days	47.4 days
Maximum beta energy (MeV)	<b>2.162</b>	2.281	1.709
Average beta energy (MeV)	<b>0.809</b>	0.934	0.695
Maximum Range in Tissue <sup>†</sup> (mm)	<b>10.3</b>	10.9	7.90
Density of glass (g/cm <sup>3</sup> )	<b>4.0</b>	3.29	3.06
Gamma emissions for imaging	<b>Brems<sup>§</sup></b> <b>1.58 MeV, γ(3.7%)</b>	Brems <sup>§</sup>	Brems <sup>§</sup>
Thermal neutron cross section	<b>7.5 b (+3.9 b)<sup>‡</sup></b>	1.28 b	0.17 b

<sup>†</sup> Calculated using Eq. 1.11 (Katz and Penfold, 1952).

<sup>§</sup> Bremsstrahlung.

<sup>‡</sup> Cross section of meta-stable state.

**Table 2.2:** Composition of  $^{142}\text{Pr}$  and  $^{90}\text{Y}$  glass microspheres.

<b>Element</b>	<b><math>^{142}\text{Pr}^{\text{a}}</math></b>	<b><math>^{90}\text{Y}^{\text{b}}</math></b>
Si	<b>0.153</b>	0.194
Al	<b>0.081</b>	0.106
Pr	<b>0.445</b>	0
Y	<b>0</b>	0.303
O	<b>0.321</b>	0.397
Total	<b>1.000</b>	1.000

<sup>a</sup> Composition of  $^{142}\text{Pr}$  REAS glass (Jung and Reece, 2008)

<sup>b</sup> Composition of  $^{90}\text{Y}$  YAS glass (Poorbaygi et al., 2011)

## *Radiobiological Effective Doses for $^{142}\text{Pr}$ and $^{90}\text{Y}$*

A numeral software package, Mathematica<sup>®</sup> 8 (Wolfram Research, Champaign, IL) was used to perform the BED calculations. BED values for both  $^{142}\text{Pr}$  and  $^{90}\text{Y}$  given different values of HCC clonogenic doubling times (DTs) were calculated. BED varies with the radionuclide properties, the tumor radiobiological factors and the tumor DT. HCC doubling times vary greatly according to the tumor types: well, moderately or poorly differentiated. The rate of tumor growth can be classified as: slow (DT > 100 days); intermediate (50 days < DT < 100 days); or rapid (DT < 50 days). The distribution of DT values within each group is positively skewed, with some tumors presenting very long DT values compared to the mean value. For this reason, ranges of values were considered for BED calculation, rather than using mean values. DT values for each group were classified as: well differentiated (38-720 days), moderately differentiated (17-380 days) and poorly differentiated HCCs (20-70 days), based on clinical values obtained in previous studies (Mehrra et al., 2007). An  $\alpha/\beta$  value of 10 Gy (tumoral liver), and a total physical dose (PD) of 150 Gy was used for both radionuclides. A total physical dose (PD) of 10 Gy and an  $\alpha/\beta$  value of 2.5 Gy was used for the healthy liver tissue, based on  $\alpha/\beta$  values previously reported in the literature (Cremonesi et al., 2008). Total time to deliver 90% of the prescribed dose was estimated for  $^{90}\text{Y}$  and  $^{142}\text{Pr}$  by calculating the total time from the microsphere embolization procedure up to the time that only 10% of the initial activity is remaining in the patient's system. A total physical dose (PD) of 150 Gy was considered for both radionuclides studied. The initial dose rate  $R_0$  was calculated by dividing the total physical dose by the mean life of the nuclide. Comparison between the total times to deliver 90% of the prescribed total dose of 150 Gy was also performed for  $^{90}\text{Y}$  and  $^{142}\text{Pr}$ .

### 2.1.3 MCNPX2.6 Monte Carlo Simulations

#### *Praseodymium-142 versus Yttrium-90*

In order to evaluate the feasibility of  $^{142}\text{Pr}$  in microsphere brachytherapy, we analyzed dose distribution using MCNPX2.6, BRAIN-DOSE code and analytical calculations and compared with the dose distributions produced by  $^{90}\text{Y}$ . Figure 2.1 shows the beta spectrum for  $^{142}\text{Pr}$  and  $^{90}\text{Y}$  (Cross et al., 1983) used for the MCNPX2.6 source energy input.

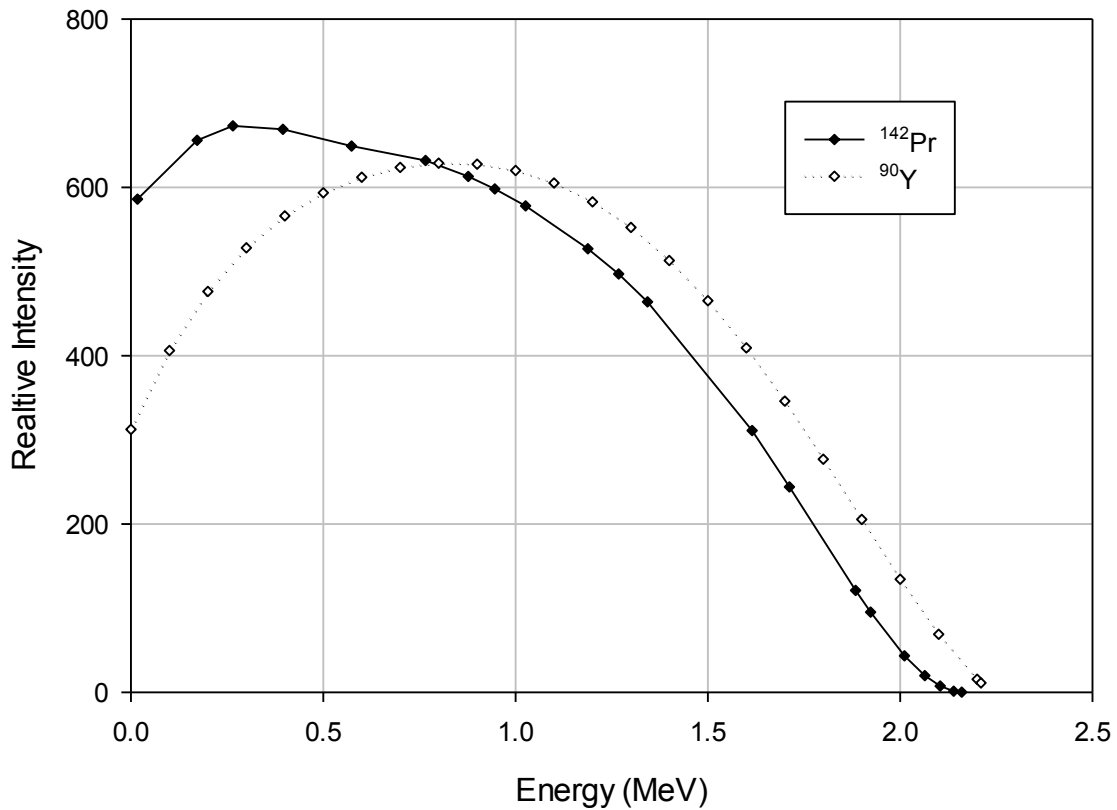


**Figure 2.1**  $^{142}\text{Pr}$  and  $^{90}\text{Y}$  Beta energy spectrum used for MC simulation.

Calculations using BRAIN-DOSE code (Dauffy, 1988), based on dose point kernel (DPK) method, and simulation using MCNPX2.6 Monte Carlo (MC) code of dose rates due to  $^{142}\text{Pr}$  and

$^{90}\text{Y}$  point sources were performed. MCNPX2.6 code simulations were performed on a computer with the following specifications: RAM: 12GB; CPU: Intel(R) Xeon(R), 12 Cores; OS: Linux Ubuntu 64 bit. Several physical and radiobiological aspects, including physical half-life, dose distribution and biological effective dose for  $^{142}\text{Pr}$  and  $^{90}\text{Y}$  were also compared.

#### *Dose distribution for a point source*

DPK calculation and MC simulation were also performed to determine the dose distribution due to a  $^{142}\text{Pr}$  point source. Dose rate for  $^{90}\text{Y}$  was calculated using DPK method and the results were compared with the benchmarked calculations from Berger, presented in the previous work from Vynckier and Wambersie (1982). Results from DPK calculations were compared with MC results. Dose rates produced by  $^{142}\text{Pr}$  and  $^{90}\text{Y}$  point sources were also calculated using the DPK method and compared at 0.5 cm away from the point sources.

#### *Dose distribution for a spherical ensemble of microspheres*

MCNPX2.6 code was used to simulate the dose delivered by a given ensemble of homogeneously distributes microspheres within a tumor for both beta and gamma contributions for  $^{142}\text{Pr}$  and for beta contributions for  $^{90}\text{Y}$ . A spherical tumor immersed in water was used in this model. The tumor size was based on the average reported sizes found in the literature with radius ranging from 1 to 5 cm (Sarfaraz et al., 2003). MCNPX2.6 was used to model the geometry of the glass microspheres distributed within the tumor for different tumor sizes and volume of surrounding water (input code can be found in Appendix A.1.1). The source was defined using the source definition (SDEF) parameters in MCNPX2.6. The source was uniformly distributed within the spherical shape. Details of the radionuclide, such as beta energy spectrum, glass

density and percent weight composition were also entered as parameters for the source definition coding. Number of source electron histories and statistical uncertainties were chosen so that there was less than 1.50 % statistical error for the points of interest. Three-dimensional mesh-tallies were defined to cover the total tumor volume and extra margin was given to access the dose deposited in the tumor vicinity. Dose rate calculations for the gamma contribution were also performed using MCNPX2.6 simulation and the analytical equation. The differences in the code for modeling the gamma component consist in changing the particle type that the MC code will track, from electron (E) to gamma (P), and changing the mesh tally distance ranges, since the gamma rays are more penetrating than electrons. The source definitions and geometries used for gamma modeling were the same as used for the electron code.

#### *Dose distribution for cylindrical blood vessels*

Dose distributions of microspheres within a single blood vessel were simulated in this paper. Post treatment liver analysis has shown that the highest concentration of microspheres is deposited at the tumor boundaries and blood vessels (Sarfaraz et al., 2004; Fox et al., 1991). The microspheres are embolized especially well within the tiny blood vessels surrounding the tumor surface, responsible for providing blood supply to the tumor. Dose distribution due to  $^{90}\text{Y}$  and  $^{142}\text{Pr}$  within blood vessels was simulated using MCNPX2.6 (input code can be found in Appendix A.1.2).

This model uses cylindrical blood vessels with diameters ranging from 25 to 75  $\mu\text{m}$  (diameters based on the average sizes reported by Kennedy *et al.*, 2004), with a length the same as the tumor diameter. Blood vessels were modeled as a cylindrical volume source. The radioisotope was uniformly distributed within the volume sources, and located in the center of a

0.2, 0.5 and 1.0 cm radius tumor. Figure 2.2 shows the model of a 50  $\mu\text{m}$  diameter blood vessel, both within and at the periphery of a 0.5 cm tumor radius. A total activity of 8,400 Bq and 2,500 Bq was used per microsphere of  $^{142}\text{Pr}$  and  $^{90}\text{Y}$ , respectively.

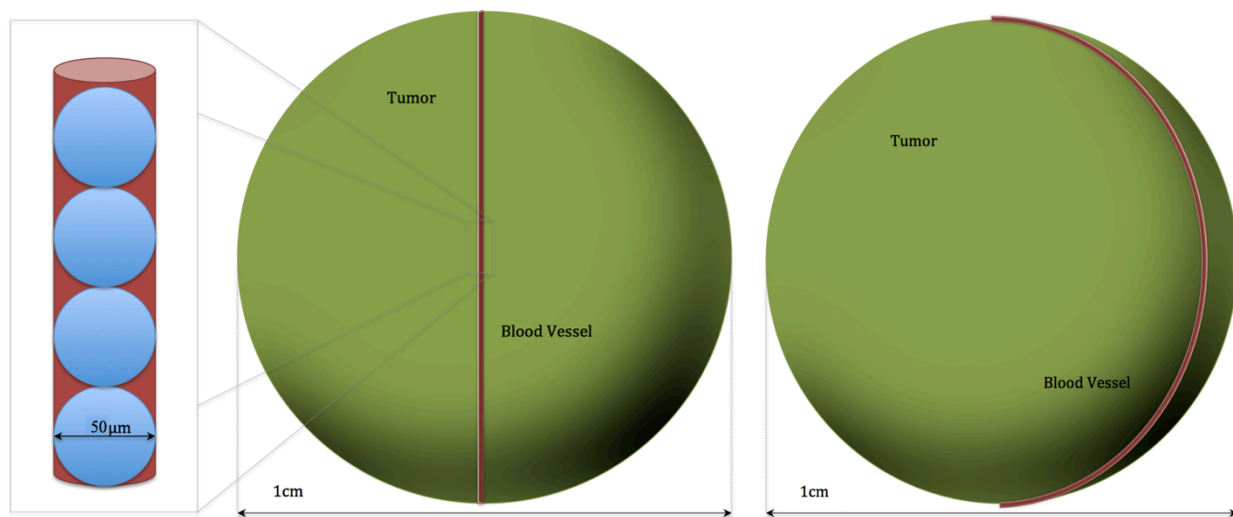


**Figure 2.2** Model of a blood vessel inside and at the periphery of a 1 cm tumor. Microspheres are embolized within the 50 $\mu\text{m}$  blood vessel.

These activities resulted in the same number of disintegrations for both nuclides during entire treatment period. The same number of disintegrations was chosen in order to calculate the total physical dose delivered by each radionuclide, for the same number of decays.

The same number of microspheres was considered for both nuclides, i.e.  $1.2 \times 10^6$  microspheres per vial (Kennedy et al., 2007), which equates to an activity of 3 GBq for TheraSphere<sup>®</sup>. In order to deliver the same physical dose, an activity of 10.1 GBq would be required for the  $^{142}\text{Pr}$  vial. The  $^{142}\text{Pr}$  gamma component may raise concerns regarding the

radiation protection of the dose due to its 3.7% gamma component. However, the specific gamma-ray dose constant,  $\Gamma$ , for  $^{142}\text{Pr}$  ( $8.050 \times 10^{-6} \text{ mSv h}^{-1} \text{ MBq}^{-1}$ ) is considerably smaller than  $\Gamma$  for other nuclides used in nuclear medicine and therapy, such as  $^{11}\text{C}$  ( $1.937 \times 10^{-4} \text{ mSv h}^{-1} \text{ MBq}^{-1}$ ) and  $^{137}\text{Cs}$  ( $1.032 \times 10^{-4} \text{ mSv h}^{-1} \text{ MBq}^{-1}$ ) at 1 meter from the source (Unger and Trubey, 1982). The ambient dose rates for  $^{142}\text{Pr}$  were calculated for a point source and compared with the limits for occupational and general public exposures.

The physical dose distribution for each case was simulated. However, in order to compare the efficacy of the treatment, the biological effective dose (BED) should be also taken into account. Therefore a Biological Effective Dose Volume Histogram (BEDVH) (Gagne et al., 2012) was plotted for each case studied, in order to determine the percent volume of the tumor receiving biological effective dose higher than 150 Gy. The target dose prescribed for microsphere brachytherapy is between 120 to 180 Gy (Dezarn et al., 2011), therefore 150 Gy was chosen to represent the average treatment target dose.

#### *Dose distribution for microspheres within a glass capillary*

In order to compare the MCNPX2.6 Monte Carlo simulations with the experimental design, a glass capillary immersed in water and filled with  $^{142}\text{Pr}$  glass microspheres was modeled in MCNPX2.6 (input code can be found in Appendix A.1.3). The capillary had an internal diameter of 305  $\mu\text{m}$  and external diameter of 453  $\mu\text{m}$ , which are the same dimensions of the glass capillary used in the experiments. The modeled glass vial had the same averaged dimensions of the capillary used in the experimental section and is described in CHAPTER 3: MATERIALS AND METHODS II: EXPERIMENTAL DESIGN. Glass composition of the capillary was taken into account in this simulation and it was the same used for the Monte Carlo

experimental validation. The following chemical composition (weight percent) was used: 74%: SiO<sub>2</sub>, 13%: Na<sub>2</sub>O, 10.5%: CaO, 1.3% Al<sub>2</sub>O<sub>3</sub>, 0.3% K<sub>2</sub>O, 0.2%: SO<sub>3</sub>, 0.2%: MgO, 0.04%: Fe<sub>2</sub>O<sub>3</sub>, 0.01: TiO<sub>2</sub>. The experimental setup for accessing the dose distribution using GAFCHROMIC<sup>®</sup> EBT2 film due to a single glass capillary is described in Chapter 4: EXPERIMENTAL DESIGN. The dose deposited per decay was analyzed in a set of 60 × 60 × 60 voxels distribute in the x, y, and z-axis. The total volume analyzed around the capillary was 5 × 5 × 5 mm<sup>3</sup>. Each voxel had a total volume of 1.157 μm<sup>3</sup>.

#### 2.1.4 Analytical calculations for gamma dose distribution

The analytical modeling for the total dose takes into account the inverse square law and attenuation contributions. Volume integrals to determine the total dose were solved using Mathematica software. The photon fluence differential  $d\phi$  at a given point  $a$  outside the tumor, due to a volume differential  $dV$  is given by:

$$d\phi = \frac{\gamma_y A_V e^{-\mu/\rho |\mathbf{r}-\mathbf{r}'|} \rho}{4\pi(|\mathbf{r}-\mathbf{r}'|)^2} dV \quad \text{Eq. 2.1}$$

where  $\gamma_y$  is the gamma yield,  $A_V$  is the volume density of activity (total activity/volume),  $\mu/\rho$  the mass attenuation coefficient for a given photon energy,  $\mathbf{r}'$  is the vector representing the position of the fluence differential shown in Figure 2.3,  $\mathbf{r}$  is the vector representing the position  $a$  outside the tumor,  $|\mathbf{r}-\mathbf{r}'|$  the distance between the source differential and the point of interest  $a$ , and  $\rho$  is the medium density.

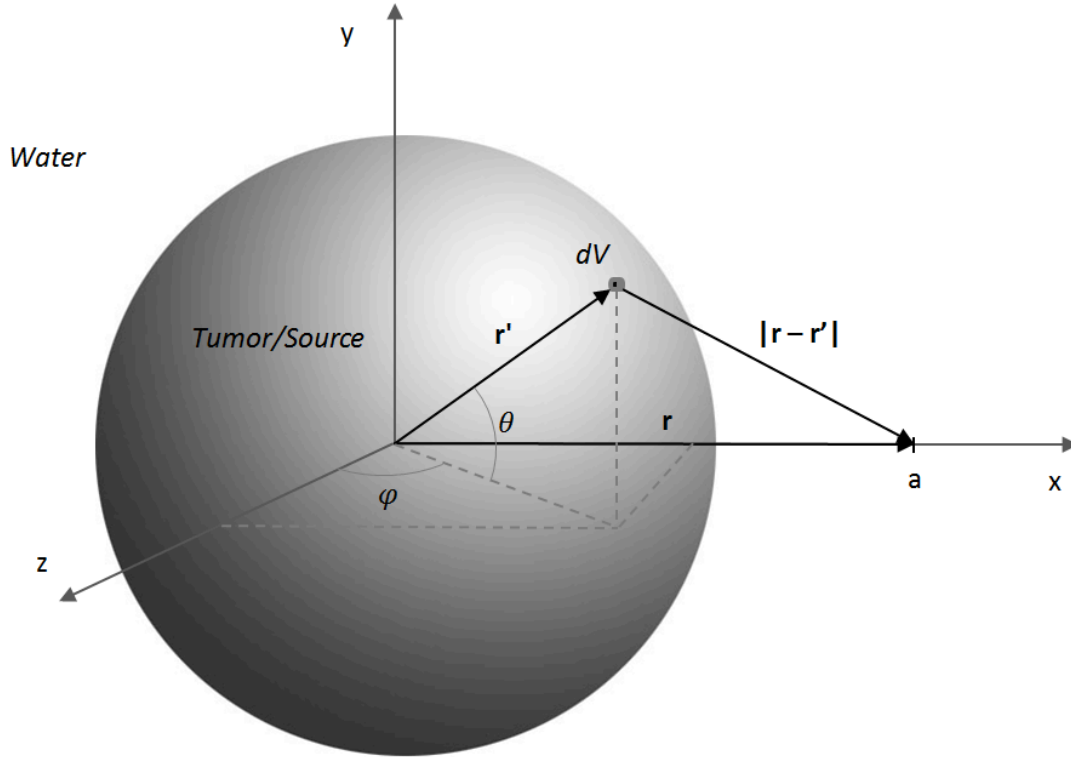


**Figure 2.3** Geometry used for analytical calculations. Tumor is filled with activated  $^{142}\text{Pr}$  microspheres and immersed into the water.

The dose rate differential at the point of interest  $a$  is given by:

$$d\dot{D} = E d\phi \frac{\mu_{en}}{\rho} \quad \text{Eq. 2.2}$$

where  $E$  is the photon energy,  $d\phi$  is defined in Equation 2.1 and  $\mu_{en}/\rho$  is the mass energy absorption for a given photon energy. The total dose rate  $\dot{D}$  at the point of interest  $a$  can be calculated by integrating the dose rate due to each fluence contribution over the entire spherical volume. In spherical coordinates it becomes:

$$\dot{D} = \iiint E \frac{\mu_{en}}{\rho} \frac{\gamma_y A_V e^{-\mu/\rho |\mathbf{r}-\mathbf{r}'| \rho}}{4\pi(|\mathbf{r}-\mathbf{r}'|)^2} r^2 \sin\theta \, dr \, d\theta \, d\varphi \quad \text{Eq. 2.3}$$

With  $r$  varying from 0 to  $R$ ,  $\theta$  from 0 to  $\pi$ , and  $\varphi$  from 0 to  $2\pi$ . The dose was calculated for different values of  $a$  along the x axes. For instance, for a 1 cm radius tumor the dose rate was calculated for  $x$  values ranging from 0 to 10 cm. Total activity was 10.1 GBq for  $^{142}\text{Pr}$  calculations, based on the typical vial activity used for  $^{90}\text{Y}$  treatments. The energy absorption and mass attenuation coefficients used for tumor and medium were those of water for a 1.58 MeV gamma photon. Comparison between the time to deliver 90% of the prescribed dose was performed for  $^{90}\text{Y}$  and  $^{142}\text{Pr}$ . Results were compared with values obtained from the simulation.

## 2.2 CONFORMAL EYE BRACHYTHERAPY DEVICE

### 2.2.1 Device development

The development and design of a conformal eye brachytherapy (CEBT) device for an individualized treatment of OSCC using  $^{142}\text{Pr}$  is proposed and studied. This study is divided into two main steps. The first step identifies (i) the rationale for and importance of a new eye applicator, and (ii) the device design and how it compares to the currently available eye plaques. The second part consists of the preliminary studies on the viability of a new eye applicator, which consists of: (i) the evaluation of several possible radionuclides (ii) MCNPX2.6 Monte Carlo simulations for the proposed geometry and radionuclide comparison, and (iii) experimental validation of the Monte Carlo method for a simplified case. Future work includes patent application, device assembly, development of a treatment planning system capable of calculating the necessary fields in order to optimize the tumor coverage, and proposing quality assurance (QA) methods to verify the treatment planning and dose delivered.

#### *Choice of radionuclide*

In previous work the use of beta emitters  $^{90}\text{Y}$  and Rhenium-188 ( $^{188}\text{Re}$ ) has been reported for eye brachytherapy. Based on its physical and radiobiological properties, as well as its availability and activation costs,  $^{142}\text{Pr}$  was chosen as a suitable radionuclide for this study. However, the device design is not limited to this radionuclide and other beta emitters could be used as well. Monte Carlo simulations were performed to determine the beta and gamma dose distributions for  $^{142}\text{Pr}$  within the eye. Simulation of dose distributions for  $^{90}\text{Y}$  and  $^{188}\text{Re}$  were performed as well and compared with the distribution for  $^{142}\text{Pr}$ .

### 2.2.2 CEBT design

An average adult human eye has an axial length along the visual axis of 24 mm, horizontal and vertical diameters of 23 and 23.5 mm and a mass of 7.5 g. The proposed device is able to cover up to 3 cm diameter of a spherical surface. The device consists of  $^{142}\text{Pr}$  glass rods arranged in a 3.00 cm diameter grid, capable of covering most scleral tumor sizes. Individual rods can be controlled independently. Figure 2.4 shows the device and ten selected rods projected outside of the beta shield.

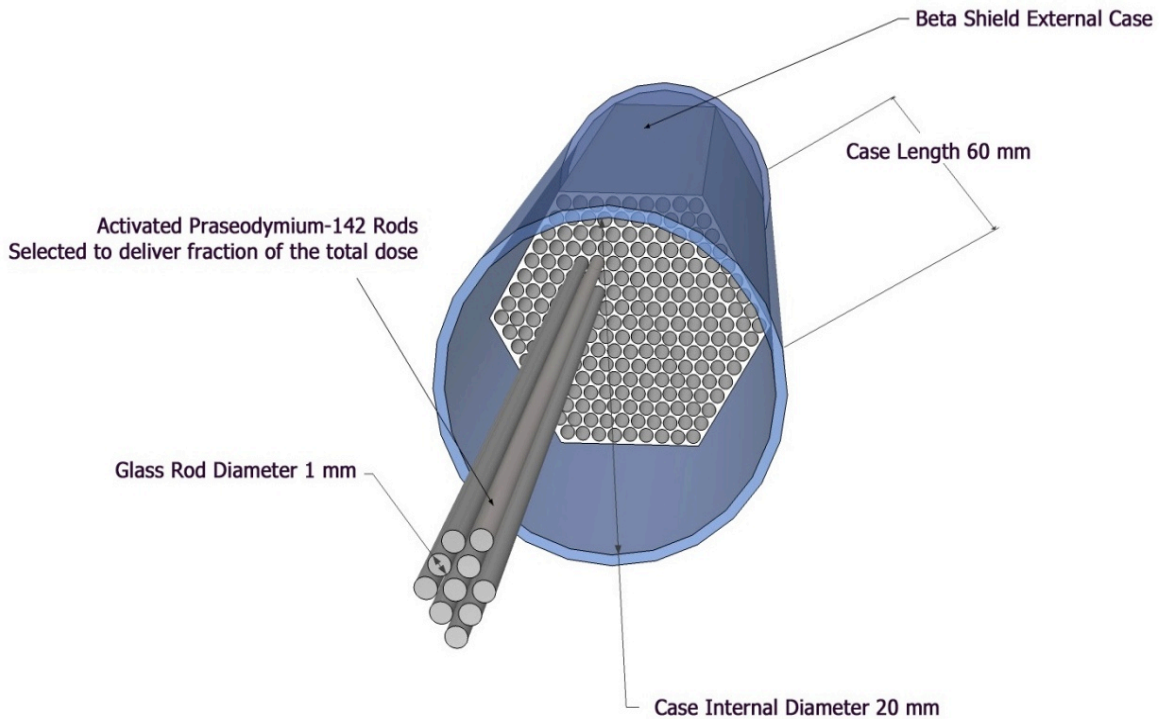


**Figure 2.4** Eye applicator design.

The device was drawn using the 3D Computer aided design software, SketchUp Version 8. A digital control system, connected to a computer interface, would allow the execution of the treatment plan. The rods are placed parallel to each other within a hexagonal template. The

motion of each rod is independent, allowing the positioning of any combination of rods on the eye surface. The length of the rod projection can be also controlled in order to better conform to the spherical shape of eye surface. The surrounding external case and template are made of a beta shielding material, e.g. Plexiglas. The device holder was designed to rotate and translate to allow better positioning of the eye device on the patient eye surface (Figure 2.5).

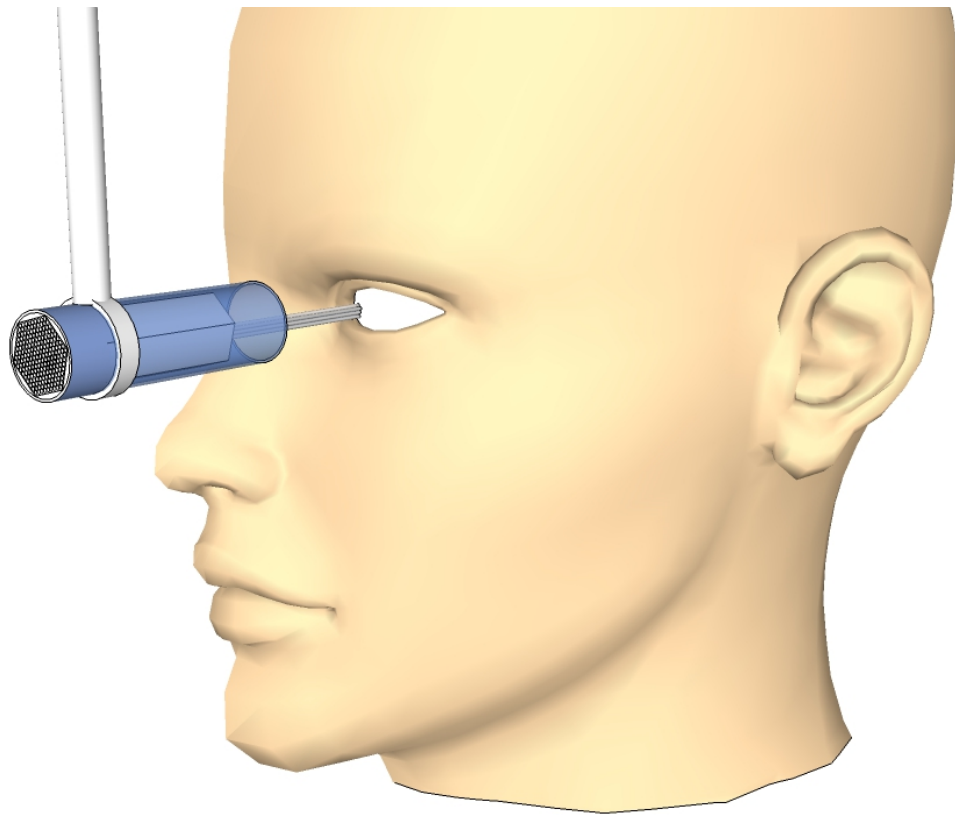


**Figure 2.5** Eye applicator holder

The patient head and eye may be immobilized prior to the treatment, to allow a precise delivery of the total planned dose. Four different “segments”, formed by configurations of glass rods, and the resultant “field” is shown in Figure 2.6, with the rods used for each field highlighted. The freedom of independently positioning the rods would allow a more conformal

dose to be delivered to the tumor. Computer programmed rod placement would allow a set of rod configurations to deliver the planned dose.  $^{142}\text{Pr}$  can be activated immediately before use in a research reactor such as TRIGA. This device can also be reactivated several times and therefore, eye applicators using this nuclide could be reused upon nuclide reactivation.

### *Materials selected for the device's prototype*

A prototype of the eye device was developed in the East Carolina University Physics Department machine shop, and is in the initial execution phase. The materials selected for the core of the CEBT in this first model was Self Lubricating Oil-Filled UHMW (Ultra High Molecular Weight) Polyethylene, with 1-1/4" Diameter, and 1' length from McMaster-Carr Supply Company. This material was chosen for its desirable physical properties. For the movable rods High Temperature Garolite (G-11), 1/16" Diameter, and 1' Length was chosen.

### **2.2.3 Monte Carlo Simulation for CEBT device**

A glass rod was simulated (Figure 2.7) to determine the dose distribution within the eyeball for the use in episcleral brachytherapy using MCNPX2.6 Monte Carlo code (input codes can be found in Appendix A.2.1 and A.2.2). Dose due to one rod can be used to derive the dose due to an arrangement of rods by the superposition principle. A total physical dose of 85 Gy was used as reference dose in the treated tumor volume, based on the American Brachytherapy Society (ABS) recommendations for brachytherapy of uveal melanomas (Nag et al., 2003).

## 2.2.4 MCNPX2.6 Monte Carlo Simulations for $^{142}\text{Pr}$ , $^{90}\text{Y}$ , and $^{188}\text{Re}$

In order to compare  $^{142}\text{Pr}$ ,  $^{90}\text{Y}$  and  $^{188}\text{Re}$  as possible choices for use in eye brachytherapy, Monte Carlo simulations were performed for each nuclide to determine the dose distributions within the eyeball (input code can be found in Appendix A.2.3). A model for the glass eye plaque applicator was designed for episcleral brachytherapy, with rectangular geometry of  $1.00 \times 1.00 \text{ cm}^2$  area and curved interior (Figure 2.8). The eye applicator was designed to contour to the eye and to be in contact with the eye surface during the treatment. This geometry, contrary to the model proposed for the CEBT, delivers a more homogeneous dose to the eye surface. However the goal in these simulations was to compare the effect in the eye doses when different nuclides are used, and therefore a simpler geometric model was adopted.

A total physical dose of 85 Gy was used as reference dose in the treated tumor volume, based on the American Brachytherapy Society (ABS) recommendations for brachytherapy of uveal melanomas. From the nuclides studied,  $^{188}\text{Re}$  had the highest parent isotope cross-section (73 b), followed by  $^{142}\text{Pr}$  (11.4 b) and then  $^{90}\text{Y}$  (1.28 b). The half-life of  $^{188}\text{Re}$  was the shortest (17.0 h), compared to  $^{90}\text{Y}$  (64.0 h) and  $^{142}\text{Pr}$  (19.12 h).

A last model for the eye rod MCNPX2.6 Monte Carlo Simulations (input code can be found in Appendix A.2.4) was developed simulating the experimental measurements conducted with  $^{142}\text{Pr}$  glass rods in water phantom. A squared water phantom (red) was used to simulate the measurements conditions (Figure 2.9). The 1.5 mm diameter eye rod (blue) was placed on top of the water phantom. Both  $^{142}\text{Pr}$  glass rod and water phantom were surrounded by air (green). A mesh tally containing  $60 \times 60 \times 60$  voxels was created and the dose profile was analyzed in the xy-axis and zy-axis, in a squared volume of  $1.0 \text{ cm}^3$ .

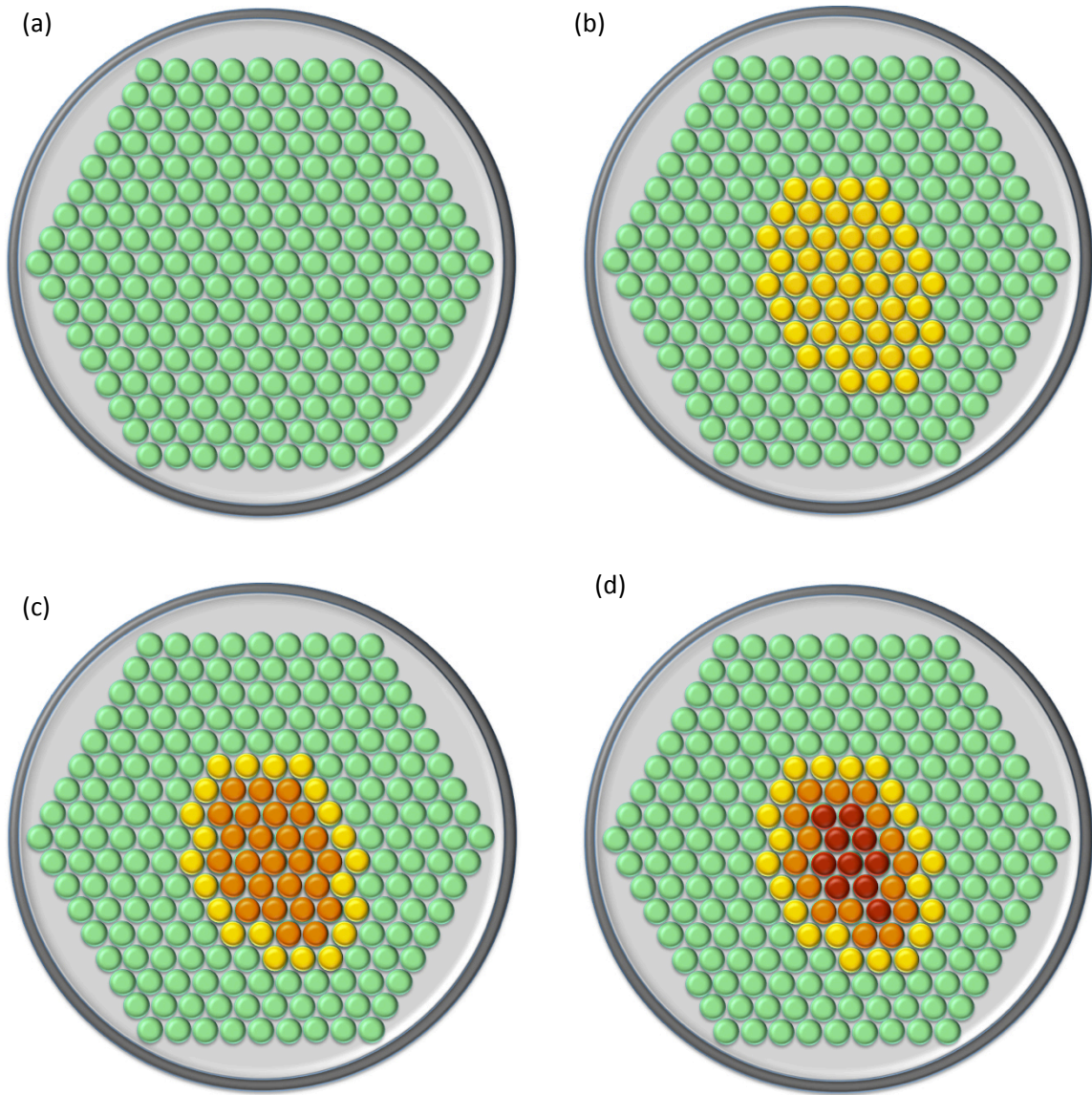


**Figure 2.6** Top view of the eye applicator: rods are allowed to move independently in order to conform the particular target geometry being treated and to deliver the planned dose. In this figure we can see different segments added together (a) no rods (all green), (b) one (yellow), (c) two (yellow + orange), (d) and three (yellow + orange + red) segments added to form a field.

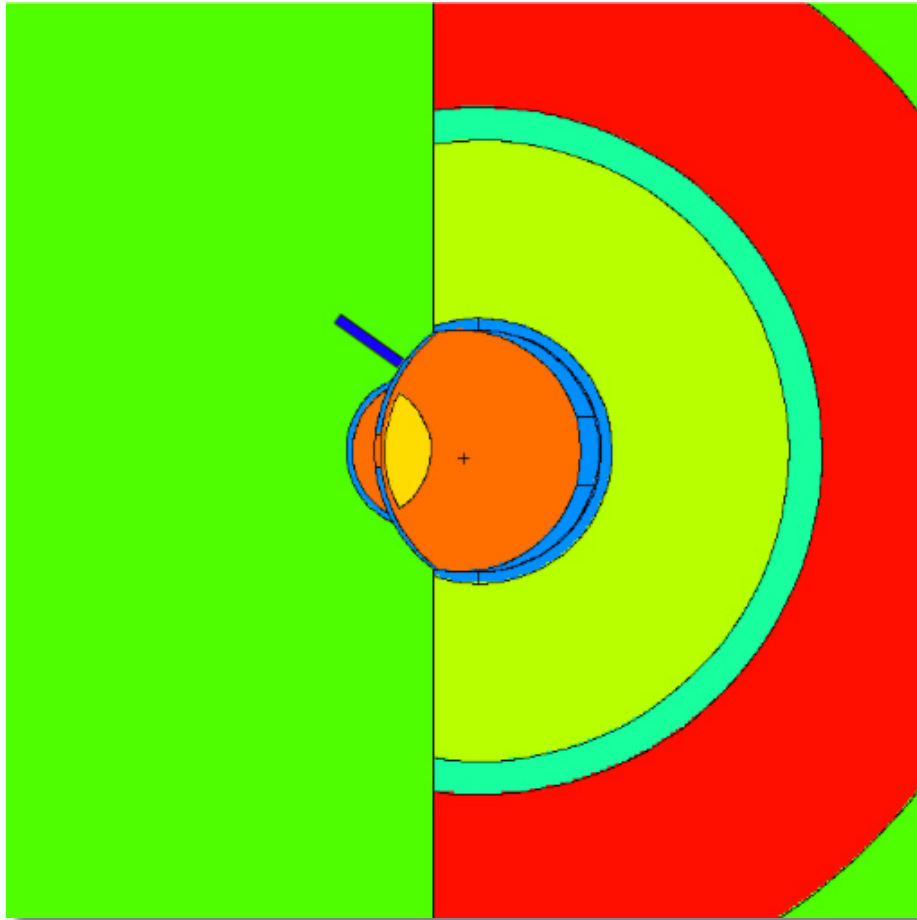


**Figure 2.7** Eye model and one  $^{142}\text{Pr}$  rod touching the eye surface (sclera). A total dose of 85 Gy was used as a reference in the treated tumor volume, according to the ABS recommendations for brachytherapy of uveal melanomas (Nag et al. 2003). Credits for the model for detailed anatomy of the eye in MCNPX2.6: Choonsik Lee, PhD, National Cancer Institute.

999

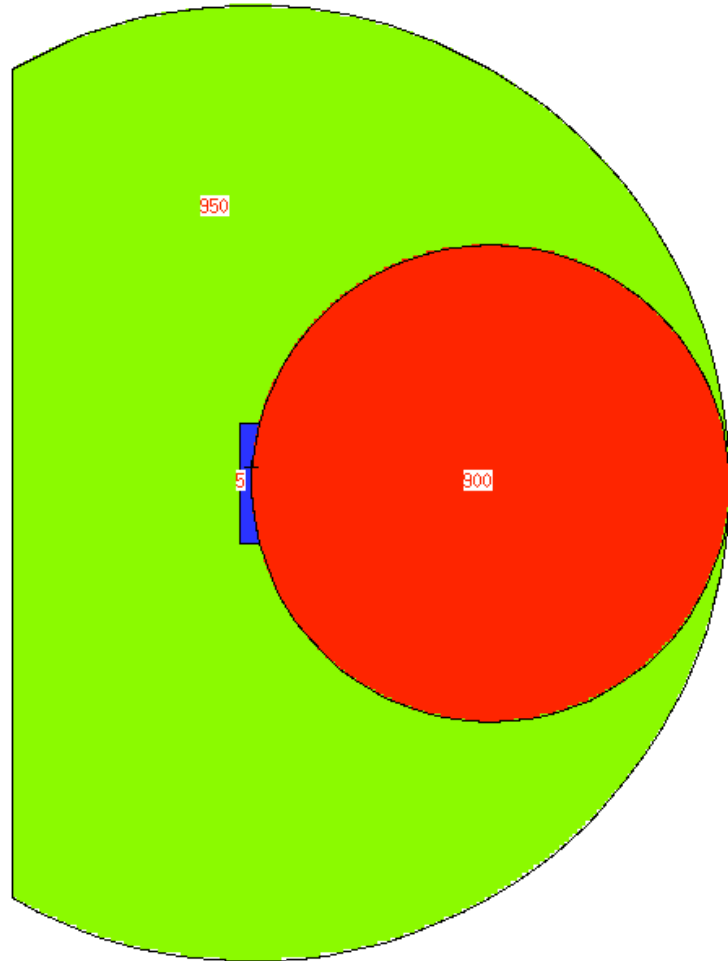


**Figure 2.8** Sagittal view of the geometry input used in the MCNPX2.6 to simulate the dose distribution due to  $^{142}\text{Pr}$ ,  $^{90}\text{Y}$  and  $^{188}\text{Re}$  within the eyeball. Eye plaque (blue), the eyeball (red) the eyeball surroundings (green) and the air outside the body (white).

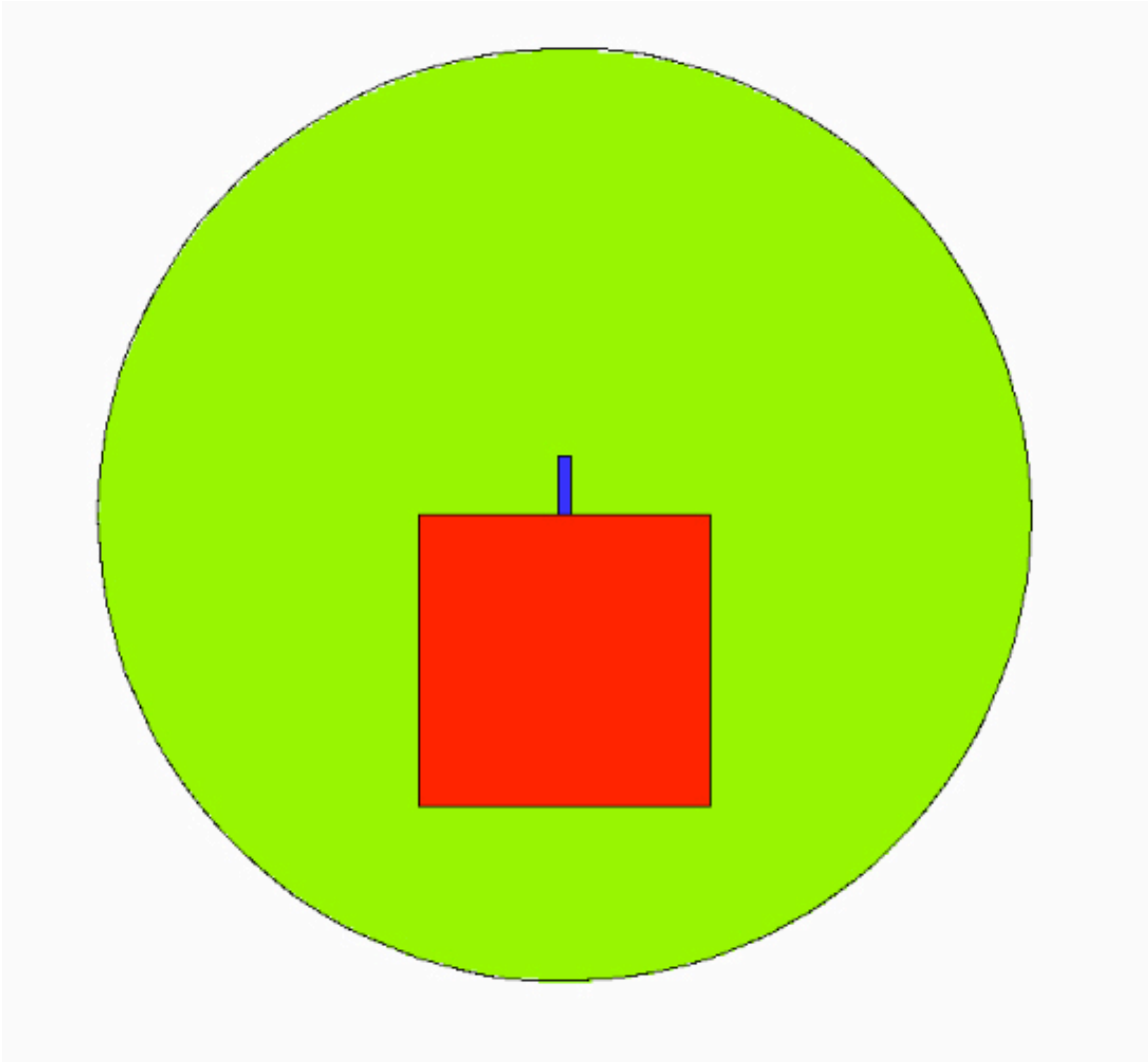


**Figure 2.9** Geometry input used in the MCNPX2.6 to simulate the dose distribution due to  $^{142}\text{Pr}$  experiments with glass rods. The squared water box (red) had dimensions  $2.5 \times 2.5 \times 2.5 \text{ cm}^3$ , the rod (blue) had the same dimension of the experimental glass rod, 1.5 mm diameter and 5 mm length. Dose profiles were acquired on the plan perpendicular to the base of the rod and on the z-axis, parallel to the rod's symmetry axis.

## CHAPTER 3: MATERIALS AND METHODS II: EXPERIMENTAL DESIGN

### 3.1 Microsphere Brachytherapy and Eye Brachytherapy

In this chapter the experimental techniques to measure the dose fall-off due to the  $^{142}\text{Pr}$  glass microspheres and  $^{142}\text{Pr}$  glass rods are described. Dose distributions in custom designed solid water phantoms were measured using GAFCHROMIC<sup>®</sup> EBT2 film. Details of the phantom design and film calibration, as well as safety measures involved in these measurements are described in this chapter.

### 3.2 Nuclide Activation

#### *$^{142}\text{Pr}$ Microspheres Activation*

The 0.169 g sample of  $^{141}\text{Pr}$  microspheres was irradiated and the calculated activity at the time of receiving the source was 36.6 mCi. The measurements were performed on the same day the microspheres were received. For a clinical vial activity of 7,500 Bq per  $^{142}\text{Pr}$  microsphere, containing a total of  $1.2 \times 10^6$  microspheres, the vial activity would contain 9 GBq or 2.43 Ci. The final activity of the sample was scaled down from the necessary clinical activity so that the radiation exposure to the staff and general public could be minimized. The reactor used for irradiating the samples was the Missouri University Research Reactor (MURR<sup>®</sup>) with a neutron flux  $\phi$  of  $9.60 \times 10^{13}$  thermal  $\text{n}(\text{cm}^2\text{s})^{-1}$ . The total irradiation time was 0.40 h (24 min), and the time from the irradiation time until sample delivery was approximately 33 hours. Samples were shipped to the Radiation Safety Officer and transported to the East Carolina University main

campus. The experimental setup and measurements were performed in the Health and Medical Physics Lab facilities at the Howell Science Complex, East Carolina University.

The percentage of  $^{141}\text{Pr}$  in the microspheres used was 46.14 %. Therefore, the number of atoms  $N$ , contained in 0.169 g of  $^{141}\text{Pr}$  calculated using Eq. 1.16 (reduced to 44.4%) was  $3.20 \times 10^{20}$ , with  $m$  equal to 0.169 g and  $M$  equals to 141 g/mol. The saturation activity of this sample calculated using Eq. 1.15 was  $3.57 \times 10^{11}$  Bq (9.64 Ci), with  $\phi$  equals to  $9.60 \times 10^{13}$  thermal  $\text{n}(\text{cm}^2\text{s})^{-1}$ ,  $\sigma$  equals to  $11.6 \times 10^{-24}$   $\text{cm}^2$ , and  $N$  equals to  $3.20 \times 10^{20}$ . Therefore, the activity (Ci) as a function of the time for the 0.169 g of  $^{141}\text{Pr}$  microspheres sample is:

$$A(t) = 9.64 (1 - e^{-(0.0361)t}) \quad \text{Eq. 3.1}$$

where  $t$  is the irradiation time in hours and  $0.0361$  ( $\text{h}^{-1}$ ) is the calculated decay constant for  $^{142}\text{Pr}$ . To obtain the irradiation time (h) as a function of the desired activity of this sample, this equation can be rewritten as:

$$t = 27.7 \ln \left( 1 - \frac{A}{9.64} \right)^{-1} \quad \text{Eq. 3.2}$$

To obtain 36.6 mCi at the delivery time the sample should be irradiated by 0.4 h (24 min).

### *<sup>142</sup>Pr Rods Activation*

Ten <sup>141</sup>Pr glass rods were activated in the same research reactor. The glass rods had diameter of 1.5 mm and a length of 5 mm, with a total sample mass of 0.353 g. They were composed of 44.5% of <sup>141</sup>Pr. Using the same calculation methods described for the microspheres sample, the received activity for each rod was calculated as 76.3 mCi.

### **3.3 Experimental Setup**

A phantom was designed and constructed to carry out the dose distribution measurements. Measuring dose of a single microsphere is challenging, due to its small size and limitation of the total dose delivered by a single sphere. Unlike other sealed sources used routinely in brachytherapy, the activity and dose due to a single microsphere cannot be individually verified. In fact, no standardized methods exist to this date to verify <sup>90</sup>Y microsphere vials activities (Dezarn and Kennedy, 2007; Dezarn et al., 2011). Therefore, the measurements with microspheres were performed in bulk solution distributed in a known geometry. A micro glass capillary was used to hold the microspheres. Having a known geometry made possible to validate the Monte Carlo simulations with the experiments. The detailed experimental setup and procedures to perform these measurements will be discussed in the following sections.

#### **3.3.1 Film Calibration**

The change in optical density of the irradiated GAFCHROMIC<sup>®</sup> EBT2 calibrated film was used in this work to access the dose fall-off of due the <sup>142</sup>Pr microspheres and to the <sup>142</sup>Pr glass rods. For the film calibration, known doses of electron external beam calibrated by the

TG51 protocol were used to irradiate the film. An Exradin Farmer-type chamber Model A12 was used for the output check. This ion chamber is specifically designed for absolute dosimetry calibrations in water, air, or other phantom material and it is completely characterized in TG 51 (Almond et al., 1999). A 6 MeV electron beam (Siemens ONCOR™ Linear Accelerator, Leo Jenkins Cancer Center) was used to calibrate the GAFCHROMIC® EBT2 film. The beam output was measured at 1 cm depth in solid water, with 100 cm source to surface distance (SSD), collimated with a  $15 \times 15 \text{ cm}^2$  cone, which corresponds to the machine calibration point. The raw reading was corrected for the temperature and pressure and then compared with the calibration value. The temperature and pressure correction factor is given by:

$$P_{TP} = \frac{273.2 + T}{273.2 + 22.0} \times \frac{760}{P} \quad \text{Eq. 3.3}$$

Where  $T$  is the temperature in degrees Celsius and  $P$  is the pressure in mmHg. For the temperature measurement, a thermometer was placed inside the solid water phantom and stayed for a few minutes until reaching thermic equilibrium. Temperature and pressure values of 22.4 °C and 769 mmHg were measured, and a value of 0.990 was calculated for  $P_{TP}$ . The calibrated reading for the 6 MeV electron beam obtained from the annual quality assurance was  $20.86 \times 10^{-9} \text{ C}$ . The corrected reading using a NIST calibrated Exradin A16 ion chamber was  $20.78 \times 10^{-9} \text{ C}$ , or 0.383% lower than the calibrated value. Therefore the dose per monitor unit (MU) was corrected by 0.383%. A total of 11 stripes having  $2 \text{ cm} \times 3 \text{ cm}$  were exposed to doses ranging from 0 to 1020 cGy. One additional stripe of the film was left un-irradiated and used as a reference for the scanned output corrections. The number of MUs delivered to the film stripes

were: 0, 20, 40, 80, 160, 240, 320, 420, 520, 620, 820, 1020 MUs. Only one film stripe was irradiated at a time, in order to have them placed in the same position in relation to the field size. Each film was placed at the center of the field size, where the beam is more symmetric and flat. Films were placed at depth of  $d_{max}$  (1.3 cm). After temperature and corrections were applied, a 1.0038 cGy/MU was found for the beam output at  $d_{max}$ .

GAFCHROMIC<sup>®</sup> EBT2 film has an asymmetrical cross-section and also a directional dependence for portrait or landscape orientation. Therefore, each stripe of film was marked with a slit in the top right corner, following the original film sheet to guarantee that every individual stripe would be scanned in the same direction.

After 24 hours of the exposure, the color changes in the film were read using a flatbed Epson Perfection V750 Pro scanner (Leo Jenkins Cancer Center). Digital images of the film stripes were acquired according to the scanning guidelines suggested by the GAFCHROMIC<sup>®</sup> EBT2 manufacturer. Readings were done using a 48-bit color image type, with resolution of 300 dpi, and with all the image adjustment features turned off. Images were analyzed using the public domain software, ImageJ (Image processing and analysis in Java) developed at the National Institute of Health (NIH). The RGB channels were split (Figure 3.1) and each channel was converted to a 16-bit gray scale. Gray values ranged from 0 to 255, in which values closer to 0 correspond to more exposed areas. A histogram function was used to analyze the film gray scales.

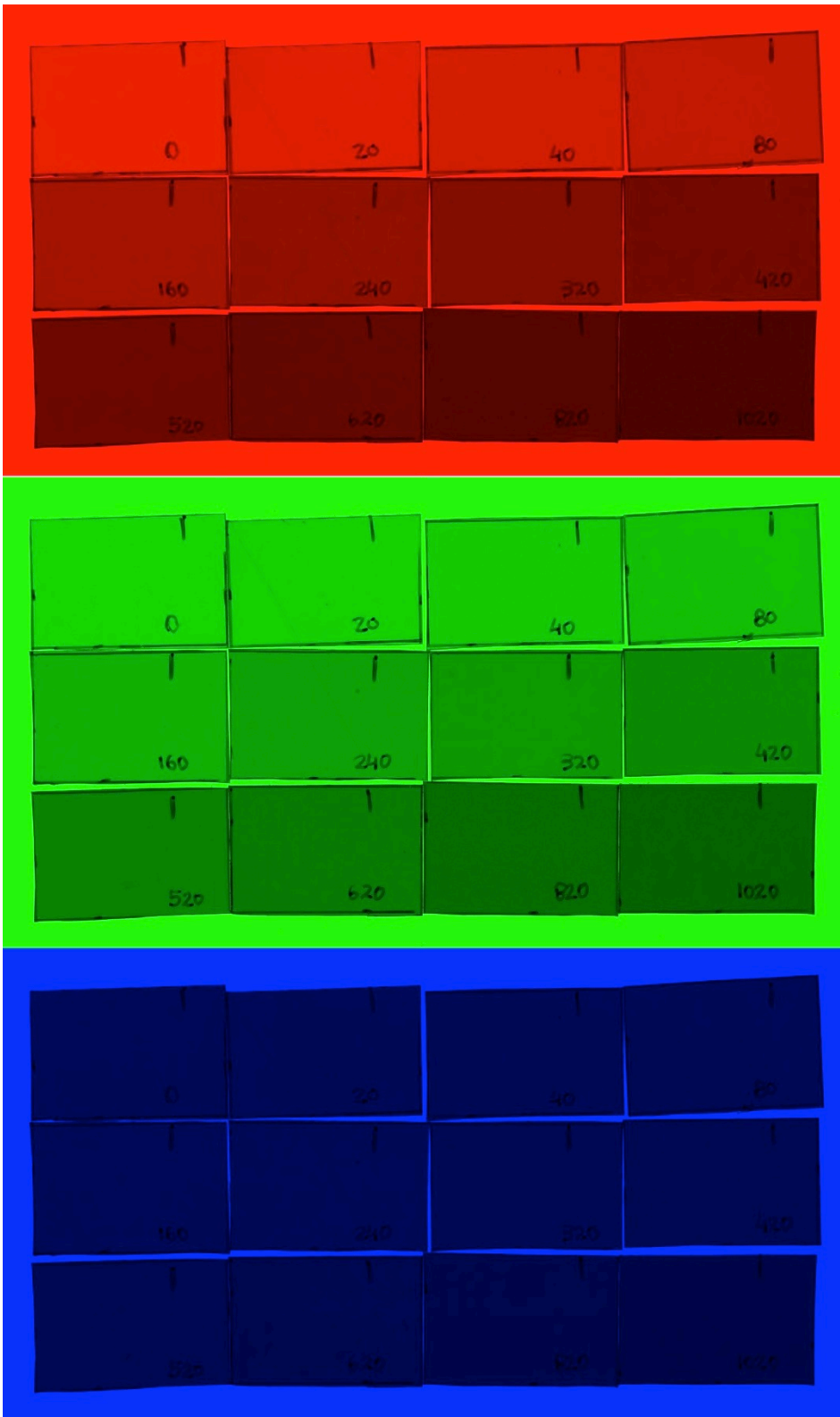


**Figure 3.1** Red Blue Green Channels and their different brightness responses to radiation doses.

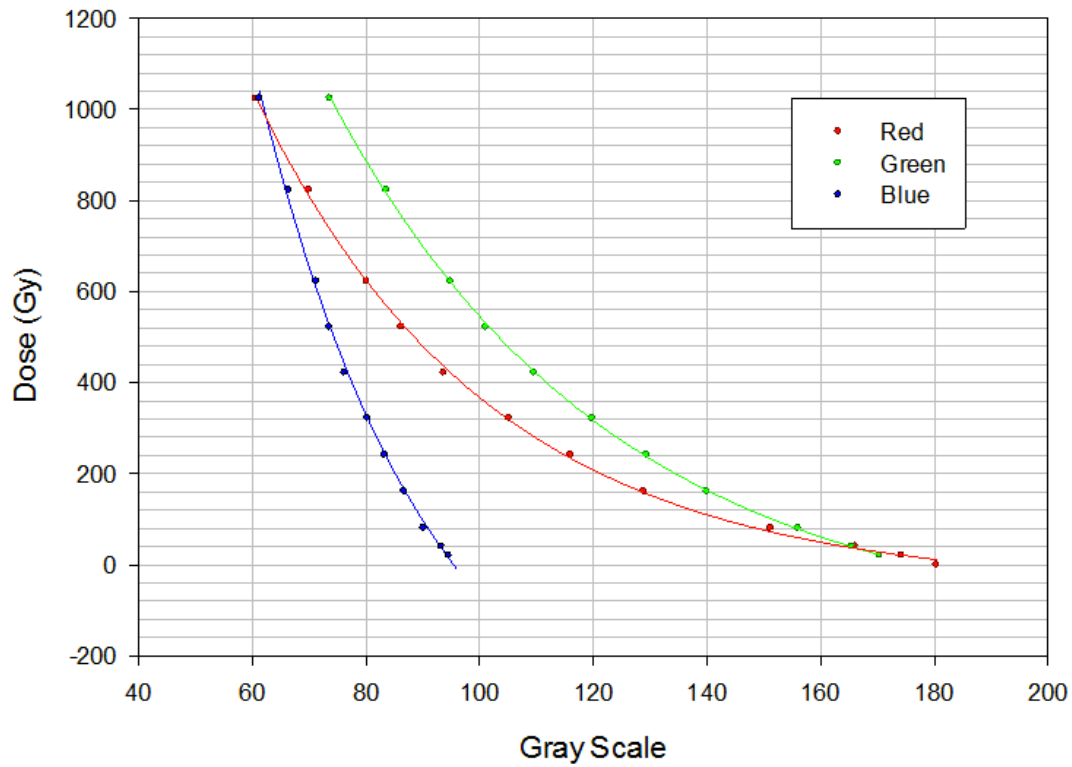


**Figure 3.2** Film calibration using a Siemens ONCOR 6 MeV electron beam: gray-scale plot of the RGB channels and fitted curves.

An average of 30,000 pixels was counted in each film stripe. Values for maximum, minimum, median and average gray scale values were acquired in ImageJ and plotted using SigmaPlot™ software (Figure 3.2). Standard deviations for gray scale values were within  $\pm 1\%$  and therefore were not included in the plot. A non-linear regression and dynamic fitting was performed using SigmaPlot™ software. A three-parameter exponential decay equation was used to fit the red channel gray scale plot:

$$f = y_0 + ae^{-bx} \quad \text{Eq. 3.4}$$

with parameters equal to:  $y_0 = -47.94 \pm 8.61$ ,  $a = 4661.1 \pm 158.3$ ,  $b = 0.0242 \pm 0.0006$ . A total of 200 iterations was performed a  $R^2 = 0.9994$  was obtained for this dynamic fitting.

### 3.3.2 Verification of Glass Microspheres

The  $^{141}\text{Pr}$  glass microspheres (Figure 3.3) were manufactured by MO-SCI Corporation (Rolla, MO). The composition of the glass microspheres is as follows: Si: 12.5%, Al: 9%, Pr: 46.14%, and O: 31.31%. The composition of the glass rods is very similar: Si: 15.3%, Al: 8.10%, Pr: 44.5%, and O: 32.1%. According to the manufacturer, microspheres sizes range from 20 to 35  $\mu\text{m}$ . The inactive microsphere sample was analyzed using an optical microscope (Nikon, TE2000-S) in order to estimate the average size of the microspheres in the sample. Several frames at different parts of the sample were taken.



**Figure 3.3** Inactivated Pr glass microspheres

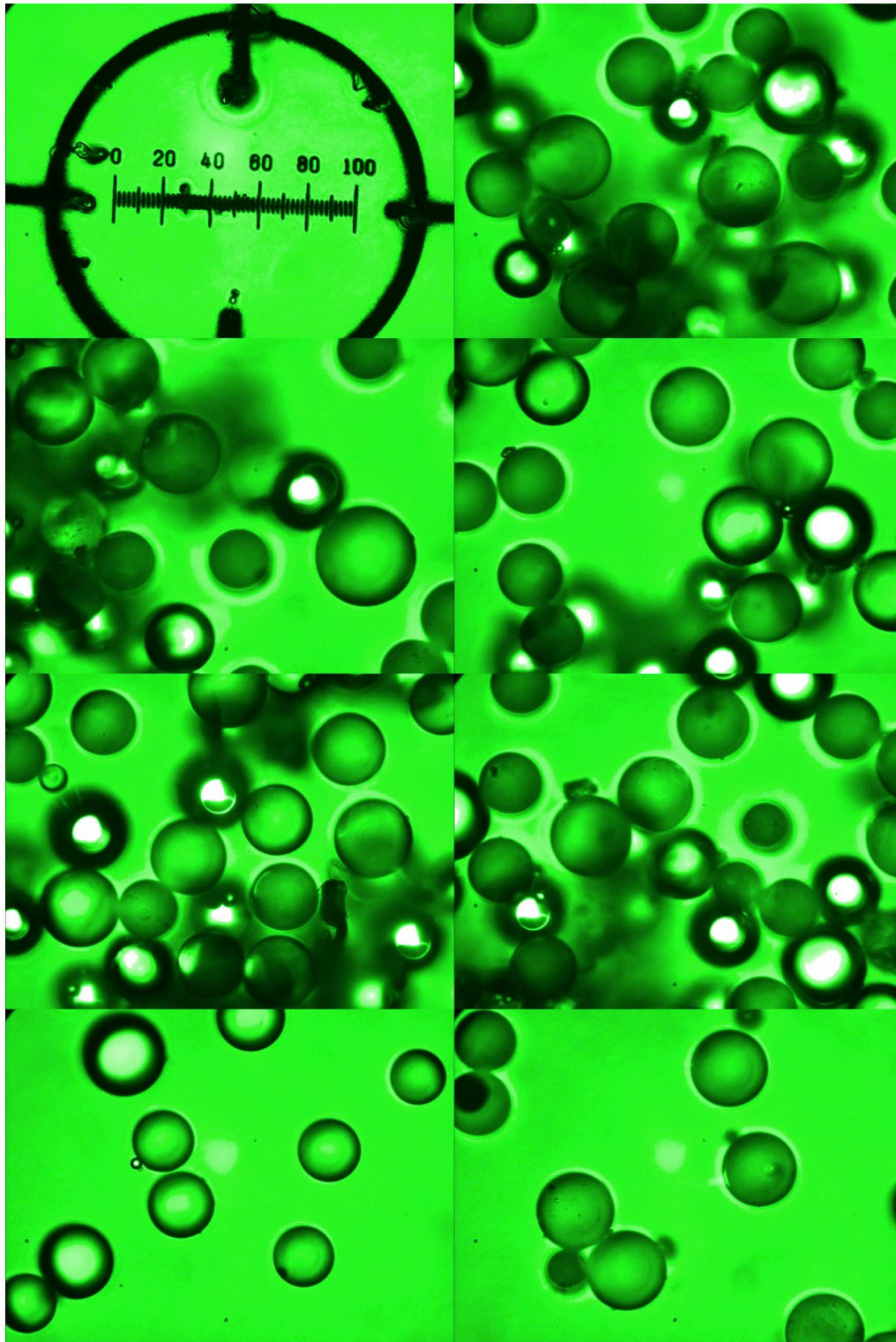


Figure 3.4 Microscopic view of the  $^{141}\text{Pr}$  microspheres

A total of 8 frames from different regions of the sample were analyzed (Figure 3.4). The first frame contains the microscope ruler with marks from 0 to 100  $\mu\text{m}$ , with resolution of 2  $\mu\text{m}$ , used for the pixel calibration. ImageJ software was used to determine the number of pixels corresponding to 100  $\mu\text{m}$  so that a conversion between number of pixels and actual size could be determined. It was found that at the imaging magnification, 751.41 pixels was equivalent to 100  $\mu\text{m}$ , or 0.1331  $\mu\text{m}/\text{px}$ . A total of 70 microspheres were measured. Only microspheres positioned at the same level as the focal distance of the microscope were taken into account, due to the optical artifact of a thicker and blurrier border for the microspheres out of focus. An average diameter of 29.7  $\mu\text{m}$  with standard deviation of 3.9  $\mu\text{m}$  was found for this sample.

### **3.3.3 Experimental setup for accessing dose fall-off of microspheres**

As discussed earlier, dose assessment of individual microspheres may be limited by their physical size and also by the small activity of a single microsphere. Arterioles have an approximated size of 37.0  $\mu\text{m}$ , and the end of capillary bed ranges from 8 to 10  $\mu\text{m}$ . Ideally, an experimental setup capable of representing an embolized blood vessel should have dimensions comparable to that of a blood vessel. However, due to experimental limitations of smaller sizes and lower doses measurements, handling and performing dosimetry for such small dimensions were unpractical. To overcome these limitations, a larger system was proposed to hold a bulk of microsphere solution.

A glass microcapillary (Drummond Scientific Company, Broomall, PA) was used to hold a dense microsphere solution (Figure 3.5). The microcapillary had inside diameter (ID) of 300  $\mu\text{m}$  and outside diameter (OD) of 450  $\mu\text{m}$ . The R-6 glass, as known as Soda Lime, had the

following chemical composition (weight percent): 74%: SiO<sub>2</sub>, 13%: Na<sub>2</sub>O, 10.5% CaO, 1.3% Al<sub>2</sub>O<sub>3</sub>, 0.3% K<sub>2</sub>O, 0.2%: SO<sub>3</sub>, 0.2%: MgO, 0.04%: Fe<sub>2</sub>O<sub>3</sub>, 0.01: TiO<sub>2</sub>.

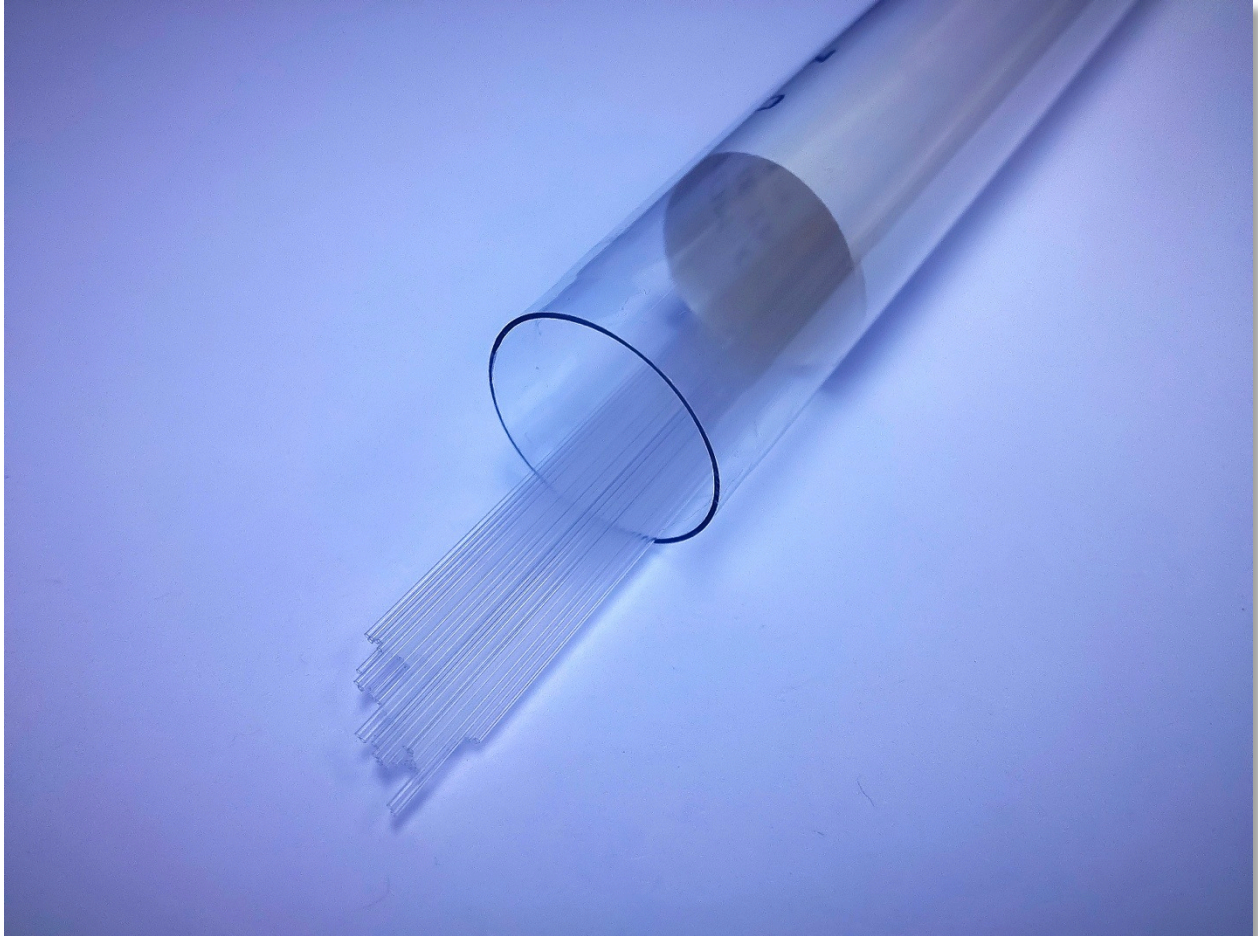


**Figure 3.5** Glass capillaries used as receptacle of microspheres.

The wall thickness of about 150  $\mu\text{m}$  was still thin enough to allow beta dose penetration and dose assessment by the film placed outside of the capillary. The microsphere solution was transferred to the capillary interior by using a micropipette developed for this purpose (Figure 3.6).

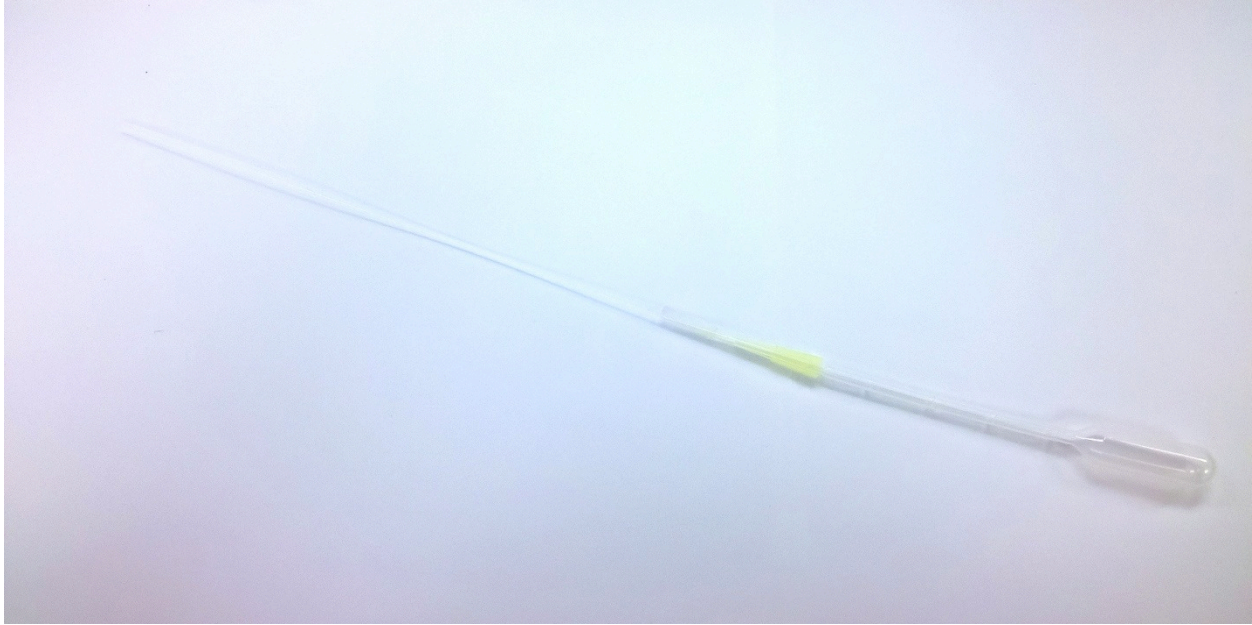


**Figure 3.6** Micropipette developed to fill the glass capillary with the microspheres. Microcapillary was attached to a disposable plastic 1 ml pipette through a micropipette (yellow part in the figure).

The solution was prepared by mixing 0.1 ml of sterile water (Cellgro<sup>®</sup>, Mediatec, Inc., Manassas, VA) to the activated microspheres. After filled with the microspheres solution, the capillary tips were sealed with super glue (Krazy Glue<sup>™</sup>). Based on the total volume inside the sample and concentration, a total of about 70,000 <sup>142</sup>Pr microspheres were inside the microcapillary. The final sample was analyzed under the microscope to access the pattern of microspheres distribution inside the micro capillary (Figure 3.7).

A new phantom was developed for this research to suit the requirements of the measurements (Figure 3.8). In order to attain full backscattering conditions for both primary and secondary photons and electrons the glass capillary was surrounded in by water and water equivalent plastic.

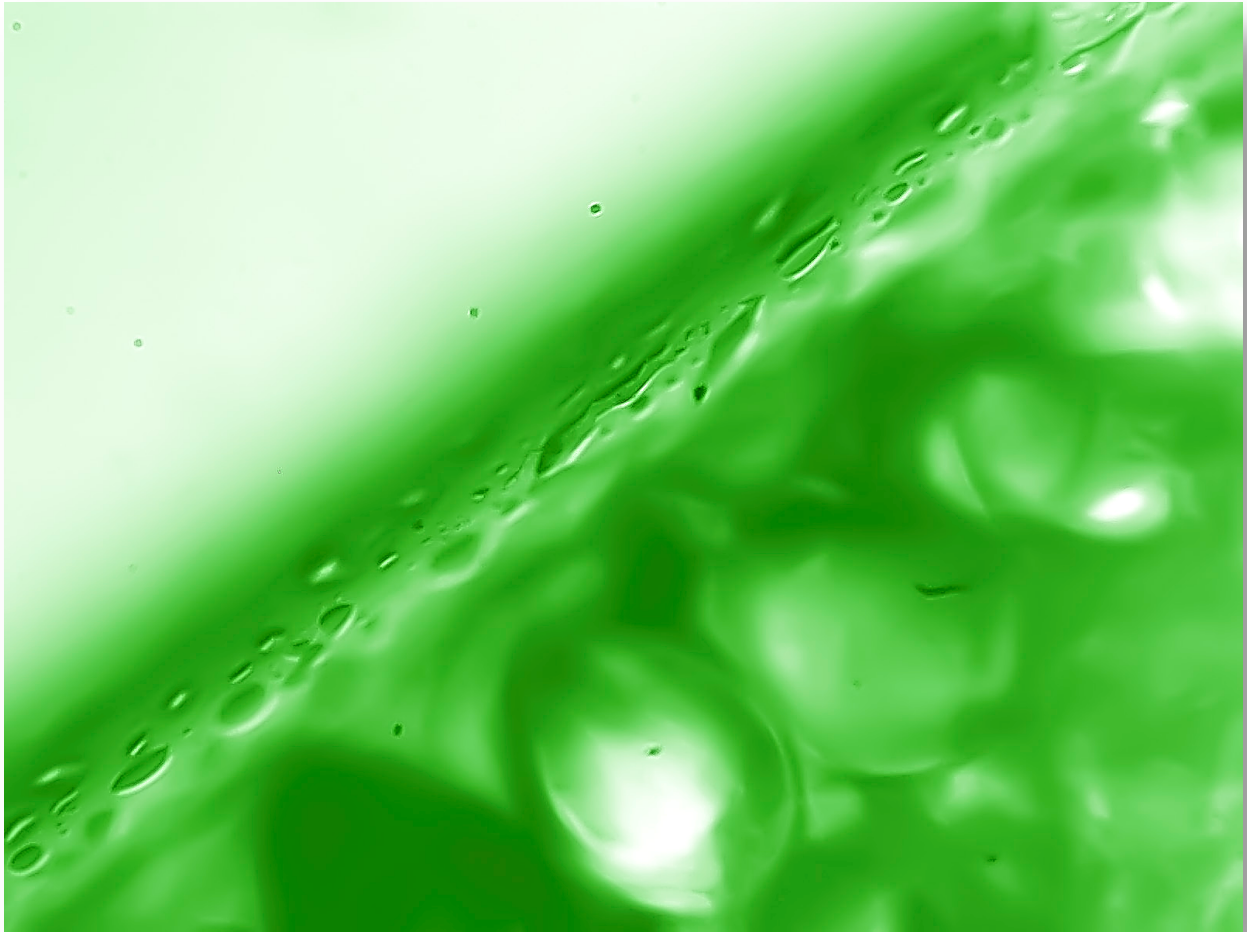


**Figure 3.7** Air-microcapillary-microsphere solution interface under the microscope.

Gammex Solid Water<sup>®</sup> was chosen as base material for this phantom. Solid Water<sup>®</sup> is a tissue equivalent material, and therefore, it has been used extensively for dosimetric purposes in medical physics, especially in IMRT dose assessment. One Solid Water phantom of 12 × 12 squared inches and widths of 5 cm formed the base of the phantom. Two square frames of Acrylonitrile butadiene styrene (ABS) with 1/2 inch each were cut and joined together on top of the film and placed on the phantom.

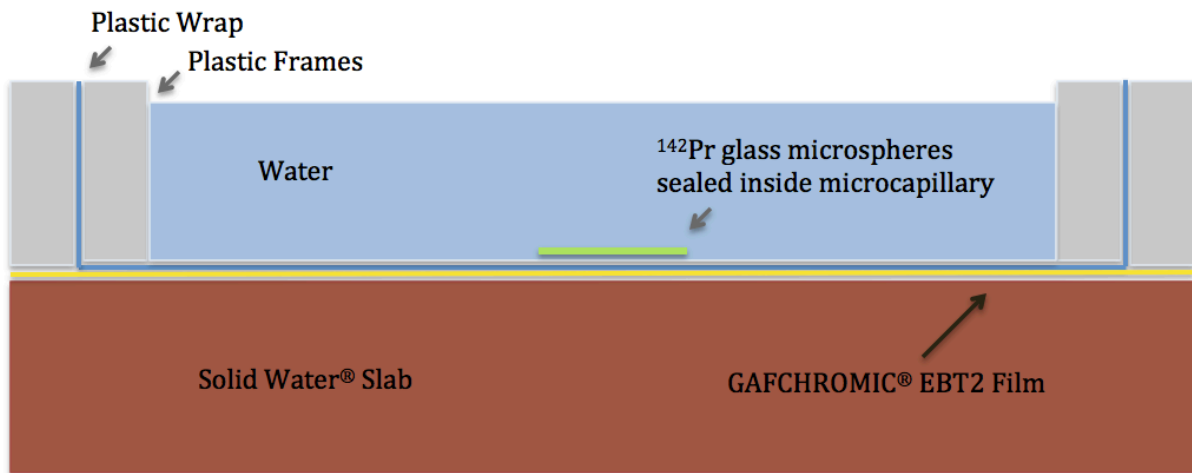


**Figure 3.8** Phantom developed to carry the measurements with the microspheres. A GAFCHROMIC® EBT2 film sheet (yellow line) was placed on top of a Gammex Solid Water® plastic slab. An external ABS plastic frame was placed on top of the Solid Water® phantom to support the liquid water. A plastic wrap (blue line) was used to protect the film from the water. Another internal ABS frame was used to hold the plastic wrap extended on top of the film. The internal frame was filled with water and the capillary containing the  $^{142}\text{Pr}$  microspheres was placed in the water.

The ABS top frames were used to hold a plastic wrap placed against the film surface on the edges of the solid water phantom and did not have any influence on the radiation interactions. Although ABS was not used as a phantom itself in this work (because of the lack of published data on its electron stopping power), ABS has been used for IMRT QA. ABS is a plastic-based low cost tissue equivalent material, and it has been proven to have similar attenuation coefficient to that of the solid water for different photon energies (Rajesh et al., 2010). ABS is also impact

resistant and presents high toughness, while being easily machinable. It can be designed to hold several types of detectors, including ion chambers, radiochromic film, gel dosimeters, diodes, and TLDs.

The film stayed in place for 51 hours (2.66 half-lives of the nuclide). The activity of the vial was measured using a NaI detector (NAIS-2x2 detector with Osprey™ digital tube, CANBERRA Industries, Inc.). Based on the sample total mass of 0.169 g, the glass density of  $4.0 \text{ g/cm}^3$  and the measured average microspheres diameter sizes of  $29.7 \text{ }\mu\text{m}$ , volume of  $1.38 \times 10^{-8} \text{ cm}^3$ , mass of  $5.49 \times 10^{-8}$  it was estimated a total of  $3.08 \times 10^6$  microspheres in the sample. A standard  $^{90}\text{Y}$  glass microspheres sample (Therasphere®) supplied in a 0.6 ml of sterile, pyrogen-free water usually contains from 22,000 to 73,000 microspheres. In this experiment 1.0 ml of distilled water was used to prepare the solution of microspheres. A final concentration of  $3.08 \times 10^6$  per ml was obtained. The remaining microsphere solution was deposited in a second water phantom, at spaced distances from one drop to the other. Once the microspheres reached the water phantom they formed random clusters that allowed measuring the dose distribution of microspheres distributed in different concentrations.



**Figure 3.9**  $^{142}\text{Pr}$  glass rods and DREMEL tool with diamond cut-off wheels (DW10M, SE<sup>®</sup>) was used to cut the rod into 5 mm length rods. Rod tips were smoothed until flat.

### 3.3.4 Glass Rods Measurements

The glass rod was cut into sections using a DREMEL<sup>®</sup> tool with diamond cut-off wheel (Fig. 3.9). For the glass rods dose assessment, one sheet of GAFCHROMIC<sup>®</sup> EBT2 film was sandwiched between two slabs of Solid Water<sup>®</sup>, and the rod was placed on top of the junction of the two slabs perpendicular to the surface (Figure 3.10).

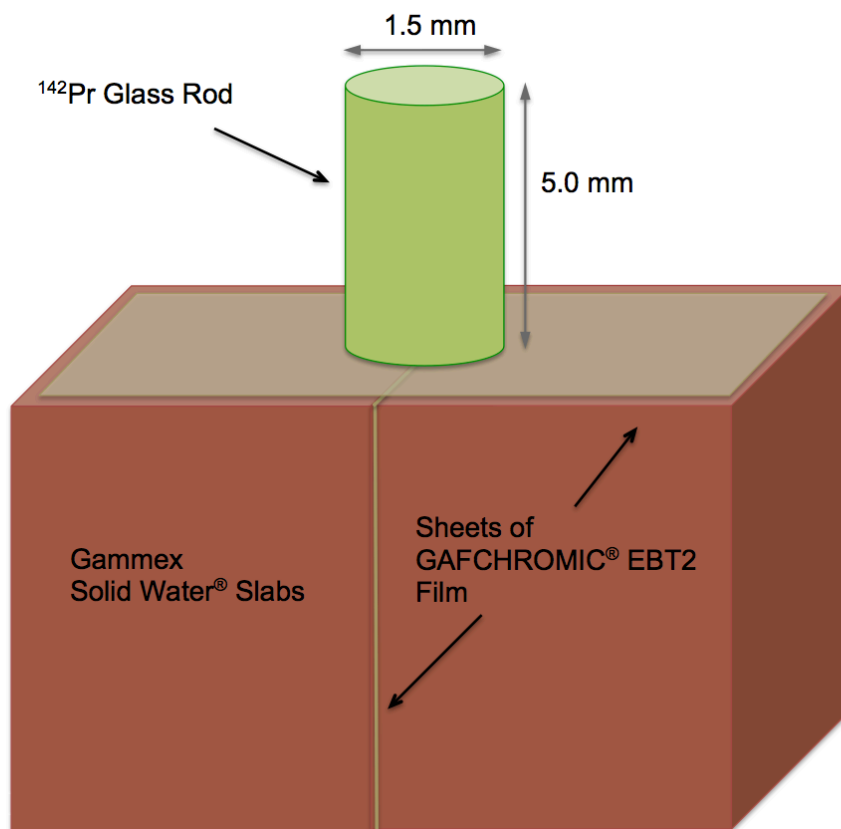


**Figure 3.10** View of the glass rods placed on top of the junction of the Gammex Solid Water<sup>®</sup> slabs. EBT2 film was placed between the slabs and on top of the phantom to measure and the axial dose profile.

To access the dose perpendicular to the axis, a glass rod was placed on top of a GAFCHROMIC<sup>®</sup> EBT2 film. The objective was to experimentally access dose distributions within the phantom and on the phantom surface due to a single rod in air and to compare it with the MCNPX2.6 simulations of dose distributions within the eyeball. The dose distribution was then measured along the axis parallel to the glass rod in the region within the plastic phantom. The irradiation time for the glass rod was the same used for the <sup>142</sup>Pr solution (2.65 days). In both measurement, a small paper funnel guide was used to efficiently placing rods in this positions, while decreasing exposure time during measurements.

### **3.4 Radiation Safety and Shielding of the Experimental Design**

The safety was considered a priority in performing these experiments. The radiation doses were kept as low as reasonably achievable (ALARA) with the help of the East Carolina University Radiation Safety Department.

#### *Dry Box for Handling the Radioactive Material*

An acrylic dry box was used to safely carry out the experiments with <sup>142</sup>Pr glass (Fig 3.11). The 5.5 mm thick acrylic blocked a considerable amount of the beta radiation. Exposure levels were measured during the experiment inside and outside the acrylic box and are reported in Table 3.1. An additional small acrylic shield was used to place the vial inside the acrylic dry box. This shield isolates the samples from the external environment and prevents dispersion of the microspheres through the air. The front pannel has two holes placed on the edges for the handling the sample. Long tweezers, long wrenches and a double layer of rubber gloves were used to manipulate the radioactive samples through the access holes. An access door to the dry

box (Fig 3.11, left side) was used to place the solid water phantom and all the tools needed before to start the experiment.



**Figure 3.11:** Dry box, water phantoms, shield, long pliers and micropipettes used to carry the  $^{142}\text{Pr}$  measurements.

### *Handling the Microspheres Solution*

A syringe shield (Figure 3.12) was used for handling and distributing the radioactive solution. The Beta Syringe Shield<sup>®</sup> reduces hand exposure from syringes containing Strontium-

89, Phosphorus-32, and other beta-emitting radiopharmaceuticals. The barrel of the syringe shield is constructed of 0.375 inches clear plastic with a 0.062 inches thick embedded lead lining, which attenuates beta emission and some bremsstrahlung photons. The lead lining is interrupted at the viewing window for clear visibility when drawing and administering the dose. A thumbscrew holds syringes firmly in place. In the current experiment, a syringe with a long needle was used to manipulate the radioactive microspheres solution.



**Figure 3.12** Beta syringe Shield

All the measurements were performed inside the dry box and plastic gloves were used to avoid contamination. Exposure measurements were performed to verify the shielding and safety of the experimental procedure. The sample manipulation lasted a total of 10 minutes. Right and left hand ring badge and total body badge were using during the experiments. Measurements with a portable ion chamber (Eberline RO-20, Thermo Instrument Systems Inc.) registered the values described in Table 3.1, prior to the sample manipulation.

**Table 2.1:** Measured exposure rates

<b>Location</b>	<b>Detector window</b>	<b>Exposure</b>
10 cm from microspheres	<b>Open</b>	15,000 mrem/h
10 cm from microspheres	<b>Closed</b>	37 mrem/h
Outside Acrylic Box (top)	<b>Open</b>	4 mrem/h
Outside Acrylic Box (top)	<b>Closed</b>	3 mrem/h
Right Hand Aperture	<b>Open</b>	10 mrem/h
Left Hand Aperture	<b>Open</b>	80 mrem/h
Front Part of the Shield	<b>Open</b>	8.5 mrem/h
Front Part of the Shield	<b>Closed</b>	2 mrem/h
Eye Height	<b>Open</b>	40 mrem/h

During the entire decay of the nuclide, the samples were located in a controlled room, with restricted access to the general public, located in the first floor of the Howell Science Complex, at East Carolina University.

## CHAPTER 4: RESULTS

### 4.1 $^{142}\text{Pr}$ MICROSPHERE BRACHYTHERAPY

#### 4.1.1 Biological Effective Dose for $^{142}\text{Pr}$ and $^{90}\text{Y}$

The calculated values for BED for both  $^{142}\text{Pr}$  and  $^{90}\text{Y}$  are listed in Table 4.1. An  $\alpha/\beta$  value of 10 Gy (tumoral liver), and a total physical dose (PD) of 150 Gy was used for both radionuclides. For example, for the lowest DT value considered (17 days), corresponding to the fastest growing tumor reported in the clinical literature, the BED calculated for  $^{90}\text{Y}$  was 104.9 Gy, while the BED calculated for  $^{142}\text{Pr}$  was 260.0 Gy, representing an increase of 147 %. For the highest DT recorded, 720 days, calculated BED for  $^{90}\text{Y}$  was 192.3 Gy and for  $^{142}\text{Pr}$  it was 299.6 Gy, representing a 56.3 % increase in the BED. According to the calculated values of BED, the difference among radionuclides increases as the doubling time decreases, with the difference being more significant for rapid growing tumors. For the healthy tissue, the calculated BED for a total physical dose of 10 Gy was 12.0 Gy for  $^{142}\text{Pr}$  and 9.02 Gy for  $^{90}\text{Y}$ . The comparison of BEDs for tumor and normal tissue in liver with physical dose are shown in Figure 4.1.

**Table 4.1:** Calculated BED values for 150 Gy physical total doses for both  $^{142}\text{Pr}$  and  $^{90}\text{Y}$ . BED calculated for the three ranges of tumor growth or Doubling Times (DT) for the different types of HCC. The distribution of DT values for each tumor type is positively skewed, therefore, ranges of values were considered for BED calculation, instead of a mean value. DT ranges for each tumor type were: well differentiated (38-720 days), moderately differentiated (17-380 days) and poorly differentiated HCCs (20-70 days) (41). It is observed that the difference for BED values is more pronounced for rapid growing tumors.

<b>Tumor Type</b>	<b>Well differentiated</b>		<b>Moderately differentiated</b>		<b>Poorly differentiated</b>	
<b>DT (days)</b>	38	720	17	380	20	70
<b>BED (Gy) <math>^{90}\text{Y}</math></b>	143.4	192.3	104.9	188.5	114.0	162.8
<b>BED (Gy) <math>^{142}\text{Pr}</math></b>	279.1	299.6	260.0	298.1	264.8	287.7
<b>% Change</b>	95.1%	56.3%	148%	58.1%	132%	76.7%

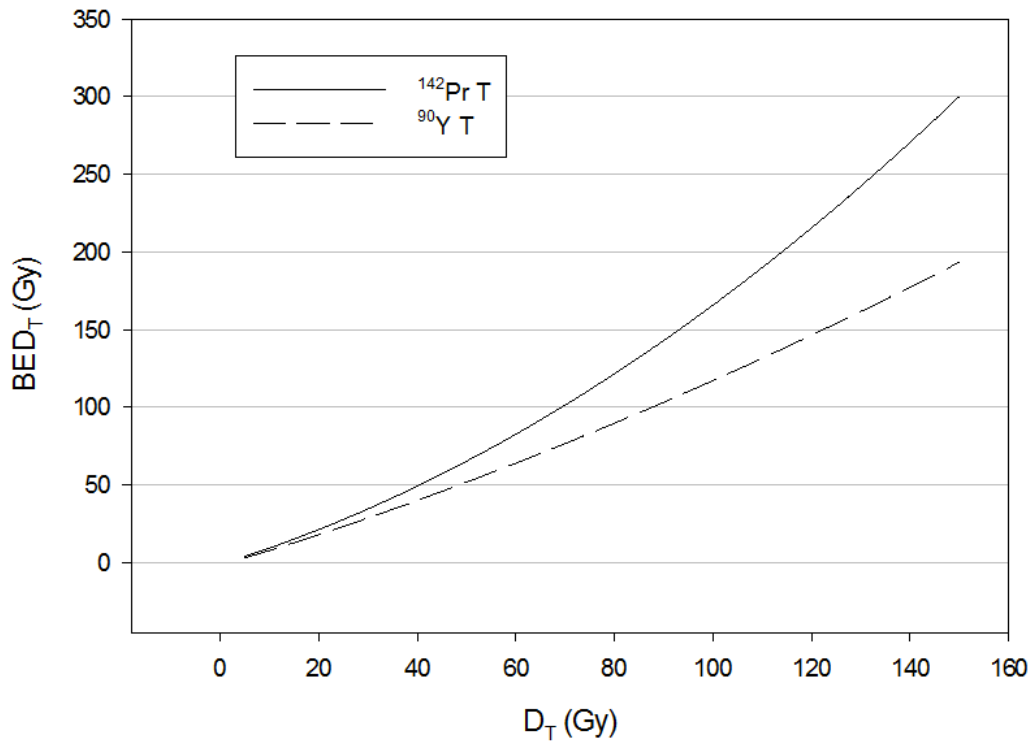
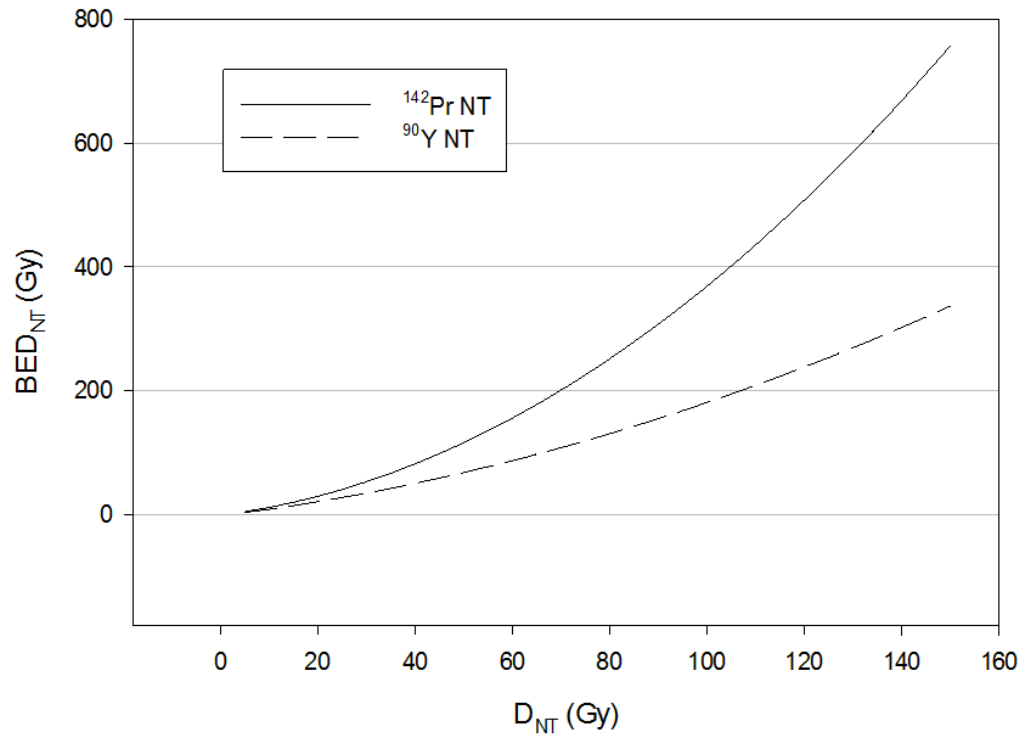


**Figure 4.1** Biological Effective Dose for tumor and non-tumor tissues.

### 4.1.2 MCNPX2.6 Monte Carlo Simulations

Plots of the calculated DPK for 1 MBq  $^{142}\text{Pr}$  and  $^{90}\text{Y}$  point sources are shown in Figure 4.2. DPK calculation results for  $^{90}\text{Y}$  were also compared with results available in the literature and benchmarked with the experimental data (Berger, 1971). The default units for dose deposition in MCNPX2.6 outputs are MeV/g per decay. Therefore the following conversion factor was used to convert the units to Gy per decay:

$$1 \frac{\text{MeV}}{\text{g}} = \frac{1.6022 \times 10^{-13} \text{J}}{10^{-3} \text{Kg}} = 1.6022 \times 10^{-10} \text{Gy} \quad \text{Eq. 4.1}$$

DPK calculations of dose versus distance for  $^{90}\text{Y}$  were in close agreement with Berger values for all relevant distances considered in this work. The dose rates obtained using MCNPX2.6 and BRAIN-DOSE were 0.120 mGy/h and 0.119 mGy/h respectively, at 0.5 cm away from the source. Dose distributions from BRAIN-DOSE and MCNPX2.6 codes for a 1 MBq  $^{142}\text{Pr}$  point source are displayed in Figure 4.3.

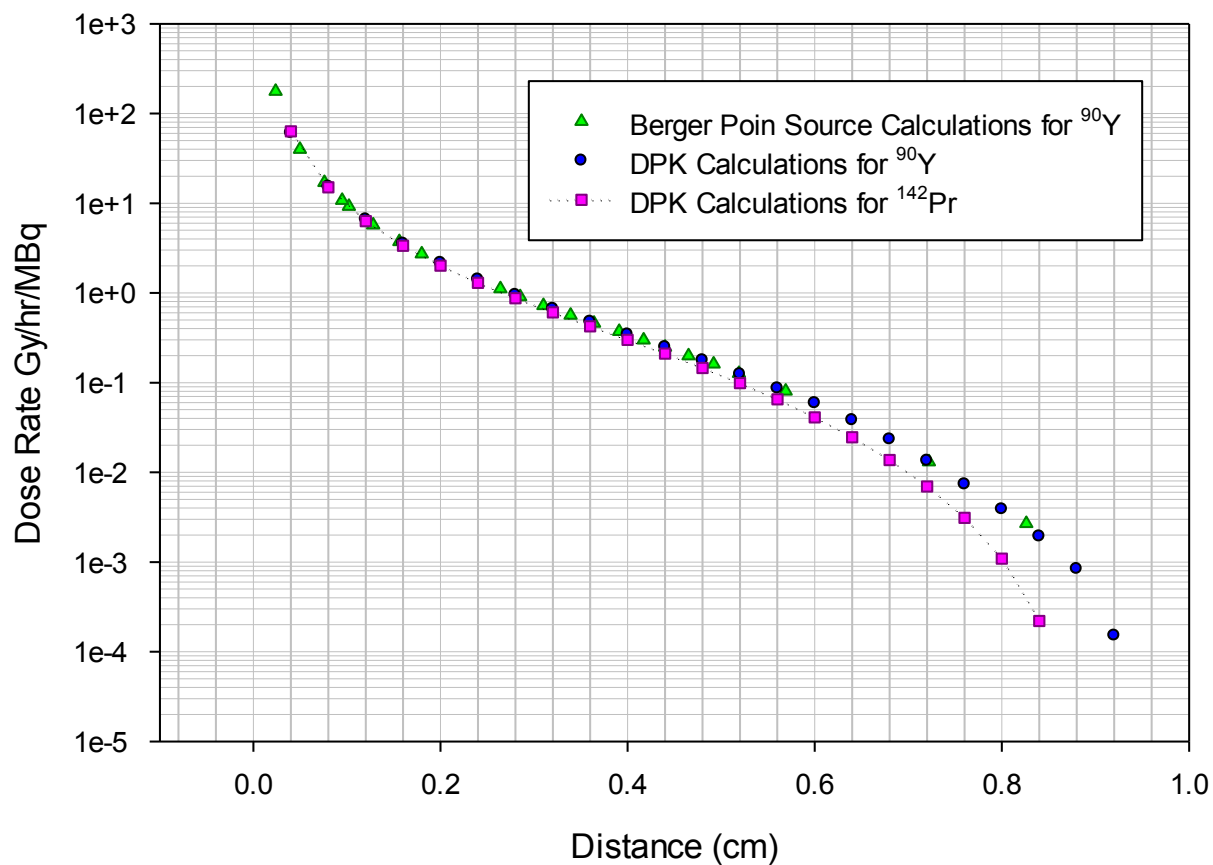


**Figure 4.2** DPK calculations for  $^{90}\text{Y}$  and  $^{142}\text{Pr}$  and comparison with the benchmarked Berger's point source calculations for  $^{90}\text{Y}$ .

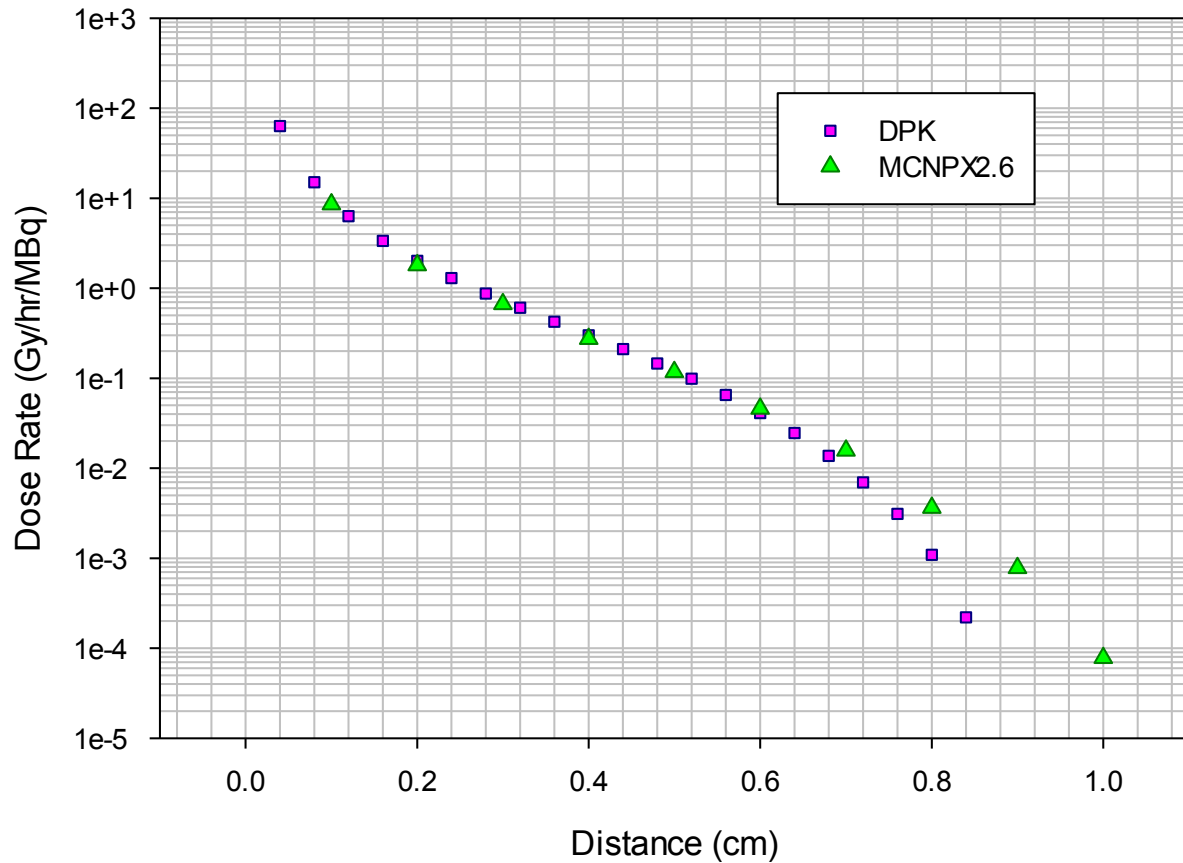


**Figure 4.3** DPK calculations and MCNPX simulation of the dose distribution for  $^{142}\text{Pr}$ . A good agreement is observed among both methods.

The calculated dose using BRAIN-DOSE code was 4.26% higher than that of MCNPX2.6 code for this distance. MCNPX2.6 provided the dose per particle for both beta and gamma contributions for  $^{142}\text{Pr}$  and beta contribution for  $^{90}\text{Y}$ . For distances beyond 0.6 cm MCNPX2.6 presented a higher dose rate than the one observed for BRAIN-DOSE calculations. The differences between these results are due to the fact that MCNPX2.6 accounts for radiation backscatter and electron multiple interactions, as described by the continuous-slowing-down model. These considerations will increase the dose rate, especially for low energy electrons. BRAIN-DOSE uses the convolution method to calculate the dose, which does not account for energy straggling radiation (Mainegra-Hing et al., 2005), therefore yielding a lower dose for points away from the source. Even though the differences are large for points beyond 0.6 cm, the dose relative to the total dose for these points is low compared to the prescription dose, e.g. at 0.8 cm, MCNPX2.6 calculates 0.0139 cGy/hr and BRAIN-DOSE gives 0.0004 cG/hr, representing less than 0.05% of the dose rate at points close to the source.

The MCNPX2.6 simulation of the beta dose distributions for  $^{142}\text{Pr}$  microspheres within a 2.5 cm tumor are shown in the Figure 4.4. Comparison of the total physical dose along the central axis due to gamma and beta contributions for  $^{142}\text{Pr}$  and total physical dose due to beta contribution for  $^{90}\text{Y}$  are displayed in Figure 4.5. For these results, a target dose of 150 Gy within the tumor was used for both nuclides. From the simulation, a beta and gamma dose per decay of  $1.95 \times 10^{-12}$  Gy and  $9.77 \times 10^{-15}$  Gy, respectively, were obtained for  $^{142}\text{Pr}$  inside the tumor. A beta dose per decay of  $2.36 \times 10^{-12}$  Gy was obtained for  $^{90}\text{Y}$  at the same point. To obtain the desired total physical dose at the center, a total initial activity of 0.662 GBq and 0.191 GBq was calculated for  $^{142}\text{Pr}$  and  $^{90}\text{Y}$ , respectively. The beta contribution to the dose drops quickly to zero for points outside the tumor, in this case for points greater than 2.5 cm.

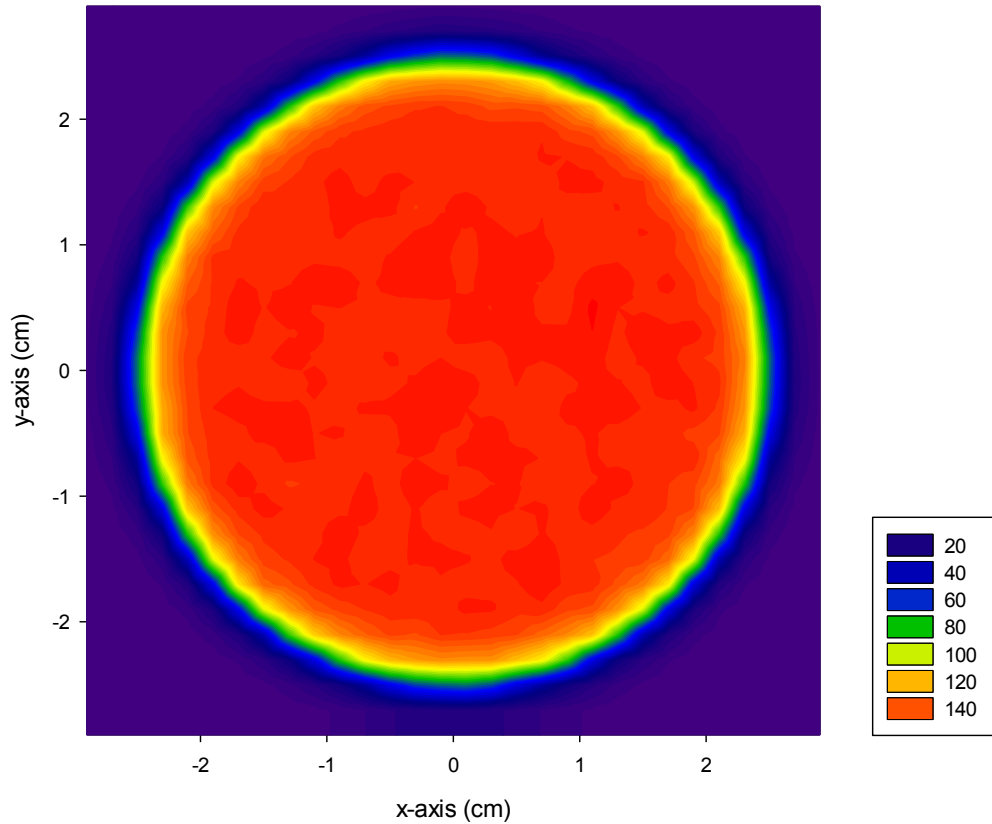


**Figure 4.4** Contour plot of the MCNPX2.6 simulation of dose (Gy) distribution for  $^{142}\text{Pr}$  microspheres in a 2.5 cm spherical tumor model (dose at the central plane of the tumor). The target physical dose was 150 Gy. The dose drops quickly to zero for regions outside the tumor, delivering a high dose inside the tumor and sparing the surrounding healthy tissues. Fluctuations observed on the top surface are due to statistical uncertainties intrinsic of the Monte Carlo method.

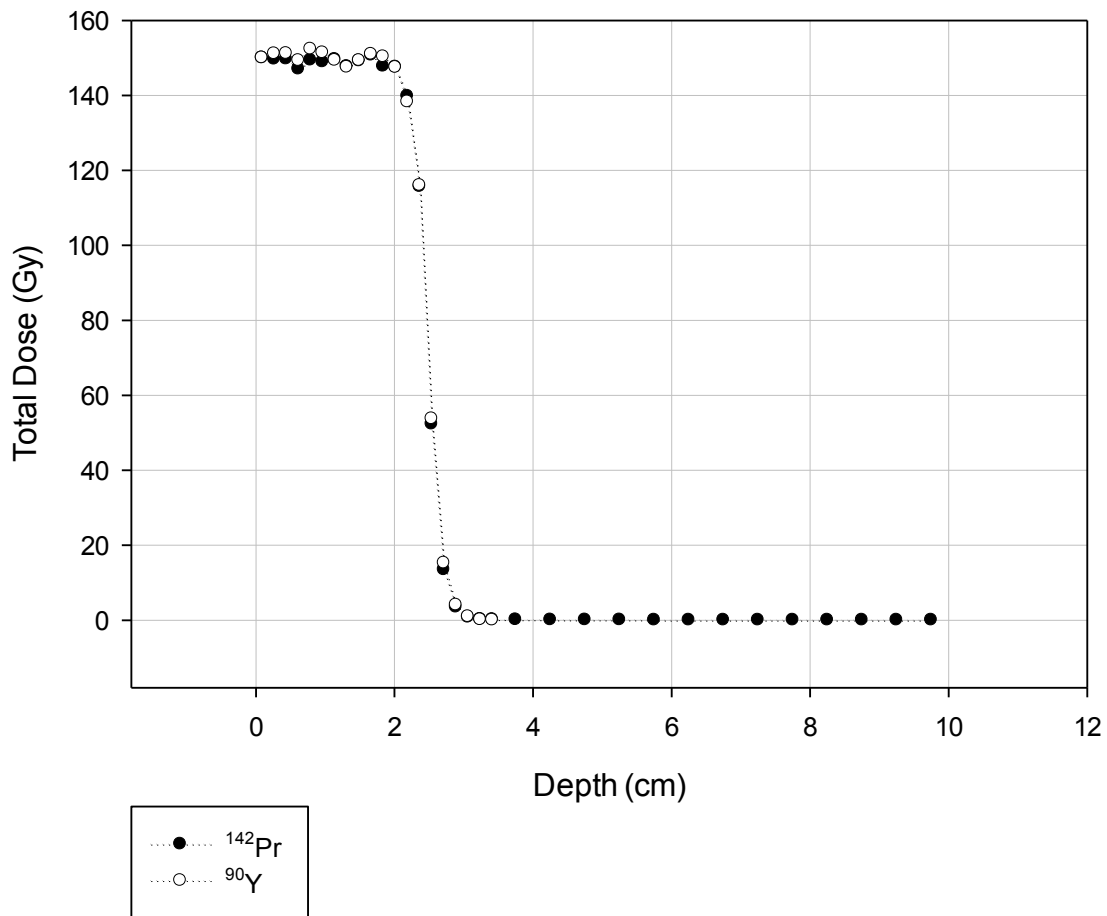


**Figure 4.5** Central axis view of the beta and gamma contributions to the dose due to  $^{142}\text{Pr}$  and beta contribution due to  $^{90}\text{Y}$ . Gamma contribution to the total dose for  $^{142}\text{Pr}$  cannot be distinguished in the plot, since it is about 100 times smaller than the beta dose at the origin. Doses due to  $^{90}\text{Y}$  are due to beta only and decay quickly to zero.

Different sizes of spherical tumors were also considered to determine dose distributions inside the tumor and in the tumor surroundings. Dose per disintegration for tumor radii of 1.0, 2.0, 2.5, 3.0, 4.0 and 5.0 cm are displayed in Figure 4.6. Total dose distributions due to the gamma contributions (during entire life of the nuclide) were obtained for a 1.0 cm sphere and compared with results obtained by MCNPX2.6 simulation (Figure 4.7). A 9 GBq vial of  $^{142}\text{Pr}$  homogeneously distributed within a 1 cm radius tumor was used. Overall, a good agreement was observed between MCNPX2.6 simulation and analytical calculations, with total dose within 1% for points at the tumor center.

The dose distribution within the tumor for blood vessels completely filled with  $^{142}\text{Pr}$  and  $^{90}\text{Y}$  are shown in Figure 4.8. The total physical dose distributions near the modeled blood vessels both inside the tumor and at the tumor periphery completely filled with  $^{142}\text{Pr}$  are shown in Figure 4.9. The total dose was calculated considering the total decays from the entire treatment period of 120 microspheres, or  $1.0 \times 10^{11}$  decays.

Based on the simulated physical dose distribution, the BEDVH distributions both  $^{90}\text{Y}$  and  $^{142}\text{Pr}$  was calculated for 150 Gy (Figure 4.10). The summary of these findings for all the tumor vessels and tumor sizes studied are listed in Table 4.2 for tumor DT of 20 days. The ambient dose rates due to the  $^{142}\text{Pr}$  gamma component calculated for a vial containing  $1.2 \times 10^6$  microspheres (10.1 GBq) of  $^{142}\text{Pr}$  was 0.081 mSv/hr. For this vial size and the entire life of this nuclide the total exposure is calculated to be 2.24 mSv. This calculation was based on conservative assumption that the attenuation from body was not accounted for and the family or caregivers stayed with the patient at 1 meter during entire treatment period.

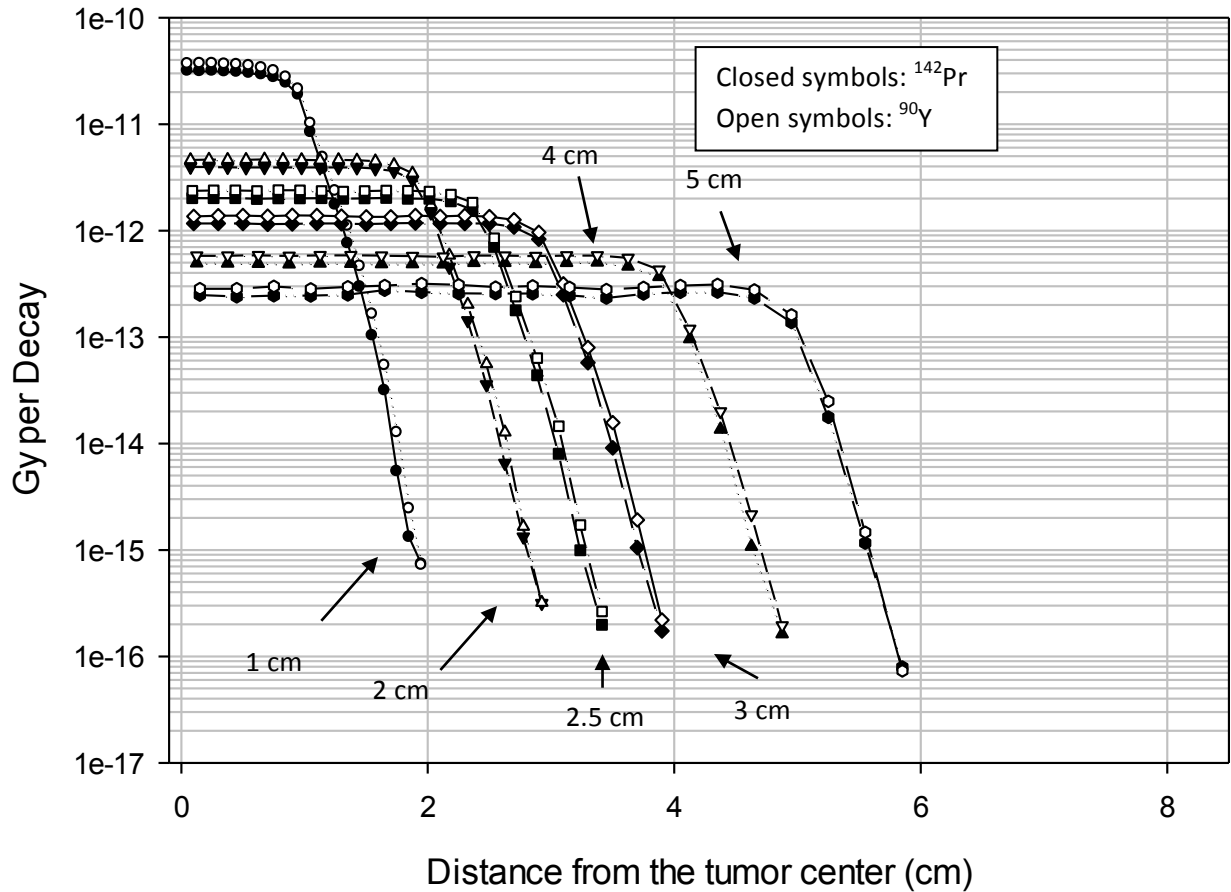


**Figure 4.6** Tumor radiuses ranging from 1 cm to 5 cm. Comparable dose decay curves along the central axis per beta decay for  $^{142}\text{Pr}$  (filled symbols) and  $^{90}\text{Y}$  (unfilled symbols).

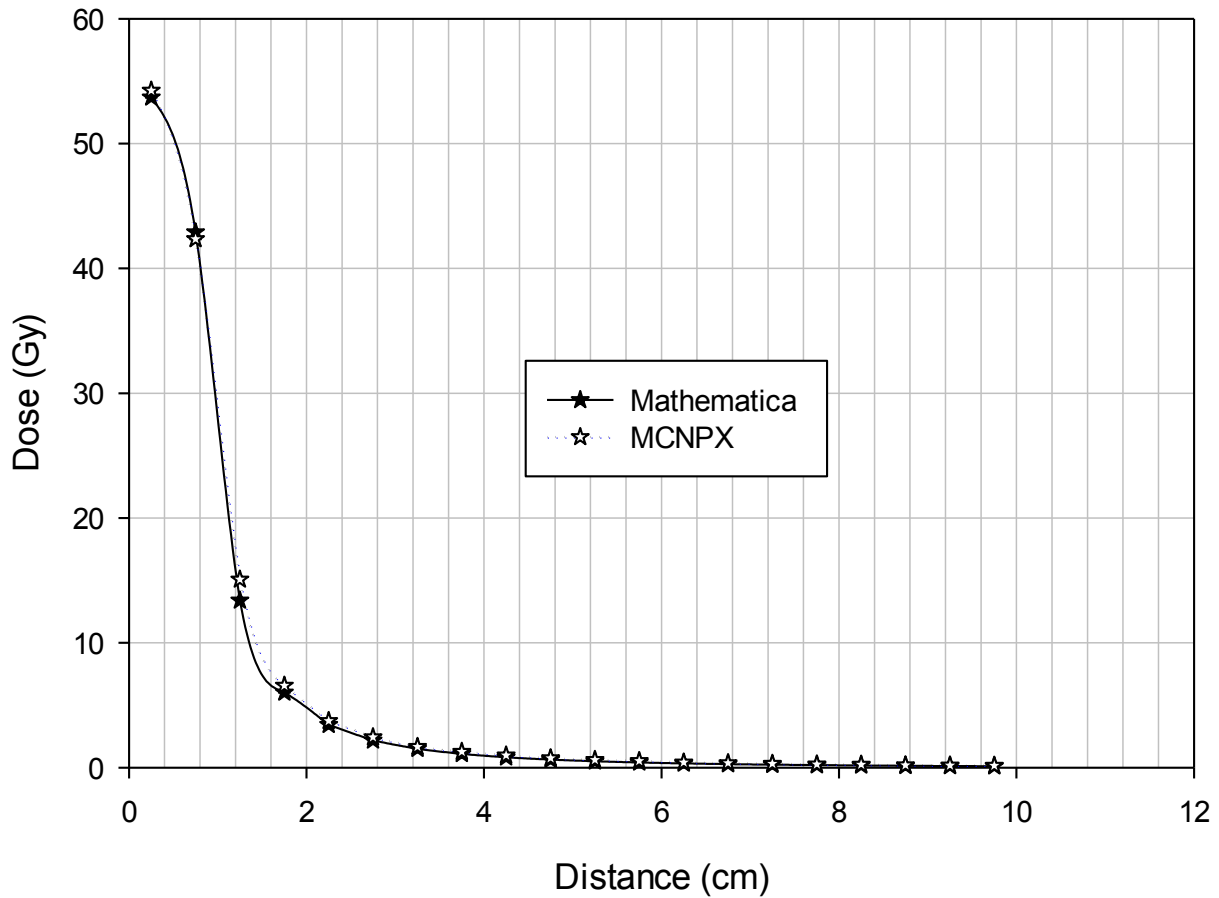


**Figure 4.7** Validation of the MCNPX simulations for the  $^{142}\text{Pr}$  gamma dose distribution using the analytical calculations. Mathematica software was used to perform the volume integrals throughout the tumor. Initial activity of 9 GBq homogeneously distributed within a 1 cm radius tumor.

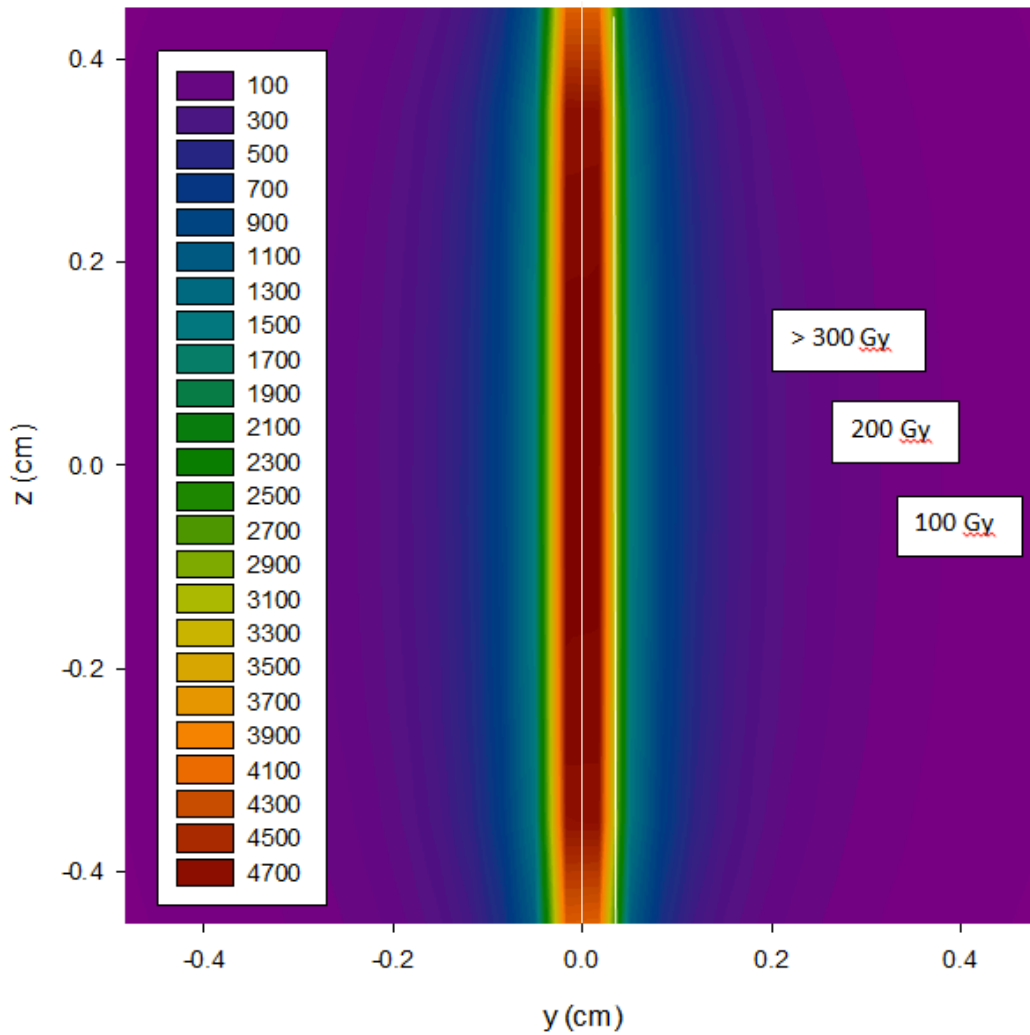


**Figure 4.8** Simulation of the dose distribution (Gy) generated by the 20 μm diameter blood vessel model (white line in the center) within a 0.5 cm tumor.

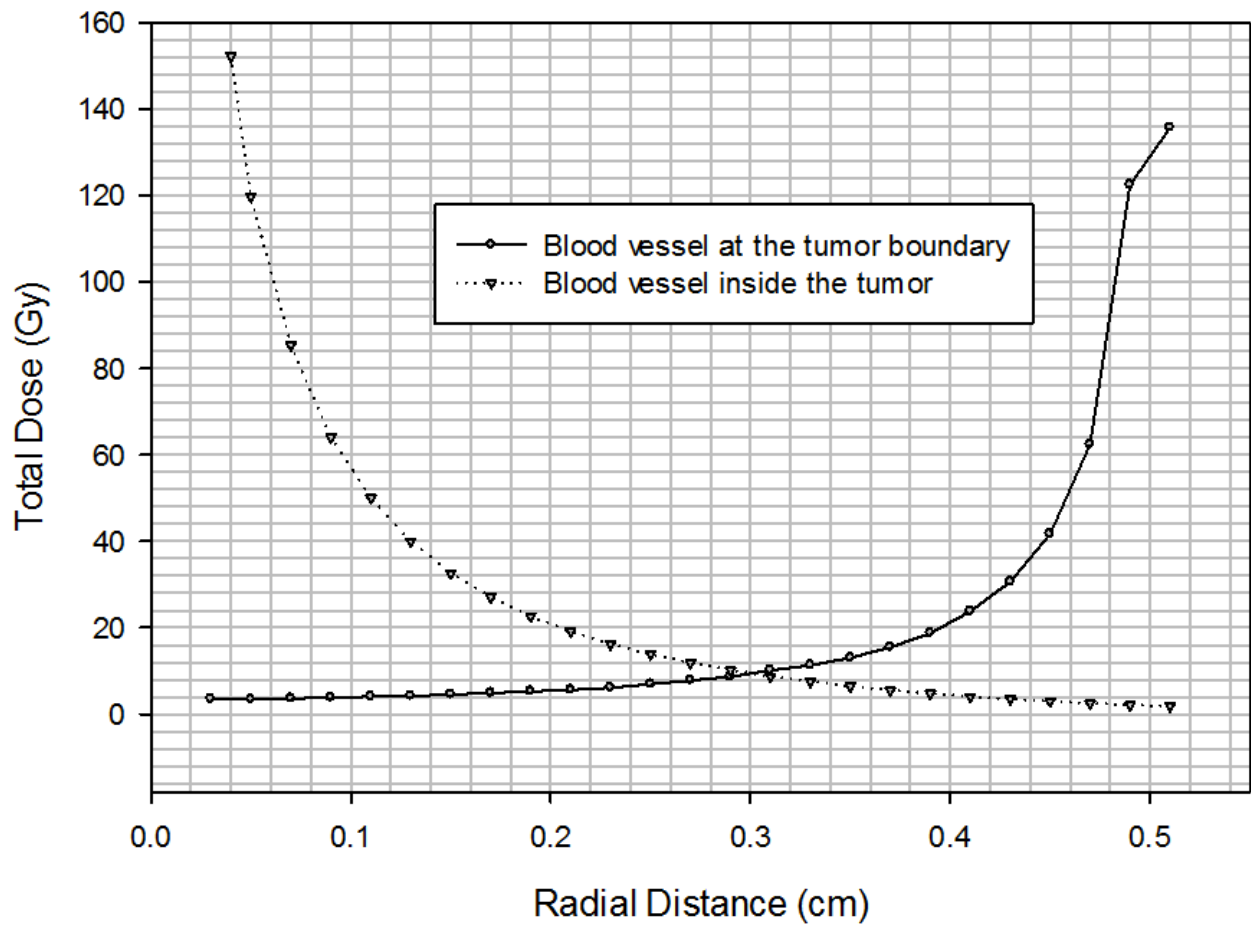


**Figure 4.9:** Dose distributions for a blood vessel placed in the center of tumor and placed at the tumor boundary.

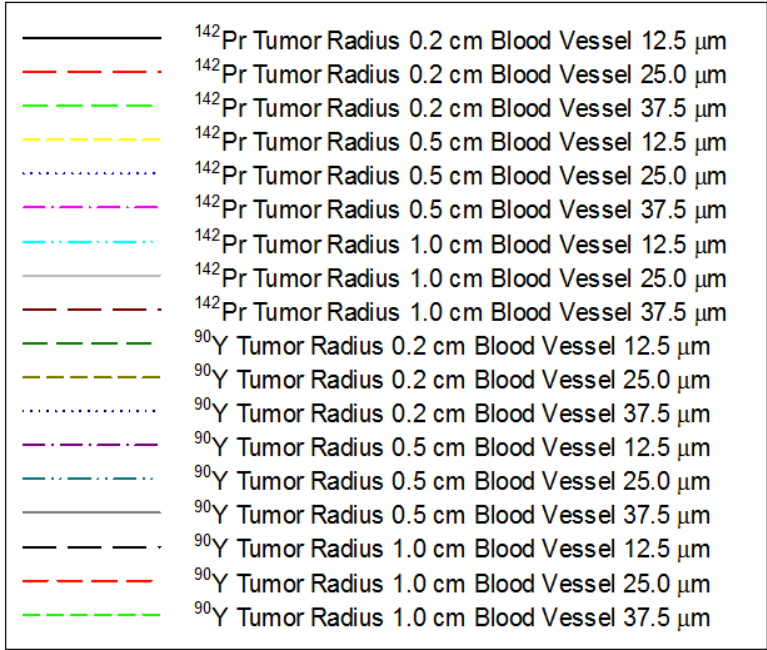
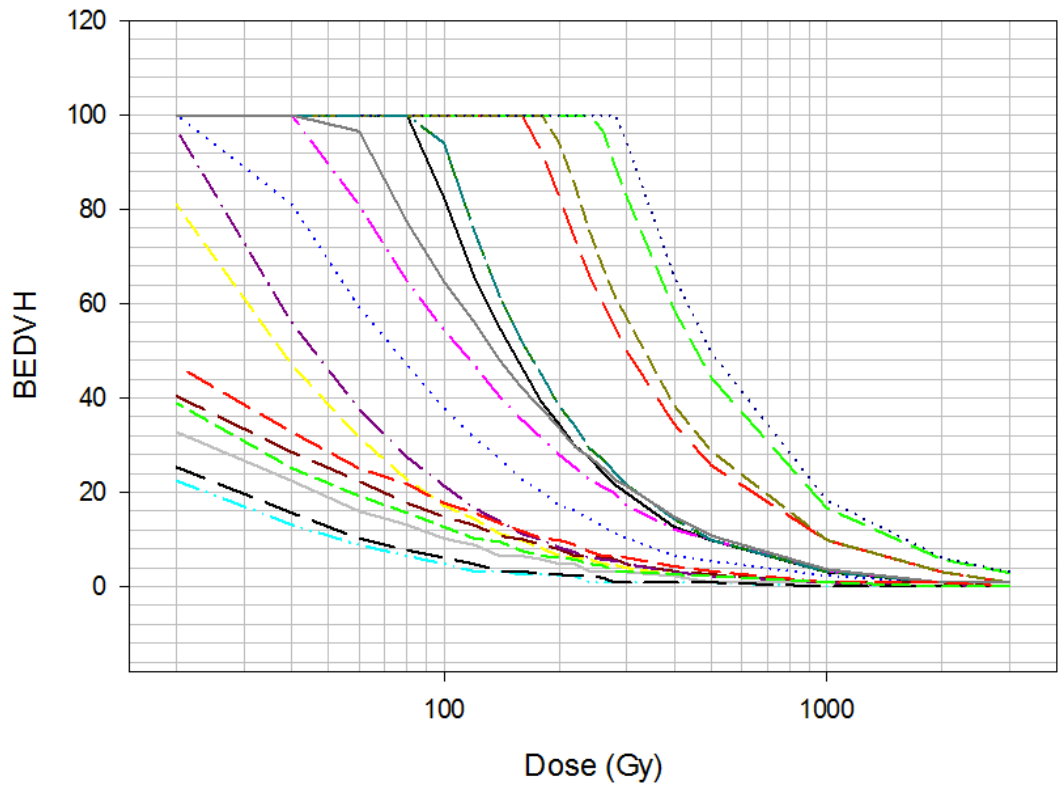


**Figure 4.10:** Biological effective dose volume histogram.

**Table 4.2:** Percent of the tumor volume covered with a BED higher than 150 Gy for different tumor radius and blood vessel diameters for both  $^{142}\text{Pr}$  and  $^{90}\text{Y}$  for a 20 days doubling time.

<b>Blood Vessel diameter*</b>							
		<b>25.0 <math>\mu\text{m}</math></b>		<b>50.0 <math>\mu\text{m}</math></b>		<b>75.0 <math>\mu\text{m}</math></b>	
<b>Tumor Radius</b>	$^{142}\text{Pr}$	$^{90}\text{Y}$	$^{142}\text{Pr}$	$^{90}\text{Y}$	$^{142}\text{Pr}$	$^{90}\text{Y}$	
<b>0.2 cm</b>	89.2	60.0	100	100	100	100	
<b>0.5 cm</b>	19.9	11.9	40.2	28.6	57.8	44.0	
<b>1.0 cm</b>	5.77	4.93	10.7	11.1	15.7	14.0	

\* Diameters were based on average hepatic blood vessel diameter sizes reported in the literature (Kennedy et al., 2004)

### **4.1.3 MCNPX2.6 Model for $^{142}\text{Pr}$ glass microsphere experimental design**

MCNPX2.6 outputs for the modeled experimental setup are displayed in Figure 4.11. The filled contour plots represent both xy and yz-axis dose distributions per decay. After multiplied by the total number of decays, the total dose profiles are compared in the next section with the experimental measurements. In addition, a linear profile (Figure 4.12) is plotted with more detailed information of dose (Gy) per decay as a function of the distance from the glass capillary.

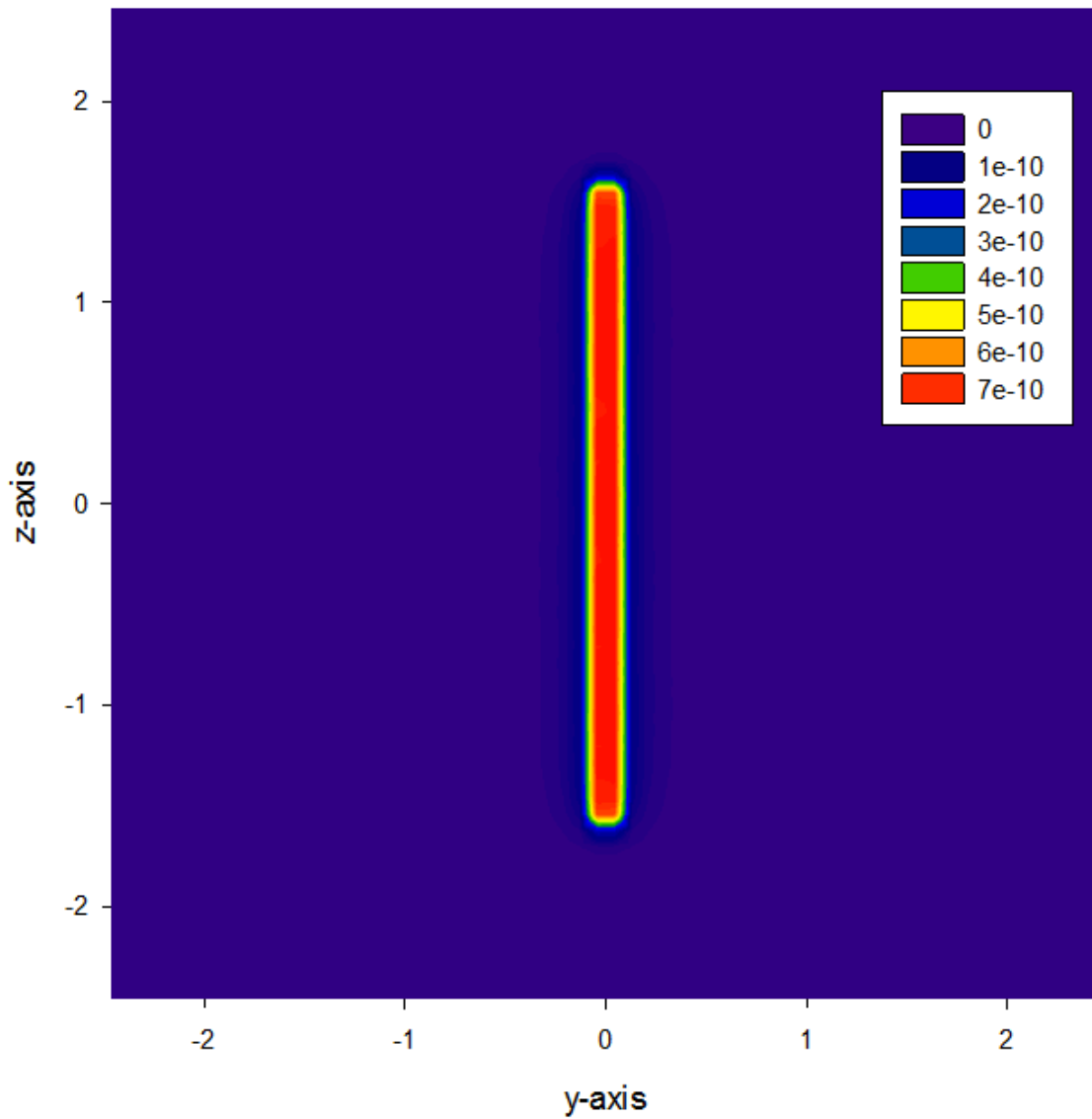


**Figure 4.11:** Dose (Gy) distributions per decay for a glass capillary filled with glass  $^{142}\text{Pr}$  microspheres, having internal diameter of 305  $\mu\text{m}$  and external diameter equals to 457  $\mu\text{m}$ .

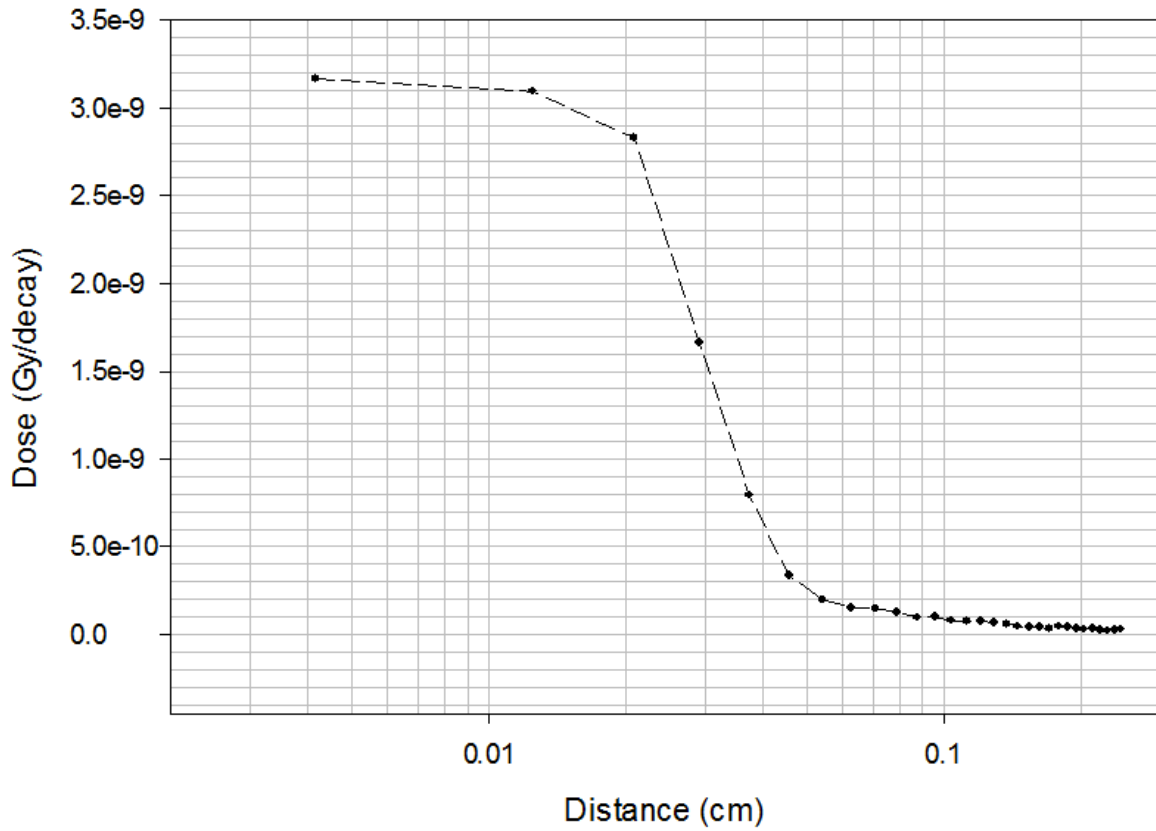


**Figure 4.12:** Linear-log plot of the dose distributions (Gy) per decay for a glass capillary filled with glass  $^{142}\text{Pr}$  microspheres, having internal diameter of 305  $\mu\text{m}$  and external diameter equals to 457  $\mu\text{m}$ .

## 4.2 <sup>142</sup>Pr CONFORMAL EYE BRACHYTHERAPY DEVICE

Results obtained for the simulations for dose within the eyeball for a glass <sup>142</sup>Pr rods and total dose of 85 Gy will be presented. Comparison of dose per decay for a total dose equal to 85 Gy for <sup>142</sup>Pr, <sup>90</sup>Y and <sup>188</sup>Re sources will also be presented and discussed in the following sections.

### 4.2.1 MCNPX2.6 <sup>142</sup>Pr Dose distribution within the eye

The beta dose profile found within the eyeball due to the glass <sup>142</sup>Pr rod (Figure 4.13) shows that this nuclide provides a short-range dose profile suitable for the treatment of superficial eye lesions. The dose at the eye surface was calculated as 85.0 Gy and 2.95 Gy at 5.00 mm with an error of less than 1% (i.e. 0.139 and 0.855% respectively). Figure 4.14 shows the log-log plot of the axial dose profile versus depth.

### 4.2.2 Comparison of <sup>142</sup>Pr, <sup>90</sup>Y and <sup>188</sup>Re dose distributions

The simulated dose per decay at 1 mm from the eye surface at the central axis for <sup>142</sup>Pr, <sup>90</sup>Y, and <sup>188</sup>Re, were  $4.16 \times 10^{-11}$ ,  $6.57 \times 10^{-11}$ , and  $3.85 \times 10^{-11}$  Gy respectively. The log-log plots of the dose per decay and total dose curves for all the nuclides studied are shown in Figure 4.15. For an 85 Gy total dose at the eye surface, the observed dose at 1 mm for <sup>142</sup>Pr, <sup>90</sup>Y, and <sup>188</sup>Re were 52.1, 55.3, and 50.5 Gy, respectively. Activation of <sup>142</sup>Pr and <sup>188</sup>Re can be achieved in low fluence neutron research reactor, making these nuclides more accessible and lowering production costs. For all nuclides studied, the beta dose profile showed that this device might provide very high doses at short ranges within the eyeball, suitable for the treatment of superficial eye lesions.

The radionuclide  $^{90}\text{Y}$  showed the highest dose per decay at the point studied, 70.6 % higher than  $^{188}\text{Re}$  and 57.9% higher than  $^{142}\text{Pr}$ . Dose penetration for  $^{90}\text{Y}$  was also higher than  $^{188}\text{Re}$  (9.5%) and  $^{142}\text{Pr}$  (6.1%).

Glass  $^{142}\text{Pr}$  CEBT device is a promising technique for the treatment of superficial eye cancers. One of the advantages of the  $^{142}\text{Pr}$  eye device is that it could be positioned for any particular desired dose distribution, according to the tumor shape and size. Monte Carlo simulation allows determination of the dose distribution for different configurations and sequences.

#### **4.2.3 MCNPX2.6 model for experimental design of one $^{142}\text{Pr}$ glass rod**

Simulated dose distribution within a squared water phantom using one rod is displayed in Figure 4.16. The first profile is the axial dose distribution of electrons within the water phantom. The second dose profile is the radial dose distribution at the water-air interface on top of the phantom. A mesh tally of  $30 \times 30 \times 30$  and having  $1 \text{ cm}^3$  was used in this simulation. A log-log plot of the radial profile of the dose distribution due to one rod in water is displayed in Figure 4.17.

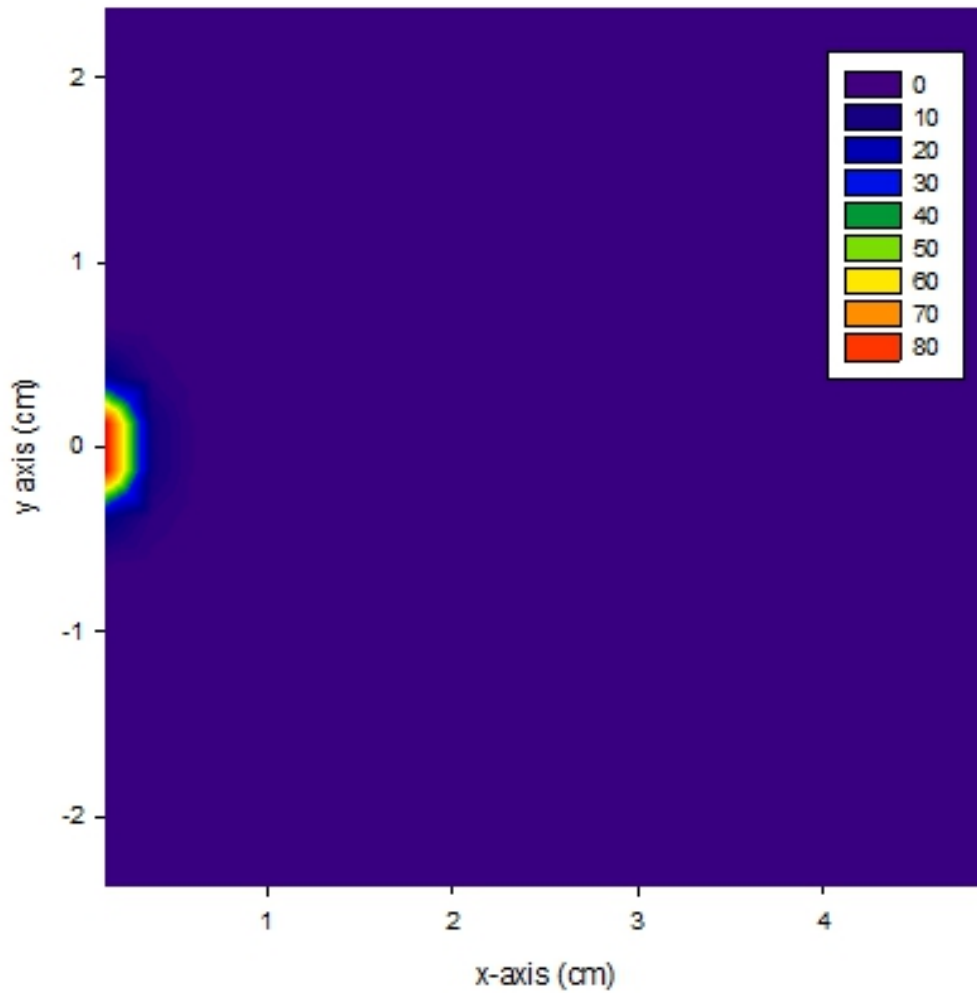


**Figure 4.13** Dose (Gy) distribution inside the eye for a  $^{142}\text{Pr}$  rod. A total dose 85 Gy was delivered at 0.01 cm from the eye surface.

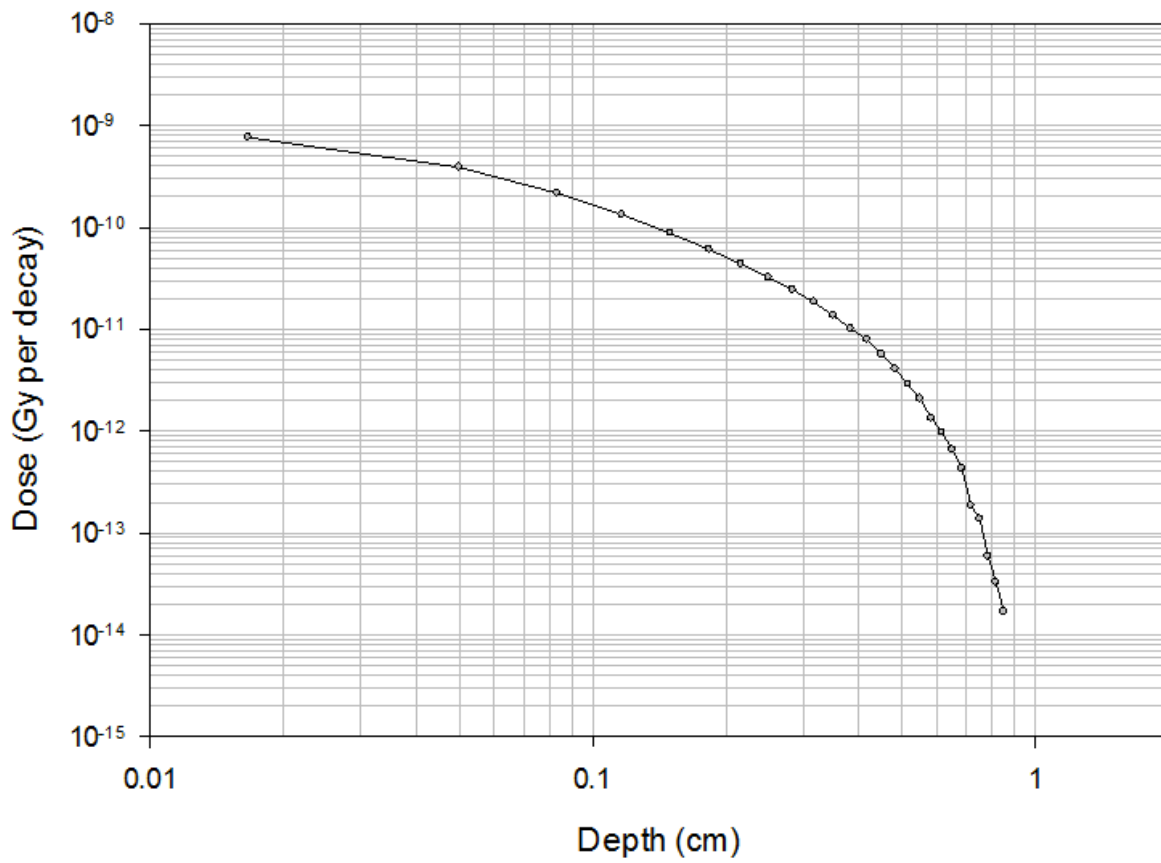


**Figure 4.14:** Axial profile of dose (Gy) per decay due to one  $^{142}\text{Pr}$  rod touching the eye surface.

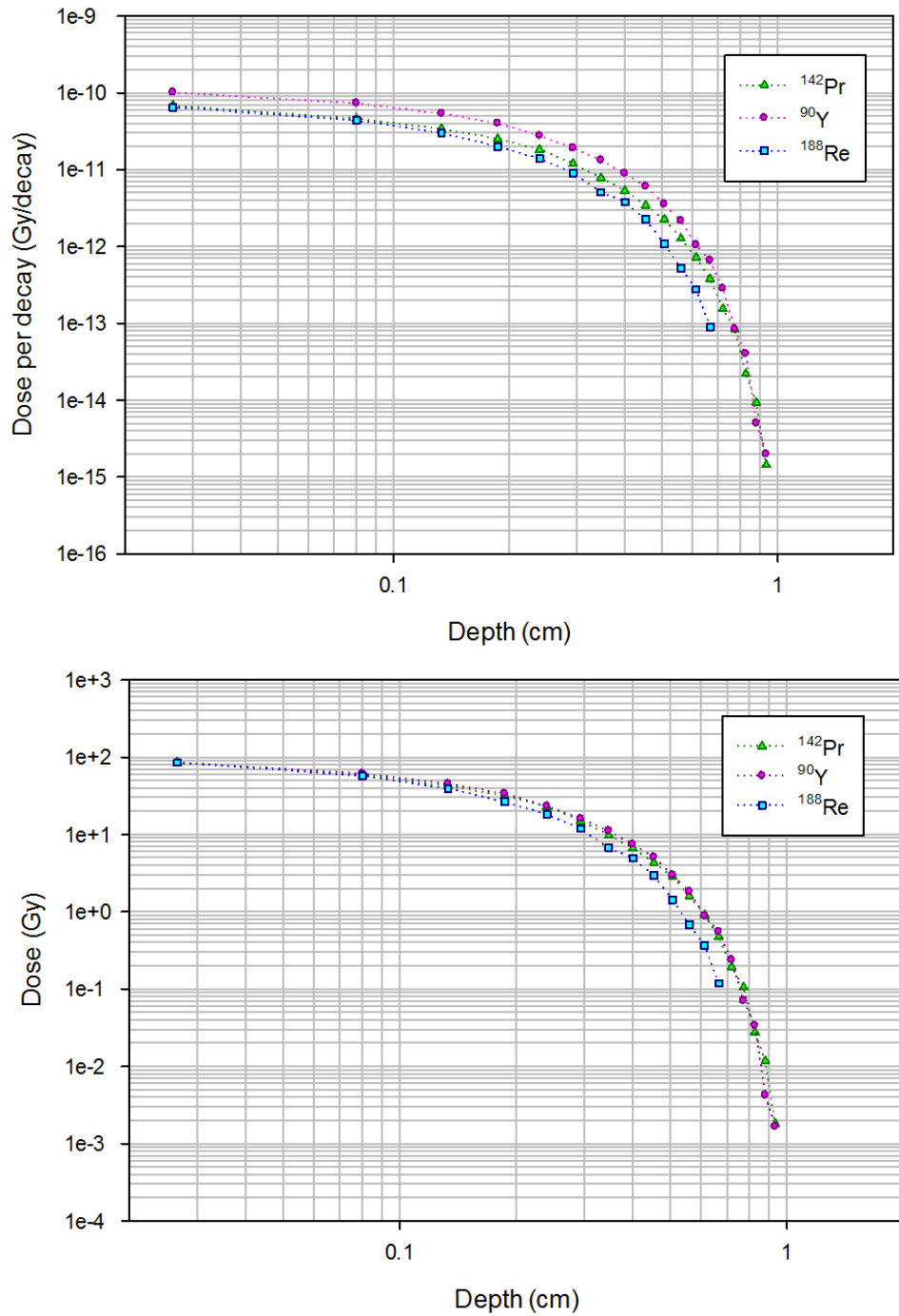


**Figure 4.15:** Comparison of dose profiles for  $^{142}\text{Pr}$ ,  $^{90}\text{Y}$  and  $^{188}\text{Re}$ . First plot shows dose per decay and second plot shows the dose distribution for 85 Gy dose at the surface.

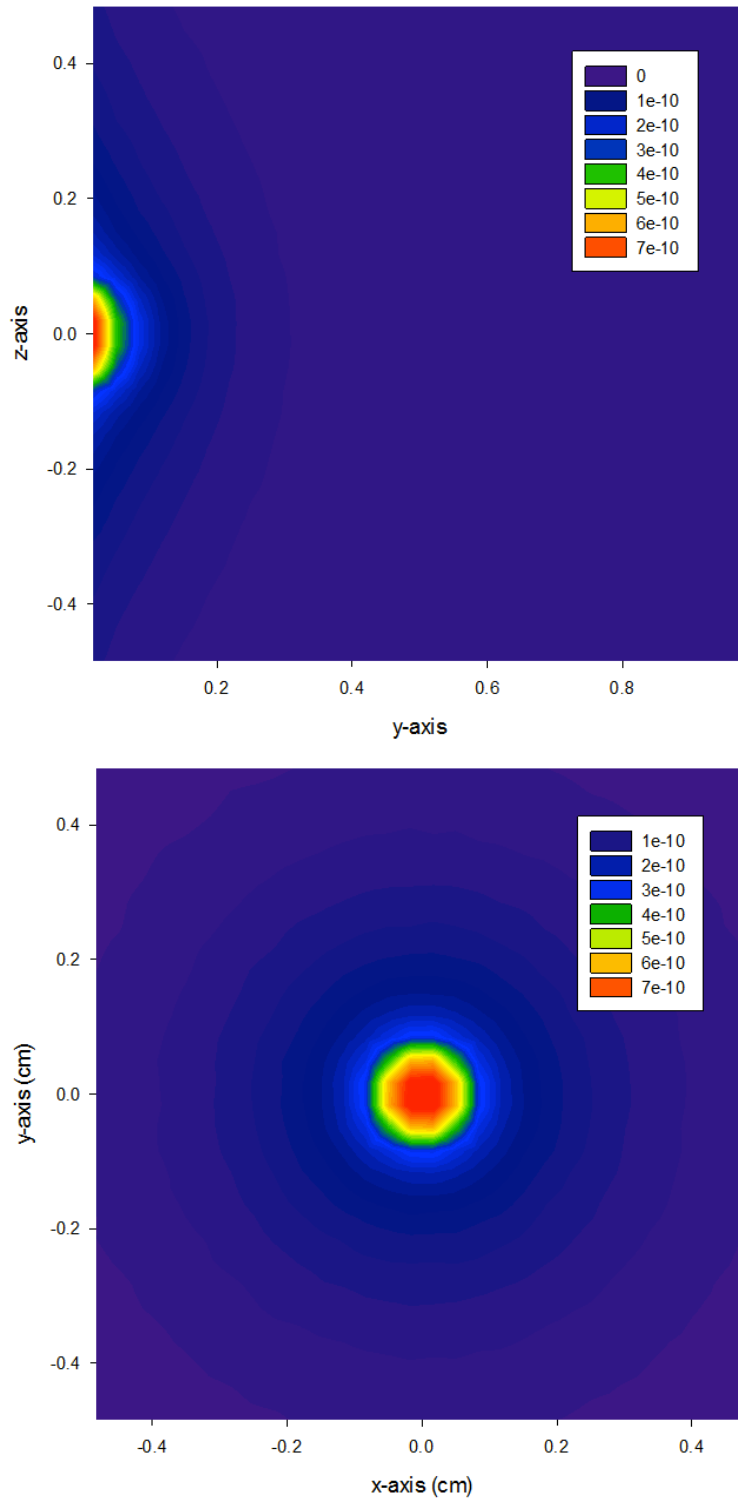


**Figure 4.16:** MCNPX2.6 transversal and radial simulations for the dose (Gy) per decay profile of model used for experimental setup.

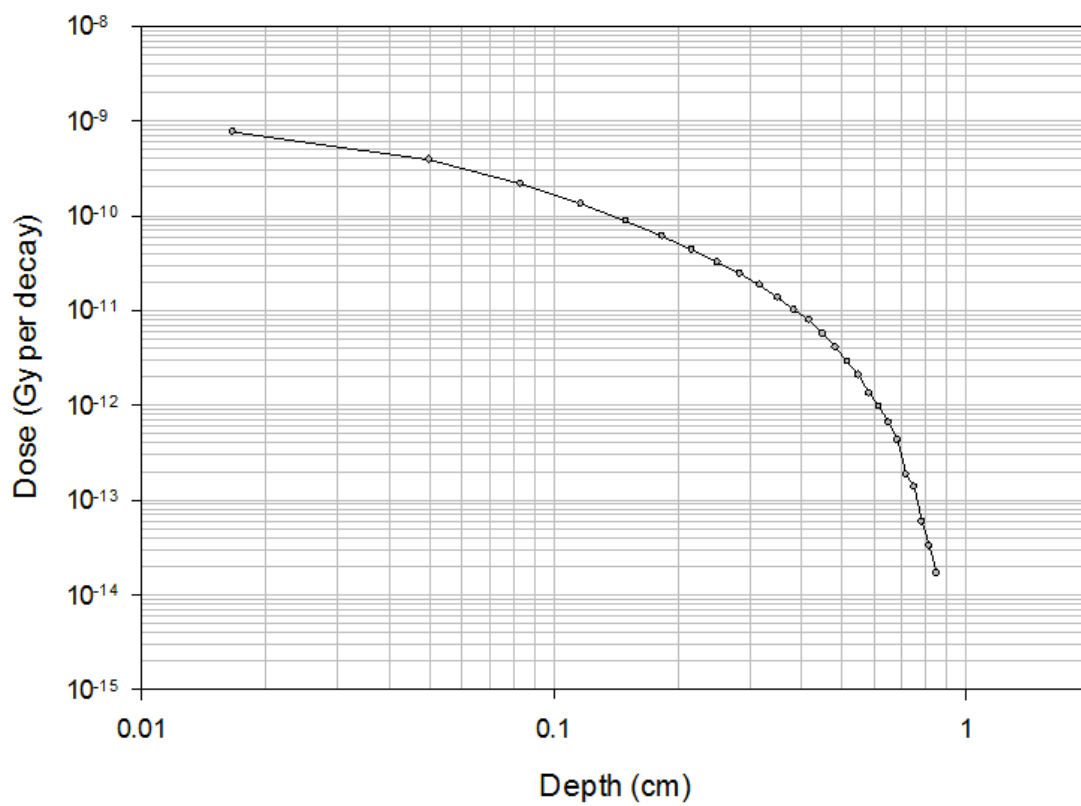


**Figure 4.17:** Axial profile of dose (Gy) per decay due to one  $^{142}\text{Pr}$  rod in contact with a squared water phantom.

### 4.3 Experimental Results and Monte Carlo Validation

Figure 4.18 shows the  $^{142}\text{Pr}$  spectrum measured with the NaI scintillator detector for 30 minutes. A 1578.2 keV peak was observed due to  $^{142}\text{Pr}$  gamma yield. Film measurements for  $^{142}\text{Pr}$  glass microsphere and rod are presented and compared with simulated dose profile.

#### 4.3.1 $^{142}\text{Pr}$ glass microspheres

Figure 4.19 shows the GAFCHROMIC<sup>®</sup> EBT2 film measurement for the glass capillary. Some dark spots are observed in the film, due to loose microspheres that were around the glass capillary before it was released in the water. The horizontal lines in the bottom are from imperfections in the scanner surface. The top part of the dose profile is wider than the bottom part, indicating a difference in microsphere concentration within the capillary. Figure 4.20 shows the isodose lines plotted in ImageJ. To plot the isodose lines, the image was split into RGB channels, and red component was converted into a 16-bit gray scale. Gray scale was calibrated using the gray value and corresponding film dose from the calibration in electron beam.

In order to compare the simulation results with the experimental data, the dose per decay was multiplied by the total decays. The final length of the capillary was 32.0 mm and it had internal diameter was 305  $\mu\text{m}$ . Considering that the average diameter of the microspheres was 29.7  $\mu\text{m}$  and the microsphere solution having  $30.8 \times 10^6$  microspheres per ml, a total number of 70,086 microspheres were estimated within the capillary. The total activity delivered at the time of experiment was 36.6 mCi ( $1.35 \times 10^9$  Bq) for a total of  $3.08 \times 10^6$  microspheres in a 0.169 g sample. Therefore, each microsphere had 440 Bq at the time of the measurements. The film was irradiated for 51 hours, therefore, the whole sample went through a total of  $2.6 \times 10^{12}$  decays.

Figure 4.21 shows the isodose lines for the MCNPX2.6 total dose simulations. The comparison for MCNPX2.6 simulations with film dosimetry are shown in Figure 4.22 for the glass microspheres. Measurements and simulations agree within 3.9 % for doses below 1600 cGy, e.g. experimental and simulated doses obtained at 0.5 cm from the source were 1547 cGy and 1610 cGy respectively. For doses of 1650 cGy and above, the sensitivity of the film is a limiting factor for accurately detecting doses. Therefore, a discrepancy is observed for this areas.

#### **4.3.2 $^{142}\text{Pr}$ glass rods**

Film measurements for an axial and transversal axis of the rods on top of a water phantom are presented in Figure 4.23. The isodose lines in cGy were plotted in ImageJ in the 16-bit red channel (Figure 4.24). To calculate the total number of decays, the total activity of the sample was divided by ten, which was the number of rods in the sample. Each rod had approximately 7.63 mCi (0.282 GBq), and stayed in the solid water phantom for 51 hours. A total number of decays of  $2.36 \times 10^{13}$  decays were calculated for 51 hours of decay. In Figure 4.25 the simulated dose profile (cGy) for the total number of decays is presented.

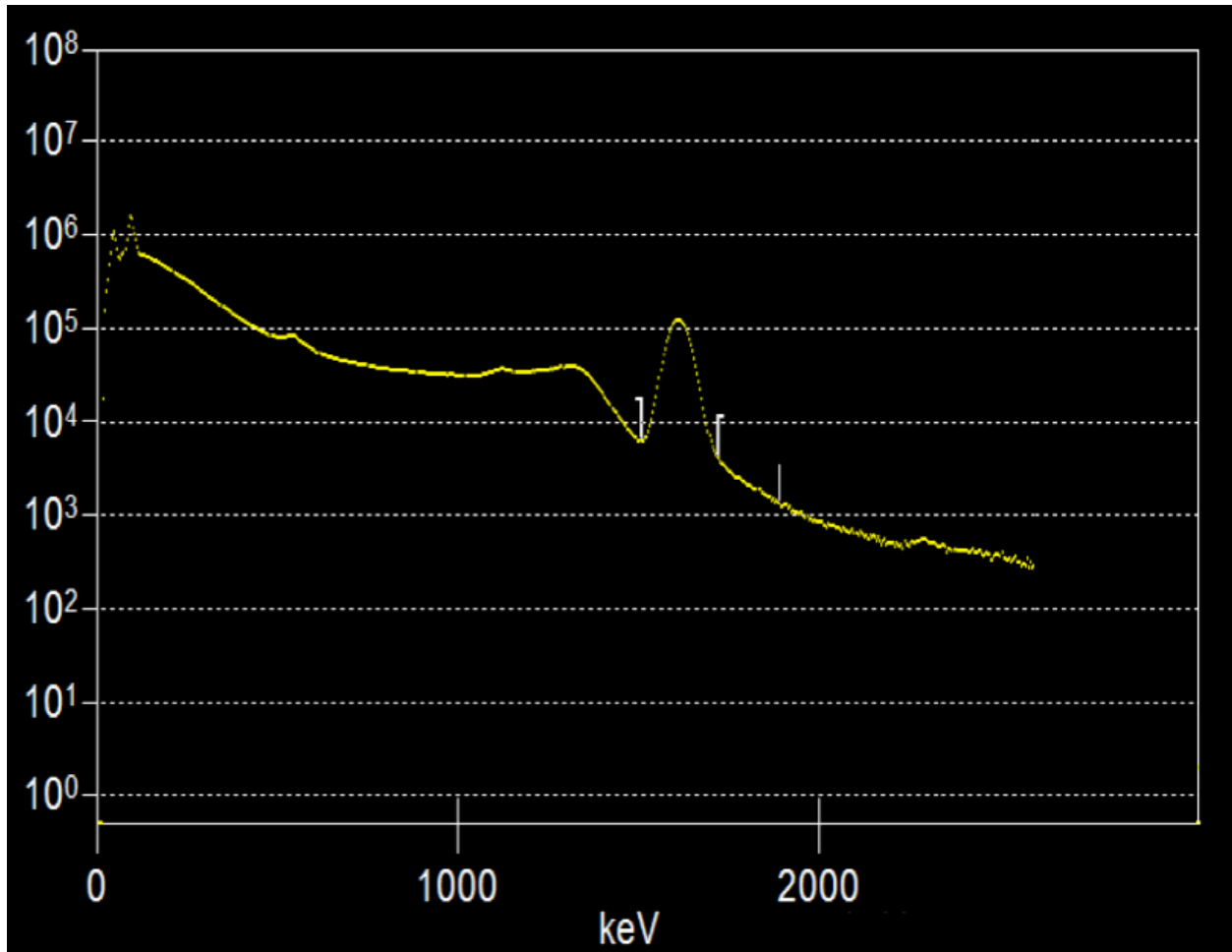


**Figure 4.18:**  $^{142}\text{Pr}$  Spectrum measured with the NaI scintillator detector. The peak observed is at the energy 1578.2 keV, corresponding to  $^{142}\text{Pr}$  gamma energy.

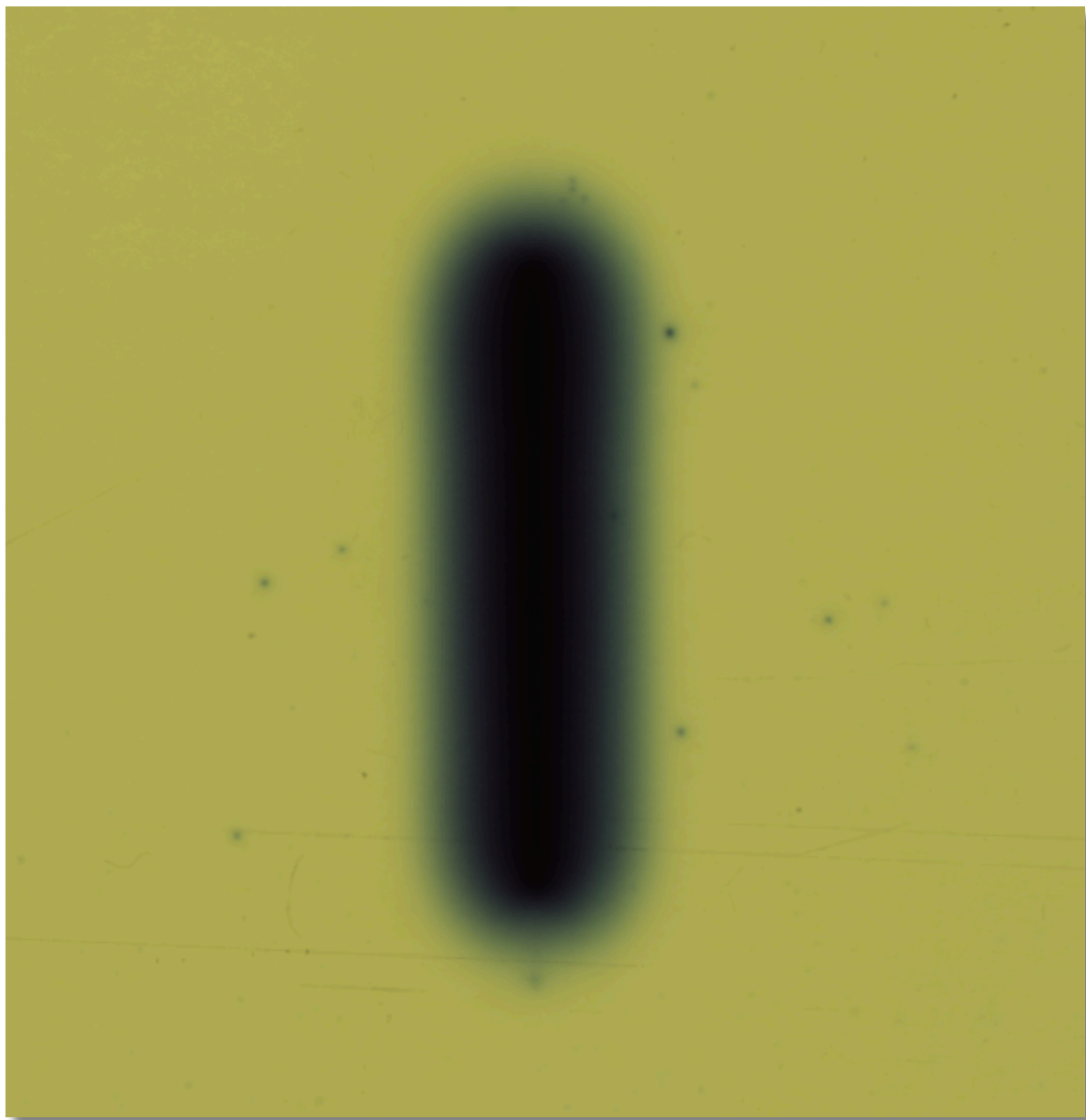


**Figure 4.19:** Raw scan of GAFCHROMIC<sup>®</sup> EBT2 film measurement for the glass capillary filled with <sup>142</sup>Pr microspheres. The small dark spots in the film are due to lose microspheres outside the capillary during pipetting. These microspheres dispersed in the water and deposited on the bottom of the phantom.

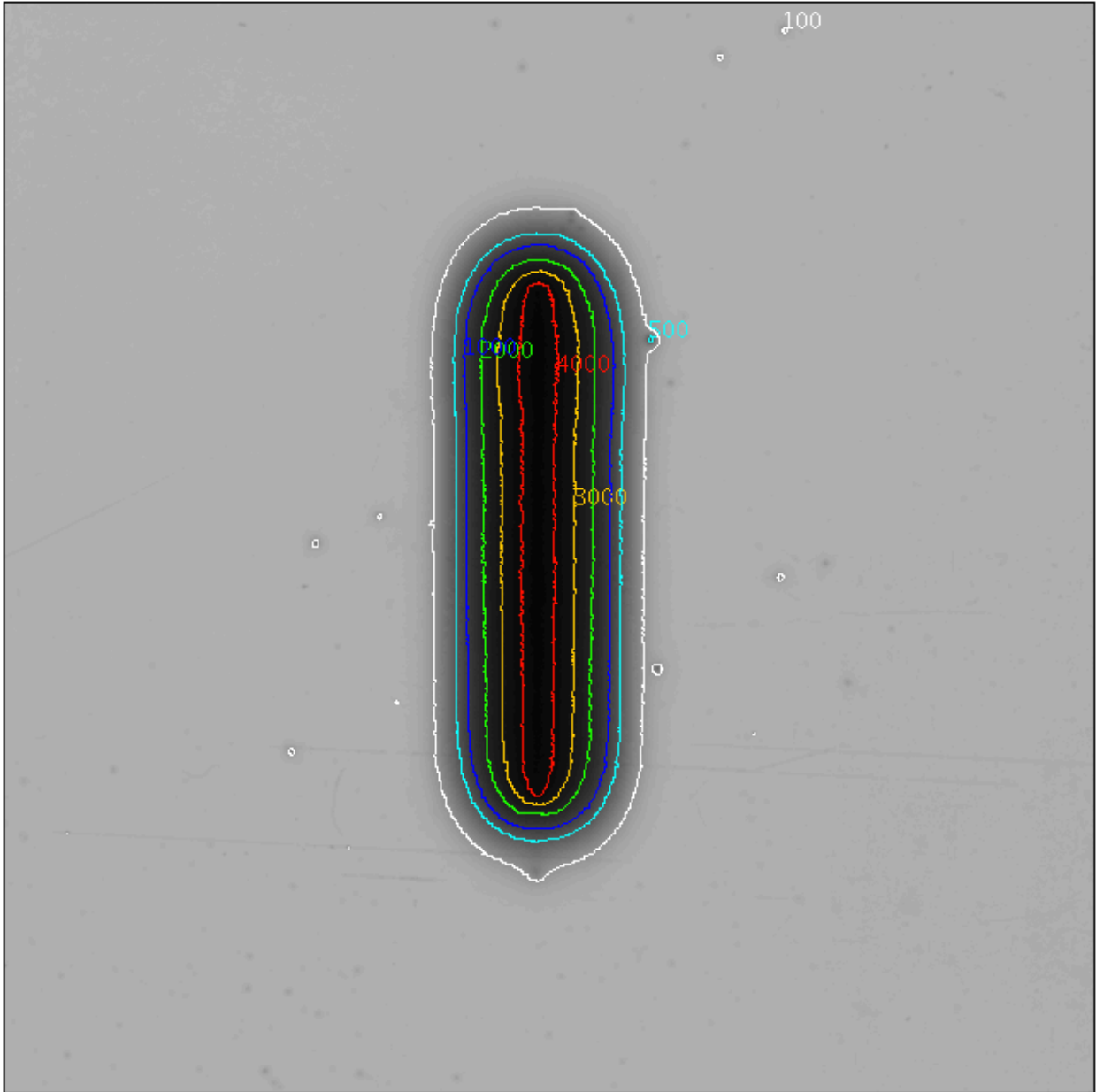


**Figure 4.20:** Isodose lines (cGy) for the glass microcapillary dose measurements in GAFCHROMIC<sup>®</sup> EBT2 film (red channel converted to a 16-bit image).

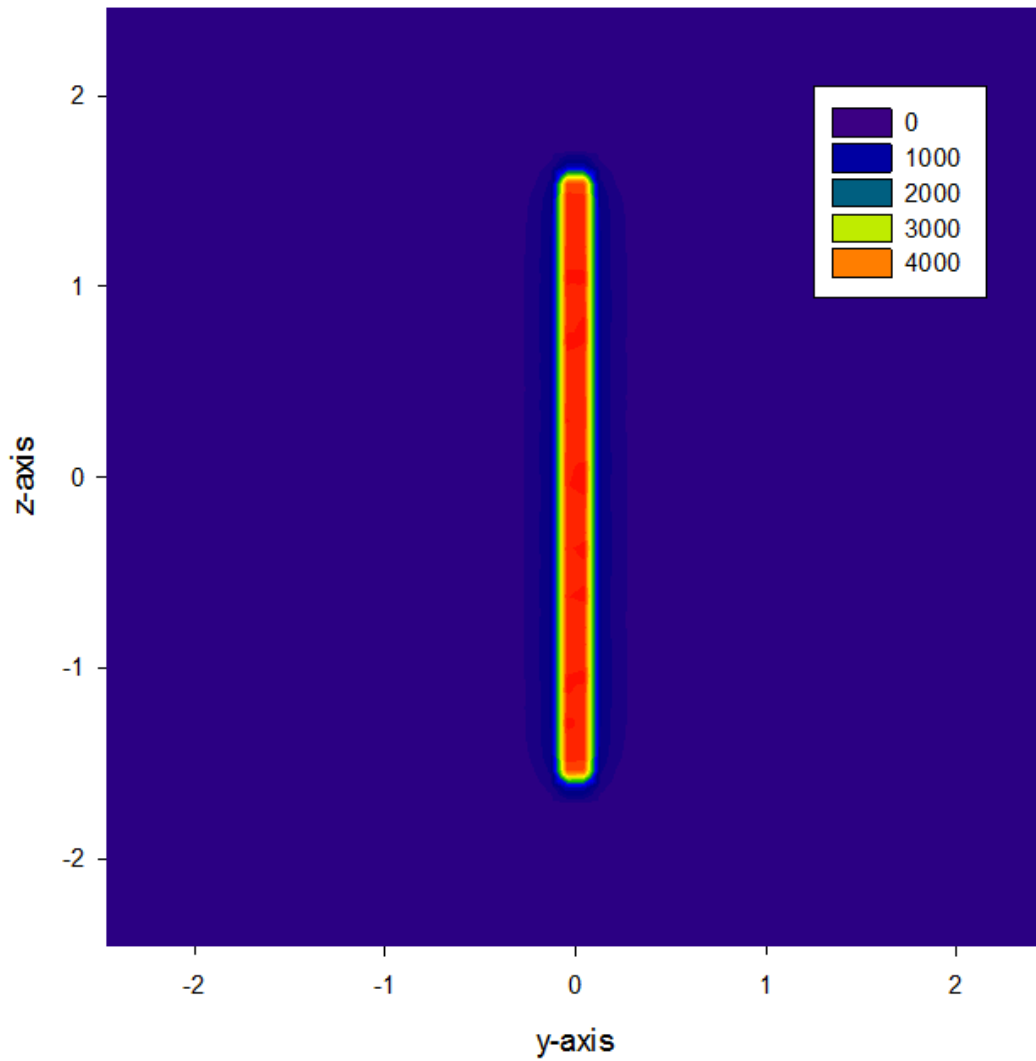


**Figure 4.21:** Monte Carlo Simulation (cGy) for a total of 70,000  $^{142}\text{Pr}$  glass microspheres in a glass capillary.

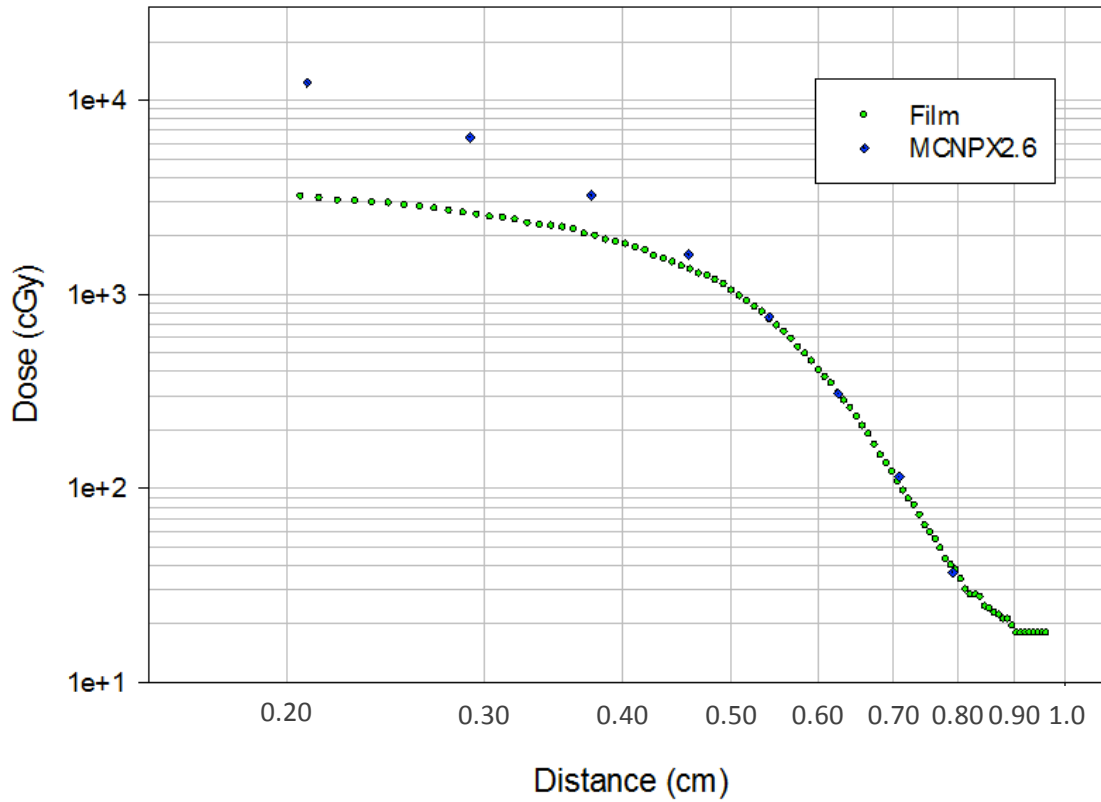


**Figure 4.22:** Monte Carlo and GAFCHROMIC<sup>®</sup> EBT2 film measurements for the <sup>142</sup>Pr glass microspheres. Discrepancies for higher doses in MCNPX2.6 when compared to the measurements are due to the lack of film sensitivity in the red channel (above 1000 cGy).

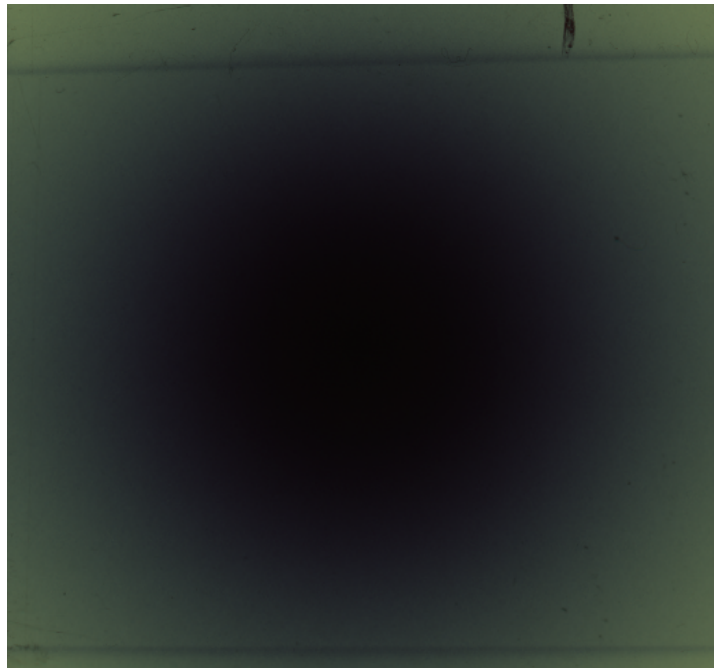
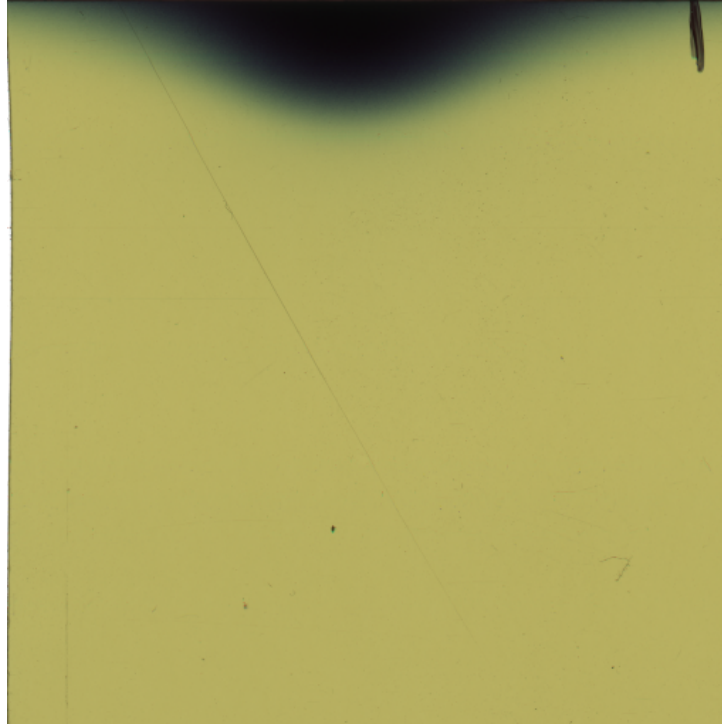


**Figure 4.23:** Axial and transversal GAFCHROMIC<sup>®</sup> EBT2 film measurement of  $^{142}\text{Pr}$  glass rod.

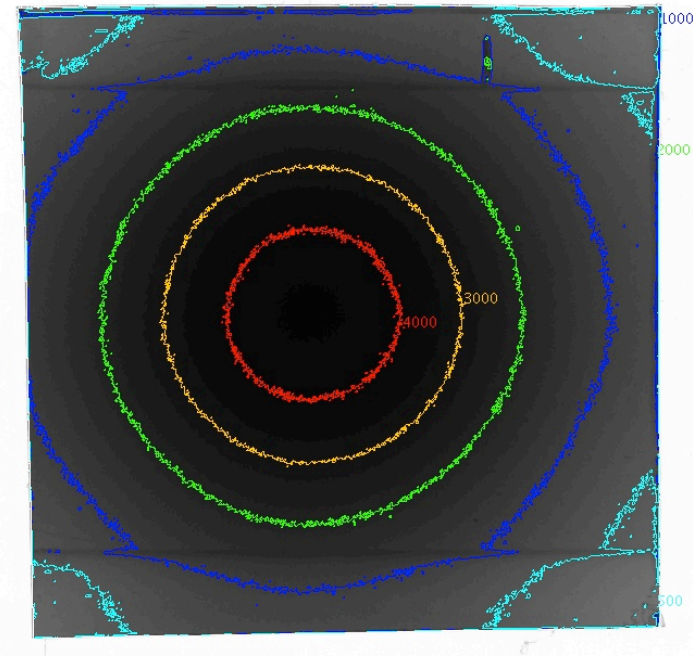
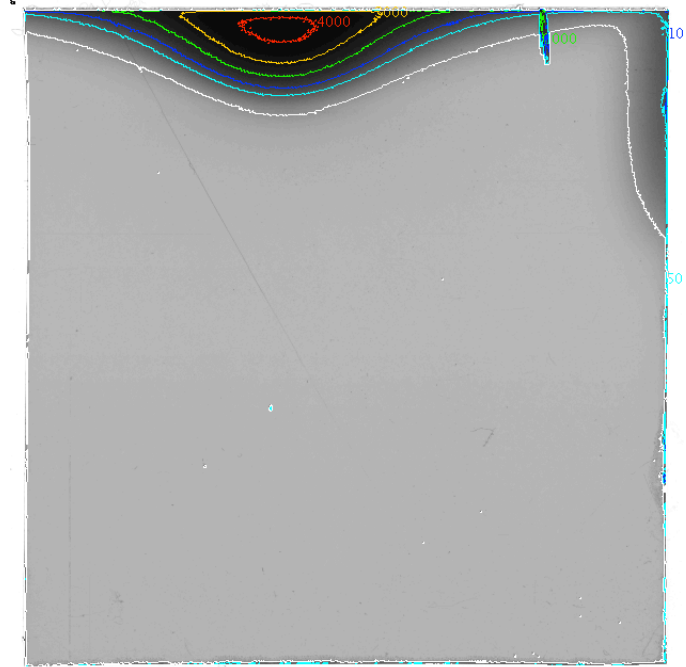


**Figure 4.24:** Isodose lines (cGy) for the glass rods dose measurements in GAFCHROMIC<sup>®</sup> EBT2 film (red channel converted to a 16-bit image).

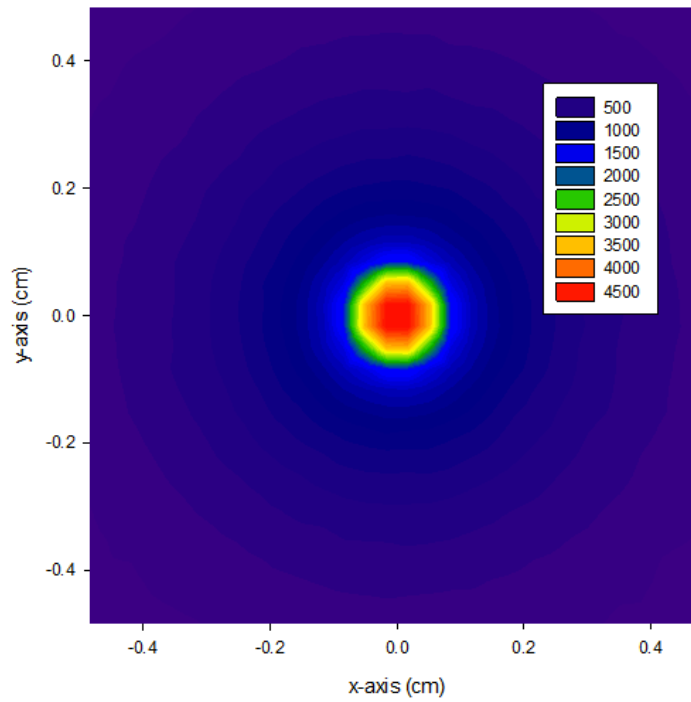
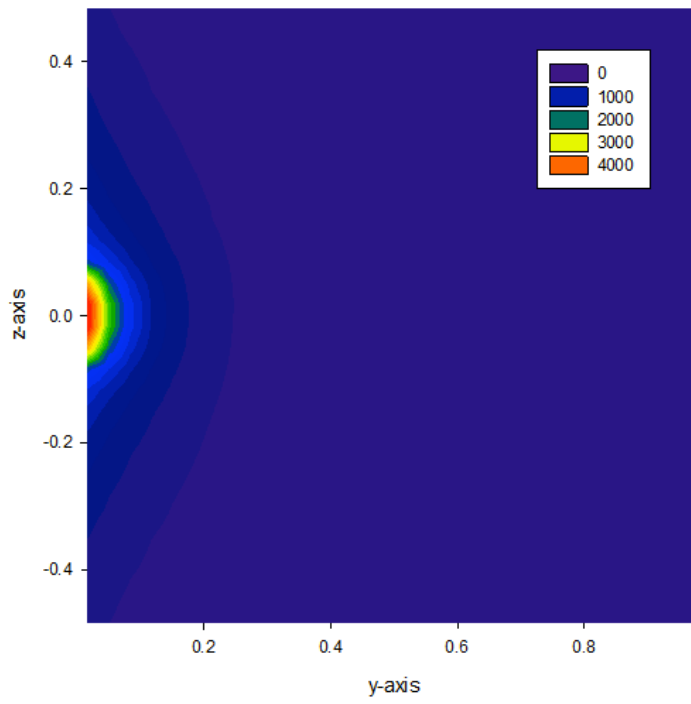


**Figure 4.25:** Monte Carlo Simulation (cGy) for a total of decays of a  $^{142}\text{Pr}$  glass rod

#### 4.4 Monte Carlo and Experimental Uncertainties Considerations

The number of histories used in MCNPX2.6 Monte Carlo simulations was great enough to guarantee less than 1.5% uncertainty associated with the energy deposition. Number of histories varied from  $1 \times 10^5$  to  $1 \times 10^7$ , depending on the distances considered and particle used (photons or electrons). For the measurements of dose deposited in film, uncertainties regarding the activity, time, and sample positioning were analyzed. For the sample activity values, uncertainties related to the sample total mass, irradiated time and shipping time were estimated in  $\pm 5\%$ ,  $\pm 1\%$  and  $\pm 6\%$  respectively. For the sample handling and placement in the phantom, it was estimated an uncertainty of  $\pm 1\%$ . During the measurements the glass capillary inside the water phantom remained in place. However, displacements were observed in the position of the rods that were in air in relation to the film positioning. These variations in positioning were estimated as being  $\pm 5\%$ . Considering that the dose deposited in the film were a function of total time, initial activity and sample positioning, the sensitivity analysis of the dose is given by:

$$\frac{\delta D}{D} = \frac{D[(t + \delta t), (a + \delta a), (p + \delta p)] - D[t, a, p]}{D[t, a, p]} \quad \text{Eq. 4.1}$$

where  $D$  is the dose,  $t$  is the time,  $a$  is the activity and  $p$  is the position and their respective uncertainties are represented by the delta. Estimated uncertainty in the dose was calculated as being  $\pm 11\%$ .

## CHAPTER 5: DISCUSSIONS & CONCLUSIONS

In this work, a dosimetric study for microsphere brachytherapy and conformal eye brachytherapy device was performed. Praseodymium-142 glass microspheres and glass rods were activated and dose measurements were performed using GAFCHROMIC<sup>®</sup> EBT2 film. A realistic dose distribution of microspheres in a single blood vessel was modeled and experiments were performed using a glass micro capillary filled with <sup>142</sup>Pr glass microspheres solution. Dose to different distances from the source as well as external exposures were calculated. Experiments were performed with <sup>142</sup>Pr microspheres using radiochromic film in a Solid Water<sup>®</sup> plastic phantom to validate the simulations. A more realistic dose distribution of microspheres in a single blood vessel was investigated. Measurements with activated <sup>142</sup>Pr microspheres in a glass microcapillary using EBT2<sup>®</sup> radiochromic film was performed and compared with the simulated dose. This work presented a detailed dosimetric study of <sup>142</sup>Pr microsphere, providing both simulation and experimental validation for the simulations, as well as biological effective dose calculations. It was shown that <sup>142</sup>Pr is a possible choice of radionuclide for treating Hepatocellular Carcinoma. This opens possibilities for animal studies by further research groups or private companies interested in manufacturing <sup>142</sup>Pr glass microspheres as well as performing clinical trials. For the CEBT device, <sup>142</sup>Pr glass rods showed to be a good candidate for applications in HDR eye brachytherapy, delivering highly target doses to the eye surface restricted to shallow depths. This opens possibilities of applications of this device in other superficial malignancies, such as skin cancer.

The activation of <sup>142</sup>Pr can be achieved in a low neutron fluence reactor. Some concern could be raised, regarding radioactive contamination due to the other components besides the

$^{142}\text{Pr}$ . During the neutron activation process, three of the  $^{142}\text{Pr}$  REAS glass components (Si and Al, and Pr) are activated in the reactor. However,  $^{28}\text{Al}$  has only 2.24 min half-life,  $^{31}\text{Si}$  has 2.62 h half-life with a small yield of gamma rays (0.07%), and the production of  $^{143}\text{Pr}$  with 13.57 d half-life is negligibly small during activation ( $1.2 \times 10^{-6}$ ). Energy spectrum of activated  $^{142}\text{Pr}$  glass samples was measured, confirming that impurities are not a concern in the activation of this nuclide.

### 5.1 $^{142}\text{Pr}$ Microsphere Brachytherapy

Microsphere brachytherapy for the treatment of hepatic malignancies using  $^{142}\text{Pr}$  is an alternative possibility in addition to the current used radionuclide  $^{90}\text{Y}$ , especially for rapid growing tumors with high doubling times.  $^{142}\text{Pr}$  microspheres can be easily activated in a low neutron flux reactor such as 1 Megawatt TRIGA (Training, Research, Isotopes, and General Atomics) reactor or may be activated in larger research reactors such as the 10 MW MURR<sup>®</sup>. These reactors are found in several research centers, making it widely available and possibly reducing total treatment costs for microsphere brachytherapy of the liver due to the proximity of the activation to the treatment site. Gamma emitting impurities generated during the activation process are expected to be negligible and therefore are not of concern regarding additional dose to the patient and staff. However, precaution should be taken during production of microspheres to avoid additional impurities. The gamma component of  $^{142}\text{Pr}$  would potentially allow a direct verification of the sample activity, using NaI detector, as well as excellent control of possible contaminations, by using a survey meter.

The time to deliver 90% of the dose ( $T_{90}$ ) for  $^{142}\text{Pr}$  is approximately 30% of  $T_{90}$  for  $^{90}\text{Y}$ . This is one advantage of using  $^{142}\text{Pr}$  over  $^{90}\text{Y}$ , since the longer the time to deliver the dose, the

higher is the risk of dose to healthy tissue due to migration to adjacent organs (especially to lungs) (Kennedy et al., 2007). A second advantage is that shorter half-lives are preferred due to the higher BED to the HCC. Considering and the additional dose to normal tissues,  $^{142}\text{Pr}$  microspheres would be more beneficial to the patients with less expected shunting from pretreatment  $^{99\text{m}}\text{Tc}$  scan.

Physical dose distributions and penetration ranges due to  $^{142}\text{Pr}$  were comparable to the ones of the currently used radionuclide  $^{90}\text{Y}$ . Point sources, as well as an ensemble of microspheres, were analyzed and point source data could be used to access the physical dose delivered to the patient. Ambient dose rates and total dose per a vial were calculated for  $^{142}\text{Pr}$  gamma component in order to estimate the radiation safety risks presented by this nuclide. Ambient dose rates and total dose were found to be 0.081 mSv/hr and 2.24 mSv, respectively which are below the exposure limits at one meter from the source. Based on the 10 CFR 35 (U.S. Nuclear Regulatory Commission, 2007), occupational exposure (50 mSv) and exposure of public limits (5 mSv if infrequent) per year should be observed. Radiation levels to the public and staff should be kept as low as reasonably achievable (ALARA). Therefore additional precaution may be necessary, such as avoiding proximity with the patient by the caregivers and family within the first few days after treatment.

The models used in the study of  $^{142}\text{Pr}$  were based in uniform distribution of activity inside tumors and blood vessels. The blood vessel located at the tumor periphery is a more realistic model for the microsphere distribution in the liver, but still considers a uniform distribution of radioactivity. Other uniform distribution studies have been proposed in the literature for  $^{90}\text{Y}$  dose distribution, e.g. partition models, in which the tumor and liver are subdivided into small voxels,

containing uniform activities (Ho et al., 1996). In addition, models using uniform distribution of activities have been used in imaging studies in an attempt to improve the assessment of the dose delivered to the patient (Rong et al., 2012). Tumor and liver sizes and shapes can vary significantly from one patient to another (Sarfaraz et al., 2004). For a more detailed dose distribution in a particular patient, a CT scan of the patient would be necessary, followed by a SPECT-CT image after dose administration to measure the actual bremsstrahlung distribution. Uniform distribution within voxels for patient specific dose determination was successfully used by Sarfaraz et al. (2004) to describe the dose distribution in the tumor and adjacent organs, such as the kidneys and stomach. The reverse technique, using the  $^{142}\text{Pr}$  dose distribution for a point source or a voxel, can be used for treatment planning purposes. This opens possibilities for a future route of this work, possibly starting phantom measurements and animal trials prior to future clinical trial.

Blood vessels uniformly filled with  $^{142}\text{Pr}$  and  $^{90}\text{Y}$  microspheres were modeled and simulated using a Monte Carlo code. Analysis of the dose distribution due to a single embolized blood vessel leads to a more realistic estimation of how microspheres are deposited in the tumor. Characterization of high physical and biological effective doses constrained to short distances, such as obtained from a single blood vessel, may be useful to the current studies being performed on the bystander effect, observed for highly localized doses (Dewhirst et al., 2012).

Post treatment biodistribution of the  $^{90}\text{Y}$  glass microspheres and dose distribution has been assessed through the detection of Bremsstrahlung photons produced by the beta particles (Rault et al., 2010; Poorbaygi et al., 2011) and scarce signal from positron emission (Gates et al., 2010). The low energy bremsstrahlung photons are highly scattered in the tissue, leading to a

poor spatial resolution of the dose distribution due to the very low signal (Rong et al., 2012). One of the issues with using SPECT for measurement of bremsstrahlung from  $^{90}\text{Y}$  is determining directionality (Rahmim and Zaidi, 2008), which can be improved with the use of pinhole cameras. The range of travel in PET is a limiting factor in the spatial resolution. In the attempt to improve resolution, PET has been proposed in conjunction with CT imaging for the optimization of  $^{90}\text{Y}$  processing (Hsiang et al., 2011). Recently the administration of a gamma emitter (e.g. Lutetium-177) concurrent with  $^{90}\text{Y}$  has been proposed to overcome issues related to the imaging resolution (Poorbaygi et al., 2011). The intrinsic gamma yield of  $^{142}\text{Pr}$  allows for potential post treatment imaging (Pelletier and Jung, 2012). Low dose rate mono-energetic photon could be detected using conventional detectors (i.e. NaI scintillation detector) for activity verification before treatment, while delivering a very low dose to the patient.  $^{142}\text{Pr}$  could be imaged with 1.58 MeV gamma photons. As the photon signal is strong enough from this isotope, Xenon detectors could be used to image the microspheres (Keller et al., 2002). Using good filtration and septa to reduce the inter-detector noise, the 1.58 MeV photon would allow for accurate imaging of the microspheres, with the additional benefit of the strong signal relative to  $^{142}\text{Pr}$  after passing through the body. The detection of high-energy gamma detection is still challenging because of more Compton scattering and needs further investigation.

### **5.1.1 Future work**

Future work in  $^{142}\text{Pr}$  microsphere brachytherapy includes the study of imaging techniques to detect microspheres post treatment and assessment of the dose delivered. Also important is the study and development of a standardized technique to measure the vial activities using gamma

detectors. Animal studies may be done prior to the implementation of  $^{142}\text{Pr}$  glass microspheres for clinical purposes.

## **5.2 Conformal Eye Brachytherapy Device**

This work purposed a preliminary dosimetric study of glass  $^{142}\text{Pr}$  and its possible applications in eye brachytherapy. Furthermore, it was intended to propose a novel design to the current eye plaque brachytherapy, capable of greater dose conformality in the tumor. However, further studies have to be done on the conformal eye brachytherapy (CEBT) device. The future steps will be followed by a patent application.

The conformal eye brachytherapy (CEBT) device would allow for the treatment of a tumor based on its shape and depth, providing a more conformal dose to the target. The preliminary simulation studies using the beta emitter  $^{142}\text{Pr}$  showed a short penetration depth and strong localization of the dose deposited to shallow regions, making this device suitable for treating superficial lesions, while sparing healthy tissues. This is proposed specifically for eye tumors, however, based on its geometry and physical properties, its use may be suitable for treating other types of superficial tumor, such as melanomas and squamous cell carcinomas.

Glass eye plaque using Re-188, Pr-142, and Y-90 are viable for the treatment of superficial eye cancers, due to the high doses achieved in short distances, sparing healthy surrounding issues. Glass eye plaques could also be further molded according to the tumor shape and size to achieve the desired dose distribution. The feasibility and costs of each of these radionuclides should be taken into account for each clinical setup configuration, time from the nuclide activation to dose delivery, and desired dose penetration in tissue.

### 5.2.1 Patent application and Future Work

This research project proposes to develop a novel conformal brachytherapy device using the beta- minus emitters to treat superficial human eye tumors and malignancies.. The proposed technique is especially designed to benefit numerous patients suffering from eye cancer in the US and in the world. In the future, this innovative device may have its use extended to treat other forms of superficial cancer, e.g. melanomas, basal and squamous cell carcinoma and body parts of difficult access as mentioned before.

It is intended to fully design and finalize the patent for the  $^{142}\text{Pr}$  CEBT device prior to seeking a scientific partnership for physically developing the conformal eye brachytherapy design. Costs may be elevated, especially for the initial price of fully developing this device. It is intended to: (1) fabricate the  $^{142}\text{Pr}$  CEBT device, having a digital remote controller and shielding case, (2) develop a software to calculate the rods positioning and temporal sequence to produce the desired dose, (3) to design a solid water phantom to simulate the eyeball, (4) to measure dose delivered using a NaI array detectors, (5) to perform animal tests prior to the clinical implementation of the device.

For the  $^{142}\text{Pr}$  CEBT device, customized rare earth aluminum silicate (REAS) glass rods of cylindrical geometry with flat ends may be custom ordered from the manufacturer. A digital controlling system would allow manipulating the device and radioactive rods from the outside of the treatment room, minimizing dose to the staff. A patent application is in process and in the future, collaboration with private companies will allow developing an accurate digital controller. A Plexiglas shield, for handling the device, can be used and radial and depth dose measurement can be done using RADIOCHROMIC<sup>®</sup> film. It is intended to perform future animal tests or

clinic tests of the novel CEBT device developed in this research.

### *Planning and delivering the planned dose*

A planning system to customize the radiation fields for a given tumor may be developed for the CEBT device. The planning of dose delivered can be done based on the tumor geometry and prescribed dose. Ultrasound imaging of the tumor (Char et al., 2002) may be used to access the depth and tumor extent within the eyeball. Dose delivery and rod positioning may be guided in real time by using a high-resolution medical camera. After total dose is prescribed and the planning target volume (PTV) contoured the treatment fields will be optimized using computer software. For the treatment delivery, patient specific quality assurance should be performed, and total planned dose should be verified prior to the actual treatment. After verification and proper consideration of the radionuclide decay, the applicator is positioned and the planned treatment can be delivered.

### *Quality Assurance Methods Proposed for the CEBT*

Development of a quality assurance method for verification of the device and planning is necessary to ensure that the correct dose is delivered to the site. Due to the size of the device and the fact that  $^{142}\text{Pr}$  presents a 3.7% gamma yield, the most appropriate method for quality assurance (QA) would be an array of HPGe or NaI detectors. This array could be made with the same number of detectors as rods in the treatment device, allowing the required spatial resolution. Computer based program will generate the corresponding 2D dose distribution to be compared with measurements. Well- established methods such as the distance to agreement (DTA) could be used to verify the passing rate of the fields delivered.

## REFERENCES

Almond PR, Biggs PJ, Coursey BM, Hanson WF, Huq MS, Nath R, Rogers DW. "AAPM's TG-51 protocol for clinical reference dosimetry of high-energy photon and electron beams." *Medical Physics* **26**:1847-70 (1999)

<http://www.cancer.org/acs/groups/cid/documents/webcontent/003100-pdf.pdf> American Cancer Society, Eye Cancer (Melanoma and Lymphoma) Overview, (2012)

<http://www.cancer.org/acs/groups/cid/documents/webcontent/003058-pdf.pdf> American Cancer Society, Liver Cancer Overview, (2013)

Antipas V, Dale RG, Coles IP "A theoretical investigation into the role of tumour radiosensitivity, clonogen repopulation, tumour shrinkage and radionuclide RBE in permanent brachytherapy implants of  $^{125}\text{I}$  and  $^{103}\text{Pd}$ ." *Physics in Medicine and Biology* **46**:2557-69 (2001)

Arjomandy B, Tailor R, Anand A, Sahoo N, Gillin M, Prado K, Vicic M, "Energy dependence and dose response of Gafchromic EBT2 film over a wide range of photon, electron, and proton beam energies." *Medical Physics* **37**: 1942-7 (2010)

Armpilia, CI, Dale, RG, Coles, IP, Jones, B, and Antipas, V, "The determination of radiobiologically optimized half-lives for radionuclides used in permanent brachytherapy implants," *International Journal of Radiation Oncology, Biology, Physics* **55**:378-85 (2003)

Bakht, MK, and Sadeghi, M, "Internal radiotherapy techniques using radiolanthanide praseodymium-142: a review of production routes, brachytherapy, unsealed source therapy," *Annals of Nuclear Medicine* (2011)

Berger MJ, "Distribution of absorbed dose around point sources of electrons and beta particles in water and other media." *Journal of Nuclear Medicine* **5**:5-23 (1971)

Bianciotto C, Shields, CL, Lally SE, Freire J, Shields JA, "CyberKnife Radiosurgery for the Treatment of Intraocular and Periocular Lymphoma" ARCH OPHTHALMOLOGY **128** (NO. 12), (2010)

Char, DH, Kundert, G, Bove, R, Crawford, JB, "20 MHz high frequency ultrasound assessment of scleral and intraocular conjunctival squamous cell carcinoma", British Journal of Ophthalmology **86**:632-635 (2002)

Chiu-Tsao ST, Astrahan MA, Finger PT, Followill DS, Meigooni AS, Melhus CS, Mourtada F, Napolitano ME, Nath R, Rivard MJ, Rogers DW, Thomson RM. "Dosimetry of (125)I and (103)Pd COMS eye plaques for intraocular tumors: report of Task Group 129 by the AAPM and ABS." Medical Physics **39**:6161-84 (2012)

Conzone SD, Häfeli UO, Day DE, Ehrhardt GJ. "Preparation and properties of radioactive rhenium glass microspheres intended for in vivo radioembolization therapy." Journal of Biomedical Materials Research **42**:617-25 (1998)

Council Steering Committee, "ACR – ASTRO – SIR PRACTICE GUIDELINE FOR RADIOEMBOLIZATION WITH MICROSPHERE BRACHYTHERAPY DEVICE (RMBD) FOR TREATMENT OF LIVER MALIGNANCIES", Chemotherapy 1-14 (2008)

Coursey BM, and Nath R. "Radionuclide Therapy" Physics Today **53** 25 April (2000)

Cremonesi M, Ferrari M, Bartolomei M, Orsi F, Bonomo G, Aricò D, Mallia A, De Cicco C, Pedrolì G, and Paganelli G, "Radioembolisation with <sup>90</sup>Y-microspheres: dosimetric and radiobiological investigation for multi-cycle treatment." European Journal of Nuclear Medicine and Molecular Imaging **35**:2088-96 (2008)

Cross, WG, Ing H, and Freedman N, "A short atlas of beta-ray spectra" Physics Medicine and Biology **28** (1983)

Dauffy L, "Calculation of dose to soft tissue from implanted beta sources" A thesis for Master of Science, Texas A&M University, College Station, Texas (1998)

Devic, S, "Radiochromic film dosimetry: Past, present, and future" *Physica Medica* **27**, 122-134 (2011)

Dezarn WA, Cessna JT, DeWerd LA, Feng W, Gates VL, Halama J, Kennedy AS, Nag S, Sarfaraz M, Sehgal V, Selwyn R, Stabin MG, Thomadsen BR, Williams LE, and Salem R, "Recommendations of the American Association of Physicists in Medicine on dosimetry, imaging, and quality assurance procedures for  $^{90}\text{Y}$  microsphere brachytherapy in the treatment of hepatic malignancies," *Medical Physics* **38**:4824 (2011)

Dezarn WA, Kennedy AS. "Resin  $^{90}\text{Y}$  microsphere activity measurements for liver brachytherapy." *Med Phys.* **34**:1896-1900 (2007)

Fischer M, Kampen WU, "Radionuclide Therapy of Bone Metastases." *Breast Care* **7** (2): 100-107. Epub (2012)

Fowler JF. "The linear-quadratic formula and progress in fractionated radiotherapy." *The British Journal of Radiology* **62**:679 (1989)

Fox RA, Klemp PF, Egan G, Mina LL, Burton MA, Gray BN, "Dose distribution following selective internal radiation therapy." *International Journal Radiation Oncology Biology Physics* **21** 463-7 (1991)

Gagne NL, Leonard KL, Huber KE, Mignano JE, Duker JS, Laver NV, Rivard MJ, "BEDVH-A method for evaluating biologically effective dose volume histograms: application to eye plaque brachytherapy implants." *Medical Physics* **39** 976-83 (2012)

Gates VL, Esmail AA, Marshall K, Spies S, Salem R, "Internal pair production of  $^{90}\text{Y}$  permits hepatic localization of microspheres using routine PET: proof of concept" *Journal of Nuclear Medicine* **52**:72-6 (2011)

Gerbi BJ, Antolak JA, Deibel FC, Followill DS, Herman MG, Higgins PD, Huq MS, Mihailidis DN, Yorke ED, Hogstrom KR, Khan FM. "Recommendations for clinical electron beam

dosimetry: supplement to the recommendations of Task Group 25” *Medical Physics* **36**:3239-3279 (2009)

Guimarães CC, Moralles M, Sene FF, and Martinelli JR, "Dose-rate distribution of  $^{32}\text{P}$ -glass microspheres for intra-arterial brachytherapy," *Medical Physics* **37**, 532 (2010)

Häfel U, “Review: Radioactive Microspheres for Medical Applications” *Journal of Radiology* [www.jradiology.org](http://www.jradiology.org) (2001)

Hall EJ, *Radiobiology for the Radiologist*, Lippincott, Philadelphia, PA (2000)

Hall EJ and Brenner DJ. “The dose-rate effect in interstitial brachytherapy: a controversy resolved.” *British Journal of Radiology* **65**:242-247 (1992)

Hamoudeh M, Kamleh MA, Diab R, and Fessi H, "Radionuclides delivery systems for nuclear imaging and radiotherapy of cancer" *Advanced Drug Delivery Reviews* **60**:1329-46 (2008)

Hennequin C, Quero L, Rivera S, “Radiosensitivity of hepatocellular carcinoma” *Cancer/Radiothérapie* **15**:39-42 (2011)

Ho S, Lau WY, Leung TWT, Chan M, Ngar YK, Johnson PJ, and Li AKC, "Partition model for estimating radiation doses from yttrium-90 microspheres in treating hepatic tumours," *European Journal of Nuclear Medicine* **23** (1996)

Hsiang KY, Jeffrey S, Jianhua Y, David WT, Somanesan S, Soon Y, Gabriel KYL, Pierce KHC, Andrew EHT, David CEN, Anthony SWG, “Optimization of yttrium-90 processing on a clinical PET/CT system.” *Nuclear Science Symposium and Medical Imaging Conference (NSS/MIC)*, IEEE 23-29 (2011)

International Commission on Radiation Units and Measurements//ICRU Report 38 “Dose and Volume Specification for Reporting Intracavitary Therapy in Gynecology (Report 38).” (1985)

Jävinen H, Cross WG, Soares C, Vynckier S, Weaver K, ICRU (The International Commission on Radiation Units and Measurements) Report No. 72: Dosimetry of Beta Rays and Low Energy Photons for Brachytherapy with Sealed Sources, Oxford University Press, Journal of the ICRU Volume 4 No. 2 (2004)

Johnson LS, Yanch JC, Shortkroff S, Barnes CL, Spitzer AI, and Sledge CB. "Beta-particle dosimetry in radiation synovectomy." *European Journal of Nuclear Medicine* **22**:977-988 (1995)

Jung JW, Reece WD, "Determination of feasibility and prescribed dose for  $^{142}\text{Pr}$  glass seeds for prostate cancer brachytherapy", *Medical Physics* **34**:2434 (2007)

Jung JW, and Reece WD, "Dosimetric characterization of  $^{142}\text{Pr}$  glass seeds for brachytherapy," *Applied Radiation and Isotopes: Including Data, Instrumentation and Methods for Use in Agriculture, Industry and Medicine* **66**:441-9 (2008)

Jung JW, "Pr GLASS SEEDS FOR THE BRACHYTHERAPY OF PROSTATE CANCER Pr GLASS SEEDS" A Ph.D. Dissertation, Technology Texas A&M University, College Station, Texas (2007)

Kairn T, Aland T, "Calibration of Radiochromic Film for Electron Radiotherapy Dosimetry," *World Congress on Medical Physics and Biomedical Engineering May 26-31, 2012, Beijing, China IFMBE Proceedings* **39**:1153-1156 (2013)

Katz L, and Penfold AS, "Range-Energy Relations for Electrons and the Determination of Beta-Ray End-Point Energies by Absorption." *Review of Modern Physics* **24**:28-44 (1952)

Keller H, Glass M, Hinderer R, Ruchala K, Jeraj R, Olivera G, and Mackie TR. "Monte Carlo study of a highly efficient gas ionization detector for megavoltage imaging and image-guided radiotherapy" *Medical Physics* **29**:165 (2002)

Kennedy AS, Coldwell D, Nutting C, Murthy R, Wertman DE Jr, Loehr SP, Overton C, Meranze S, Niedzwiecki J, Sailer S. "Resin <sup>90</sup>Y-microsphere brachytherapy for unresectable colorectal liver metastases: modern USA experience." *International Journal of Radiation Oncology, Biology, Physics* **65**:412-25 (2006)

Kennedy AS, Lodge MA, and Li XA, "Radiation absorbed dose distribution in a patient treated with yttrium-90 microspheres for hepatocellular carcinoma." 2449-2453 (2004)

Kennedy AS, Nag S, Salem R, Murthy R, McEwan AJ, Nutting C, Benson A, Espat J, Bilbao JI, Sharma RA, Thomas JP, and Coldwell D, "Recommendations for radioembolization of hepatic malignancies using yttrium-90 microsphere brachytherapy: a consensus panel report from the radioembolization brachytherapy oncology consortium." *International Journal of Radiation Oncology, Biology, Physics* **68**:13-23 (2007)

Kennedy AS, Nutting C, Coldwell D, Gaiser J, Drachenberg C., "Pathologic response and microdosimetry of <sup>90</sup>Y microspheres in man: review of four explanted whole livers." *International Journal of Radiation Oncology, Biology and Physics* **60**:1552–1563 (2004)

Kinsey RR. National Nuclear Data Center: Nuclear Data from NuDat at Brookhaven National Laboratory [<http://www.nndc.bnl.gov/nndc/nudat/>] (1998)

Kumar R, Sharma SD, Deshpande S, Ghadi Y, Shaiju VS, Amols HI, Mayya YS. "Acrylonitrile Butadiene Styrene (ABS) plastic based low cost tissue equivalent phantom for verification dosimetry in IMRT." *Journal of Applied Clinical Medical Physics/American College of Medical Physics* **11**:3030 (2009)

Lea DE, Catcheside DG, "The mechanism of the induction by radiation of chromosome aberrations in *Tradescantia*." *Journal of Genetics* **44**:216-245 (1942)

Lea DE, *Actions of Radiations on Living Cells*, Cambridge Univ. Press, Cambridge, (1947)

Lee SW and Reece WD, "Dose calculation of  $^{142}\text{Pr}$  microspheres as a potential treatment for arteriovenous malformations," *Physics in Medicine and Biology* **50**:151-166 (2005)

McShan DL, Kessler ML, Fraass BA. "Advanced interactive planning techniques for conformal therapy: high level beam descriptions and volumetric mapping techniques." *International Journal of Radiation Oncology, Biology, Physics* **33**:1061-72 (1995)

Mehrara E, Forssell-Aronsson E, Ahlman H, and Bernhardt P, "Specific Growth Rate versus Doubling Time for Quantitative Characterization of Tumor Growth Rate." *Cancer Research* **67**:8 (2007)

Nag S, Quivey JM, Earle JD, Followill D, Fontanesi J, Finger PT, "ABS recommendations for brachytherapy of uveal melanomas", *International Journal of Radiation Oncology, Biology, Physics* **56**, 544-555 (2003)

Nath R, Anderson LL, Meli JA, Olch AJ, Stitt JA, Williamson JF. "Code of practice for brachytherapy physics: report of the AAPM Radiation Therapy Committee Task Group No. 56." *American Association of Physicists in Medicine, Medical Physics* **24**:1557-98 (1997)

Nedaie HA, Mosleh-Shirazi MA, Gharaati H, Shariari M, Allahverdi M. "Assessment of different MCNP Monte Carlo codes in electron absorbed dose" *Reports of Practical Oncology & Radiotherapy* **11**:293-298 (2006)

Oehme L, Kotzerke J. "Radiobiological considerations for radioembolization with  $^{188}\text{Re}$ -microspheres" *European Journal of Nuclear Medicine and Molecular Imaging* **36** 322-325 (2009)

Pelletier CD, Jung JW. Study of imaging  $^{142}\text{Pr}$  microspheres using the gamma emission spectrum in a clinical setting. *IEEE 2012 Nuclear Science Symposium, Medical Imaging Conference, Anaheim, CA; Oct 29-Nov 3* (2012)

Poorbaygi H, Aghamiri SMR, Sheibani S, Kamali-Asl A, and Mohagheghpoor E, "Production of glass microspheres comprising  $(90)\text{Y}$  and  $(177)\text{Lu}$  for treating of hepatic tumors with SPECT

imaging capabilities," *Applied Radiation and Isotopes: Including Data, Instrumentation and Methods for Use in Agriculture, Industry and Medicine* **69**:1407-14 (2011)

Rahmim A, Zaidi H. "PET versus SPECT: strengths, limitations and challenges." *Nuclear Medicine Communications* **29**:193-207 (2008)

Reece WD, Miller SD, Durham JS, "SADDE (Scaled Absorbed Dose Distribution Evaluator): a code to generate input for VARSKIN" Washington, DC: Division of Accident Evaluation, Office of Nuclear Regulatory Research, U.S. Nuclear Regulatory Commission (1989)

Reynaert N, Palmans H, Thierens H, and Jeraj R, "Parameter dependence of the MCNP electron transport in determining dose distributions," *Medical Physics* **29**:2446-2454 (2002)

Rault E, Staelens S, Van Hoken R, De Beenhouwer J, and Vandenberghe S, "Fast simulation of yttrium-90 bremsstrahlung photons with GATE," *Medical Physics* **37**:2943 (2010)

Rong X, Du Y, Frey EC, Ljungberg M, Rault E, Vandenberghe S, "Development and evaluation of an improved quantitative <sup>90</sup>Y bremsstrahlung SPECT method," *Medical Physics* **39** 2346 (2012)

Rösler H, Triller J, Baer HU, Geiger L, Beer HF, Becker C, and Blumgart LH. "Superselective radioembolization of hepatocellular carcinoma: 5-year results of a prospective study." *Nuclear Medicine* **33**:206-214 (1994)

Sadeghi M, Bakht MK, and Mokhtari L, "Practicality of the cyclotron production of radiolanthanide <sup>142</sup>Pr: a potential for therapeutic applications and biodistribution studies," *Journal of Radioanalytical and Nuclear Chemistry* **288**:937-942 (2011)

Sadeghi M, Taghdiri F, Hosseini SH, Tenreiro C, "Monte Carlo calculated TG-60 dosimetry parameters for the beta-emitter <sup>153</sup>Sm brachytherapy source." *Medical Physics* **37**:5370-5 (2010)

Salem R and Thurston KG, "Radioembolization with yttrium-90 microspheres: a state-of-the-art brachytherapy treatment for primary and secondary liver malignancies: part 3: comprehensive literature review and future direction," *Journal of Vascular and Interventional Radiology : JVIR* **17**:1571-93 (2006)

Sarfaraz M, Kennedy AS, Cao ZJ, Sackett GD, Yu CX, Lodge MA, Murthy R, Line BR, and Van Echo DA. "Physical aspects of yttrium-90 microsphere therapy for nonresectable hepatic tumors," *Medical Physics* **30**:199 (2003)

Sarfaraz M, Kennedy AS, Lodge MA, Li XA, Wu X, and Yu CX, "Radiation absorbed dose distribution in a patient treated with yttrium-90 microspheres for hepatocellular carcinoma", *Medical Physics* **31**:2449-2453 (2004)

Sedda AF, Cipriani C, and Carrozzo A, "Dermatological single-session beta emitter conformational brachytherapy of non-melanocyte skin tumors," *Brachytherapy: Types, Dosing and Side Effects*, Nova Science Publishers, Ch. 4 (2011)

Schaart DR, Bos AJ, Winkelman AJ, Clarijs MC. "The radial depth-dose distribution of a 188W/188Re beta line source measured with novel, ultra-thin TLDs in a PMMA phantom: comparison with Monte Carlo simulations," *Physics in Medicine Biology* **47**:3605-27 (2002)

Smith T, Crawley JC, Shawe DJ, and Gumpel JM, "SPECT using Bremsstrahlung to quantify <sup>90</sup>Y uptake in Baker's cysts: its application in radiation synovectomy of the knee," *European Journal of Nuclear Medicine* **14**:498-503 (1988)

Spillane T, Raiola F, Zeng F, Becker HW, Gialanella L, Kettner KU, Kunze R, Rolfs C, Romano M, Schürmann D, Strieder F. "The <sup>198</sup>Au  $\beta$  half-life in the metal Au." *The European Physical Journal A* **31**:203-205 (2007)

Squair PL, Pozzo L, Ivanov E, Martinelli JR, Azevedo MBM, Osso Jr JA. "166Ho-microspheres as a promising radiopharmaceutical for therapy", *ALASBIMN Journal, XXVI Congresso Brasileiro de Medicina Nuclear* (2012)

Supe SJ, Mallikarjuna RS, Sawant SG, "Dosimetry of spherical Sr90-Y90 beta ray eye applicators," *The American Journal of Roentgenology, Radium Therapy, and Nuclear Medicine* **123**:36-41 (1975)

Traub RJ, et al. "Dose calculation for contamination of the skin using the computer code VARSKIN" Washington, DC: Division of Regulatory Applications, Office of Nuclear Regulatory Research, U.S. Nuclear Regulatory Commission (1987)

Thibault I, and Vigneault E, "High-Dose-Rate Interstitial Brachytherapy in the Management of Primary and Recurrent Gynaecologic Malignancies: Clinical Experience and Review of the Literature" *Brachytherapy: Types, Dosing and Side Effects*, Nova Science Publishers, Ch. 2, (2011)

Turner JH, Claringbold PG, Klemp PF, Cameron PJ, Martindale AA, Glancy RJ, Norman PE, Hetherington EL, Najdovski L, Lambrecht RM, "166Ho-microsphere liver radiotherapy: a preclinical SPECT dosimetry study in the pig." *Nuclear Medicine Communications* **15**:545-53 (1994)

Unger LM and Trubey DK, "Specific gamma-ray dose constants for nuclides important to dosimetry and radiological assessment" ORNL/RSIC-45 (1982)

U. S. Nuclear Regulatory Commission, "Code of Federal Regulations", 10 CFR Part 35.75, U. S. Government Printing Office, Washington DC (1997)

Vynckier S, and Wambersie A, "Dosimetry of beta sources in radiotherapy I. The beta point source dose function," *Physics in Medicine and Biology* **27**:1339-47 (1982)

X-5 Monte Carlo Team, MCNP-A General Monte Carlo N-Particle Transport Code, Version 5 - Vol. I: Overview and Theory, Los Alamos National Laboratory report LA-UR-03 (1987)

## APPENDIX A: MCNPX2.6 INPUTS

### A.1: Microsphere Brachytherapy Inputs:

#### A.1.1: Source homogeneously distributed model for spherical tumor

Beta dose at water due to homogeneously distributed microspheres within a 5.0 cm tumor

c Cell Cards

c Pr source

5 3 -1.0 -2 imp:p,e=1

c

900 3 -1.000 -6 #5

imp:p,e=4

c void

999 0 6 imp:p,e=0

c end of cell cards

c surface card

c surface of water

c radius of microsphere (10.0 cm diameter)

2 SO 5.0

6 SO 12.0

c end of surface cards

MODE p e

c material card

c Si:Al:Pr:O (weight percent)

m1 14000 -0.153 13000 -0.081 59000 -0.445 8000 -0.322

c water

c H : 2 O : 1

m3 001001 2 008016 1

SDEF cell=5 ERG=d1 rad=d2 PAR=3

SI1 A 0.017 0.172 0.265 0.395 0.574 0.766 0.877 0.946 1.026 1.188

1.268 1.343 1.615 1.712 1.884 1.923 2.011 2.064 2.104 2.139 2.160

SP1 D 586 656 673 669 649 632 613 598 578 527

497 464 311 244 121 95.2 43.4 19.8 7.32 1.19 0.0069

SI2 0 5.0

SP2 -21 2

c E0

c F8:P 10

c mesh tally

```
tmesh
c xz plane
  rmesh1:e pedep
  cora1 0.0 19i 6.0
  corb1 -0.30 0.30
  corc1 -0.30 0.30
endmd
NPS 2.0E6
PRDMP 1E7 1E8 0 4
DBCN 18J 1 $ITS-style energy indexing
PRINT
c PRINT -10 -40 -50 -70 -98 -85 -86 -110 -140 -170 -130 -128
```

**A.1.2: Cylindrical blood vessel model**

Beta dose at water

c BLOCK 1

c\*\*\*\*\*CellCards\*\*\*\*\*  
 \*\*\*\*\*

c  
 5 1 -4.0 -3 -2 imp:p,e=1 \$142-Pr source (cylindrical blood vessel inside tumor)  
 c 5 1 -3.29 -3 -2 imp:p,e=1 \$90-Y source (cylindrical blood vessel inside tumor)  
 100 3 -1.000 -2 #5 imp:p,e=1 \$Tumor (water, R=0.5, 1.0, and 1.5 cm)  
 900 3 -1.000 -6 #5 #100 imp:p,e=4 \$Outside medium (water, R=12.0cm)  
 999 0 6 imp:p,e=0 \$Void

c BLOCK 2

c\*\*\*\*\*SurfaceCards\*\*\*\*\*  
 \*\*\*\*\*

c  
 2 SO 0.5 \$Surface of tumor (R=0.5, 1.0, and 1.5 cm)  
 3 C/Z 0 0 0.0010 \$source/arteries (12-30um diameter, aver. r=10e-6m=10e-4cm)  
 6 SO 12.0 \$Surface of water/medium (12.0 cm radius)

c BLOCK 3

c\*\*\*\*\*DataCards\*\*\*\*\*  
 \*\*\*\*\*

c  
 MODE P E

c  
 c ----- Material Card -----

c  
 c \*\* Pr Glass \*\*  
 c Si:Al:Pr:O (weight percent)

c  
 M1 14000 -0.153 13000 -0.081 59000 -0.445 8000 -0.322

c  
 c \*\* Y Glass \*\*  
 c Si:Al:Y:O (weight percent)

c  
 c M1 14000 -0.194 13000 -0.106 39000 -0.303 8000 -0.397

c  
 c \*\* Water \*\*  
 c H:2 O:1 (atomic abundance)

c  
 M3 001001 2 008016 1

c  
 c ----- Source Definitions -----

c

```

c      SDEF: Cell 5; Tabulated Energies (A); Radial Distance; Electron;
c
SDEF POS 0 0 0 AXS=0 0 1 EXT=d2 RAD=d3 ERG=d1 PAR=3
c
c      ** 142-Praseodymium BETA ENERGY DISTRIBUTION **
c
c      ** use this energy distribution for 142-Praseodymium simulations **
c
SI1 A 0.017 0.172 0.265 0.395 0.574 0.766 0.877 0.946 1.026 1.188
1.268 1.343 1.615 1.712 1.884 1.923 2.011 2.064 2.104 2.139 2.160
SP1 D 586 656 673 669 649 632 613 598 578 527
497 464 311 244 121 95.2 43.4 19.8 7.32 1.19 0.0069
c
c      ** 90-Yttrium BETA ENERGY DISTRIBUTION **
c
c      ** use this energy distribution for 90-Yttrium simulations **
c
c SI1 A 0.1 0.2 0.3 0.4 0.5 0.6 0.7 0.8 0.9 1.0
c      1.1 1.2 1.3 1.4 1.5 1.6 1.7 1.8 1.9 2.0 2.1
c SP1 D 406.1 476.2 528.1 566.1 593.4 612.1 623.7 628.8 627.6 619.9
c      605.2 582.8 552.3 513.1 465.3 409.2 345.9 277.0 205.3 134.3 69.0
SI2 -0.5 0.5      $radial sampling range (set as same tumor radius)
SP2 -21 0      $uniform sampling for line
SI3 0 0.0010      $radial sampling range from 0 to Rmax (same as blood vessel)
SP3 -21 1      $radial sampling probability
c E0
c F8:P 10
c
c ----- Mesh Tally -----
c
tmesh
c xz plane
  rmesh1:e pedep
  cora1 -0.50 29i 0.50
  corb1 -0.50 29i 0.50
  corc1 -0.50 9i 0.50
endmd
NPS 2.0E7
PRDMP 1E7 1E8 0 4
DBCN 18J 1 $ITS-style energy indexing
PRINT
c PRINT -10 -40 -50 -70 -98 -85 -86 -110 -140 -170 -130 -128

```

### A.1.3 Glass Capillary filled with <sup>142</sup>Pr

Beta dose at water

c BLOCK 1

c \*\*\*\*\* Cell Cards \*\*\*\*\*

c

5 1 -4.0 -3 -11 12 imp:p,e=1 \$142-Pr source (cylindrical blood vessel inside tumor)

c 5 1 -3.29 -3 -2 imp:p,e=1 \$90-Y source (cylindrical blood vessel inside tumor)

10 4 -2.52 -4 -11 12 #5 imp:p,e=1 \$Glass capillary

c 100 3 -1.000 -2 #5 imp:p,e=1 \$Tumor (water, R=0.5, 1.0, and 1.5 cm)

900 3 -1.000 -6 #5 #10 imp:p,e=4 \$Outside medium (water, R=12.0cm)

999 0 6 imp:p,e=0 \$Void

c BLOCK 2

c \*\*\*\*\* Surface Cards \*\*\*\*\*

c

c 2 SO 0.5 \$Surface of tumor (R=0.5, 1.0, and 1.5 cm)

3 C/Z 0 0 0.0300 \$capillary glass internal diameter

4 C/Z 0 0 0.0450 \$capillary glass external diameter

11 PZ 1.5 \$capillary top

12 PZ -1.5 \$capillary bottom

6 SO 12.0 \$Surface of water/medium (12.0 cm radius)

c BLOCK 3

c \*\*\*\*\* Data Cards \*\*\*\*\*

c

MODE P E

c

c ----- Material Card -----

c

c \*\* Pr Glass \*\*

c Si:Al:Pr:O (weight percent)

c

M1 14000 -0.153 13000 -0.081 59000 -0.445 8000 -0.322

c

c

c \*\* Y Glass \*\*

c Si:Al:Y:O (weight percent)

c

c M1 14000 -0.194 13000 -0.106 39000 -0.303 8000 -0.397

c

c

c \*\* Water \*\*

c H:2 O:1 (atomic abundance)

c

M3 001001 2 008016 1

```

c
c
c          ** Glass (Capillary Walls)**
c          Si:Al:Na:Ca:O (weight percent)
c
M4 14000 -0.345 13000 -0.0068 11000 -0.0953 20000 -0.075 8000 -0.4779
c
c
c
c ----- Source Definitions -----
c
c          SDEF: Cell 5; Tabulated Energies (A); Radial Distance; Electron;
c
SDEF POS 0 0 0 AXS=0 0 1 EXT=d2 RAD=d3 ERG=d1 PAR=3
c
c          ** 142-Praseodymium BETA ENERGY DISTRIBUTION **
c
c          ** use this energy distribution for 142-Praseodymium simulations **
c
SI1 A 0.017 0.172 0.265 0.395 0.574 0.766 0.877 0.946 1.026 1.188
      1.268 1.343 1.615 1.712 1.884 1.923 2.011 2.064 2.104 2.139 2.160
SP1 D 586 656 673 669 649 632 613 598 578 527
      497 464 311 244 121 95.2 43.4 19.8 7.32 1.19 0.0069
c
c          ** 90-Yttrium BETA ENERGY DISTRIBUTION **
c
c          ** use this energy distribution for 90-Yttrium simulations **
c
c SI1 A 0.1 0.2 0.3 0.4 0.5 0.6 0.7 0.8 0.9 1.0
c      1.1 1.2 1.3 1.4 1.5 1.6 1.7 1.8 1.9 2.0 2.1
c SP1 D 406.1 476.2 528.1 566.1 593.4 612.1 623.7 628.8 627.6 619.9
c      605.2 582.8 552.3 513.1 465.3 409.2 345.9 277.0 205.3 134.3 69.0
SI2 -2.5 2.5          $radial sampling range (set as same tumor radius)
SP2 -21 0            $uniform sampling for line
SI3 0 0.0300        $radial sampling range from 0 to Rmax (same as blood vessel)
SP3 -21 1           $radial sampling probability
c E0
c F8:P 10
c
c ----- Mesh Tally -----
c
tmesh
c xz plane
  rmesh1:e pedep
  cora1 -1.50 29i 1.50
  corb1 -1.50 29i 1.50

```

```
corc1 -2.50 9i 2.50
endmd
NPS 2.0E6
PRDMP 1E7 1E8 0 4
DBCN 18J 1 $ITS-style energy indexing
PRINT
c PRINT -10 -40 -50 -70 -98 -85 -86 -110 -140 -170 -130 -128
```

## A.2: Eye device inputs

### A.2.1 Eye dose profiles at water

```
c Cell Cards
c Pr source
c Pr-glass4.0g/cm3
5 1 -4.0 -11 -12 13 imp:p,e=1
c
900 3 -1 -5 imp:p,e=4
950 2 -0.0012 -6 #900 #5 imp:p,e=1
c void
999 0 #5 #900 #950 imp:p,e=0
c end of cell cards
c *****
c surface card block
c * surface of water *
c Pr Glass Rod
11 CX 0.075
12 PX 0
13 PX -0.50
c 14 PZ 0.5
c 2 SX 2.5 3.0
c 3 SX 2.5 3.1
c 4 PX -0.2
5 SX 2.0 2.0 Seye surface
6 SO 4.0
c 7 PX -2.0
c 8 PX 2.0
c end of surface card block
c *****
MODE p e
c materialcard
c Pr
c Si:Al:Pr0.153:0.)
m1 14000 -0.153 13000 -0.081 59000 -0.445 8000 -0.322
c * air *
c C : 0.0125% N : 75.5267 O : 23.1781 Si : 1.2827%
m2 006000 -0.0125 007014 -75.5267 008016 -23.1781 018000 -1.2827
c water
c H : 2O : 1
m3 1001 2 8016 1
SDEF cell=5 POS=2.5 0 0 ERG=d1 PAR=3 rad=d2 eff=0.0001 AXS=1 0 0 EXT=d3
c SDEF cell=5 ERG=D1 PAR=3 rad=d2
```

```

SI1 A 0.017 0.172 0.265 0.395 0.574 0.766 0.877 0.946 1.026 1.188
      1.268 1.343 1.615 1.712 1.884 1.923 2.011 2.064 2.104 2.139 2.160
SP1 D 586 656 673 669 649 632 613 598 578 527
      497 464 311 244 121 95.2 43.4 19.8 7.32 1.19 0.0069
c SI1 L 0.017 0.172 0.265 0.395 0.574 0.766 0.946 1.188 1.343 1.712 2.011 2.104
c SP1 D 586 656 673 669 649 632 598 527 464 244 43.4 7.32
SI2 0 0.075
SP2 -21 1
SI3 0 -0.5 $radial sampling range
SP3 -21 0 $uniform sampling for line
c E0
c F8:P 10
c mesh tally
tmesh
c xz plane
  rmesh1:e pedep
  cora1 0 60i 2.0
  corb1 -1.0 60i 1.0
  corc1 -0.03 2i 0.03
endmd
NPS 2.00E+06
DBCN 18J 1 $ITS-styindexing
PRDMP 2E6 1E8 0 4
PRINT
c PRINT -10 -40 -50 -70 -98 -85 -86 -110 -140 -170 -130 -128

```

## A.2.2 Dose at Water for <sup>142</sup>Pr, <sup>90</sup>Y and <sup>188</sup>Re

### Eye dose profiles at water

```

c Cell Cards
c Pr source
c Pr-glass4.0g/cm3
c Praseodymium Microsphere
c 5 1 -4.0 11 -12 13 -14 5 3 -8 imp:p,e=1
c Yttrium Microsphere
c 5 1 -3.29 11 -12 13 -14 5 3 -8 imp:p,e=1
c Rhenium Microsphere
5 1 -4.00 11 -12 13 -14 5 3 -8 imp:p,e=1
c
900 3 -1 -5 imp:p,e=4
950 2 -0.0012 -6 7 #900 #5 imp:p,e=1
c void
999 0 #5 #900 #950 imp:p,e=0
c end of cell cards
c surface card block
c surface of water
11 PY -0.5
12 PY 0.5
13 PZ -0.5
14 PZ 0.5
c 2 SX 2.5 3.0
c 3 SX 2.5 3.1
3 PX -0.2
5 SX 2.0 2.0
6 SO 4.0
7 PX -2.0
8 PX 2.0
c end of surface card block
MODE p e
c materialcard
c Pr
c Si:Al:Pr0.153:0.)
c m1 14000 -0.153 13000 -0.081 59000 -0.445 8000 -0.322
c Y
c Si:Al:Y:O
c m1 14000 -0.194 13000 -0.106 39000 -0.303 8000 -0.397
c Si:Al:Re:0
m1 14000 -0.194 13000 -0.106 75000 -0.303 8000 -0.397
c air
c C : 0.0125% N : 75.5267 O : 23.1781 Si : 1.2827%

```

```

m2 006000 -0.0125 007014 -75.5267 008016 -23.1781 018000 -1.2827
c water
c H : 2O : 1
m3 1001 2 8016 1
SDEF cell=5 POS=2.5 0 0 ERG=d1 PAR=3 rad=d2 eff=0.0001
c SDEF cell=5 ERG=D1 PAR=3 rad=d2
C Praseodymium Energy Spectrum
c SI1 A 0.017 0.172 0.265 0.395 0.574 0.766 0.877 0.946 1.026 1.188
c 1.268 1.343 1.615 1.712 1.884 1.923 2.011 2.064 2.104 2.139 2.160
c SP1 D 586 656 673 669 649 632 613 598 578 527
c 497 464 311 244 121 95.2 43.4 19.8 7.32 1.19 0.0069
c Yttrium Energy Spectrum
c SI1 A 0.1 0.2 0.3 0.4 0.5 0.6 0.7 0.8 0.9 1.0
c 1.1 1.2 1.3 1.4 1.5 1.6 1.7 1.8 1.9 2.0 2.1
c SP1 D 406.1 476.2 528.1 566.1 593.4 612.1 623.7 628.8 627.6 619.9
c 605.2 582.8 552.3 513.1 465.3 409.2 345.9 277.0 205.3 134.3 69.0
c Rhenium Energy Spectrum
SI1 A 0.034 0.146 0.263 0.389 0.535 0.676 0.793 0.885 0.978 1.060
1.143 1.235 1.318 1.411 1.488 1.668 1.751 1.804 1.911 1.975 2.048
SP1 D 492.8 580.1 658.1 717.3 759.5 764.1 745.4 717.3 676.8 628.5
575.4 509.9 447.6 371.2 308.8 170.0 113.8 84.2 34.3 17.2 4.7
c SI1 L 0.017 0.172 0.265 0.395 0.574 0.766 0.946 1.188 1.343 1.712 2.011 2.104
c SP1 D 586 656 673 669 649 632 598 527 464 244 43.4 7.32
SI2 2.5 2.7
SP2 -21
c E0
c F8:P 10
c mesh tally
tmesh
c xz plane
rmesh1:e pedep
cora1 0 29i 1.6
corb1 -0.8 29i 0.8
corc1 -0.8 29i 0.8
endmd
NPS 2.00E+06
DBCN 18J 1 $ITS-styindexing
PRDMP 2E6 1E8 0 4
PRINT
c PRINT -10 -40 -50 -70 -98 -85 -86 -110 -140 -170 -130 -128

```

### A.2.3 Eye dose profiles at water: Experimental Geometry

```

c Cell Cards
c Pr source
c Pr-glass4.0g/cm3
5 1 -4.0 -11 -12 13 imp:p,e=1
c
900 3 -1 14 -15 16 -17 18 -19 imp:p,e=4
950 2 -0.0012 -6 #900 #5 imp:p,e=1
c void
999 0 #5 #900 #950 imp:p,e=0
c end of cell cards
c *****
c surface card block
c * surface of water *
c Pr Glass Rod
c
11 CX 0.075
12 PX 0
13 PX -0.5
14 PX 0 $Water Box 2.5 x 2.5 x 2.5 cm3
15 PX 2.5
16 PY -1.25
17 PY 1.25
18 PZ -1.25
19 PZ 1.25
c 14 PZ 0.5
c 2 SX 2.5 3.0
c 3 SX 2.5 3.1
c 4 PX -0.2
c 5 SX 2.0 2.0
6 SO 4.0
c 7 PX -2.0
c 8 PX 2.0
c end of surface card block
c *****
MODE p e
c materialcard
c Pr
c Si:Al:Pr0.153:0.)
m1 14000 -0.153 13000 -0.081 59000 -0.445 8000 -0.322
c * air *
c C : 0.0125% N : 75.5267 O : 23.1781 Si : 1.2827%
m2 006000 -0.0125 007014 -75.5267 008016 -23.1781 018000 -1.2827

```

```

c water
c H : 2O : 1
m3 1001 2 8016 1
c
c Source Definitions
c
SDEF cell=5 POS=-0.25 0 0 ERG=d1 PAR=3 rad=d2 eff=0.0001 AXS=1 0 0 EXT=d3
c SDEF cell=5 ERG=D1 PAR=3 rad=d2
c
c Praseodymium-142 Beta Spectrum
c
SI1 A 0.017 0.172 0.265 0.395 0.574 0.766 0.877 0.946 1.026 1.188
1.268 1.343 1.615 1.712 1.884 1.923 2.011 2.064 2.104 2.139 2.160
SP1 D 586 656 673 669 649 632 613 598 578 527
497 464 311 244 121 95.2 43.4 19.8 7.32 1.19 0.0069
c
c
c SI1 L 0.017 0.172 0.265 0.395 0.574 0.766 0.946 1.188 1.343 1.712 2.011 2.104
c SP1 D 586 656 673 669 649 632 598 527 464 244 43.4 7.32
c
SI2 0 0.075 $radial sampling range
SP2 -21 1 $radial sampling probability
SI3 0 -0.5 $radial sampling range
SP3 -21 0 $uniform sampling for line
c E0
c F8:P 10
c mesh tally
tmesh
c xz plane
rmesh1:e pedep
cora1 0 30i 1.0
corb1 -0.5 30i 0.5
corc1 -0.5 30i 0.5
endmd
NPS 2.00E+06
DBCN 18J 1 $ITS-styindexing
PRDMP 2E6 1E8 0 4
PRINT
c PRINT -10 -40 -50 -70 -98 -85 -86 -110 -140 -170 -130 -128

```

## **APENIDIX B: SELECTED PUBLISHED ABSTRACTS AND AWARDS**

East Carolina University Research and Creative Achievement Week 2012 (Awarded “For Best Graduate Poster Presentation in the Natural Sciences Category“) “Dosimetric Investigation of Praseodymium-142 in Eye Plaque Brachytherapy using Monte Carlo Simulation”

AAPM 54th Annual Meeting, Charlotte, NC, 2012 (Oral Presentation) “Dosimetric investigation of Praseodymium-142 microspheres for microsphere brachytherapy of nonresectable hepatic tumors”

ASTRO 54th Annual Meeting, Boston, MA, 2012 (Poster Presentation) “Comparative Study of BED for the beta emitters Pr-142 and Y-90 and Their Applications in Microsphere Brachytherapy of HCC”

NC HPS Meeting 2013 (Winner of the 2012/2013 NC HPS College Student Research Competition) “Dosimetric characterization of Praseodymium-142 for applications in microsphere brachytherapy of Hepatocellular Carcinoma using MCNPX Monte Carlo code”

East Carolina University Research and Creative Achievement Week 2013 (Awarded “For Best Graduate Oral Presentation in the Natural Sciences Category“) “Use of Praseodymium-142 in microsphere brachytherapy for treating Hepatocellular Carcinoma

AAPM 55<sup>th</sup> Annual Meeting, Indianapolis, IN, 2013 (Abstract Accepted) “Use of Biological Effective Dose Volume Histograms to evaluate Hepatocellular Carcinoma coverage due to a single blood vessel embolized with Yttrium-90 and Praseodymium-142 glass microspheres”

ASTRO 55<sup>th</sup> Annual Meeting, Atlanta, GA, 2013 (Abstract Accepted) “Dosimetry of Rhenium-188, Praseodymium-142, and Yttrium-90 using Monte Carlo simulation for application in High Dose Rate Eye Plaque Brachytherapy”